HIGH PRECISION OPTICAL SURFACE METROLOGY USING DEFLECTOMETRY

by

Run Huang

A Dissertation Submitted to the Faculty of the

COLLEGE OF OPTICAL SCIENCES

In Partial Fulfillment of the Requirements

For the Degree of

DOCTOR OF PHILOSOPHY

In the Graduate College

THE UNIVERSITY OF ARIZONA

2015

THE UNIVERSITY OF ARIZONA
GRADUATE COLLEGE

As members of the Dissertation Committee, we certify that we have read the dissertation prepared by Run Huang, titled "High Precision Optical Surface Metrology Using Deflectometry" and recommend that it be accepted as fulfilling the dissertation requirement for the Degree of Doctor of Philosophy.

_____ Date: 07/27/2015
James H. Burge

_____ Date: 07/27/2015
Hong Hua

_____ Date: 07/27/2015
Peng Su

Final approval and acceptance of this dissertation is contingent upon the candidate's submission of the final copies of the dissertation to the Graduate College.

I hereby certify that I have read this dissertation prepared under my direction and recommend that it be accepted as fulfilling the dissertation requirement.

_____ Date: 07/27/2015
Dissertation Director: James H. Burge

STATEMENT BY AUTHOR

This dissertation has been submitted in partial fulfillment of the requirements for an advanced degree at the University of Arizona and is deposited in the University Library to be made available to borrowers under rules of the Library.

Brief quotations from this dissertation are allowable without special permission, provided that an accurate acknowledgement of the source is made. Requests for permission for extended quotation from or reproduction of this manuscript in whole or in part may be granted by the copyright holder.

SIGNED: Run Huang

ACKNOWLEDGEMENTS

I would like to thank my dissertation advisor Jim Burge for providing the exciting opportunities to work on real optical projects. It has been an honor to work on so many challenging projects. Jim's expertise and insights inspired me in numerous aspects. Thanks to Peng Su for introducing me to the "SCOTS group" and guiding me to be an effective optical engineer. I would also like to thank my committee member Professor Hong Hua, for her suggestions and discussions on this dissertation.

I would like to thank all the staffs in Large Optics Fabrication and Testing (LOFT) group, for your support in research and projects. Thanks to Matt Rademacher, for helping me to build the mechanical hardware of SCOTS for an oversea project of testing the prototype of fast steering secondary mirror of Giant Magellan Telescope (GMT) in Korea. Thanks to Scott Benjamin, for the support in designing and assembly the SCOTS system for testing the primary mirror of Daniel K. Inouye Solar Telescope. Thanks to Todd Hone, for the help in the project of testing the secondary mirror of Large Binocular Telescope (LBT).

Thanks to all the lab mates and other group members, for all the discussions on the projects, researches and working together to solve the problems. I am really proud to be a member of this great group!

Thanks to my parents, Li Lin and Hongjun Huang, for everything you have given me!

Thanks to my husband, Xinda Hu, for your constant companion along the journey.

DEDICATION

To my parents, Li Lin and Hongjun Huang

To my better half, Xinda Hu

TABLE OF CONTENTS

LIST OF FIGURES

LIST OF TABLES

ABSTRACT

Software Configurable Optical Test System (SCOTS) developed at University of Arizona is a highly efficient optical metrology technique based on the principle of deflectometry, which can achieve comparable accuracy with interferometry but with low-cost hardware. In a SCOTS test, an LCD display is used to generate structured light pattern to illuminate the test optics and the reflected light is captured by a digital camera. The surface slope of test optics is determined by triangulation of the display pixels, test optics, and the camera. The surface shape is obtained by the integration of the slopes.

Comparing to interferometry, which has long served as an accurate non-contact optical metrology technology, SCOTS overcomes the limitation of dynamic range and sensitivity to environment. It is able to achieve high dynamic range slope measurement without requiring null optics.

In this dissertation, the sensitivity and performance of the test system have been analyzed comprehensively. Sophisticated calibrations of system components have been investigated and implemented in different metrology projects to push this technology to a higher accuracy including low-order terms. A compact on-axis SCOTS system lowered the testing geometry sensitivity in the

metrology of 1-meter highly aspheric secondary mirror of Large Binocular Telescope. Sub-nm accuracy was achieved in testing a high precision elliptical X-ray mirror by using reference calibration. A well-calibrated SCOTS was successfully constructed and is, at the time of writing this dissertation, being used to provide surface metrology feedback for the fabrication of the primary mirror of Daniel K. Inouye Solar Telescope which is a 4-meter off-axis parabola with more than 8 mm aspherical departure.

1 INTRODUCTION

1.1 Metrology methods for optical surface measurement

High performance requirements on optics push currently-available fabrication and metrology technologies to their limits. Any arbitrary optical surfaces can be fabricated in modern computer controlled figuring; however, fabrication of high precision optics highly relies on the metrology of optical surface to serve as a feedback in polishing deterministic process to correct subtle surface distortion. The advances of metrology techniques determine the quality of the optics that can be made.

Surface metrology techniques can be categorized as contact profilometry and contact-free profilometry. Contact profilometry [1] is probably the oldest and most accepted method of accurately measuring an arbitrary surface profile. It uses a mechanical tip to drag along the surface and the tip deflections are measured using mechanical, electrical, or optical transducers. It can measure to atomic scale when atomic force microscope is used as contact stylus. The disadvantages of contact profilometry include relatively long measurement time for excellent lateral resolution and potential damage of test surface by the stylus tip.

Instead of using mechanical stylus tip, optical profilometry uses an optical probe to map surface topography by sensing the best focus position on the test optics. Different methods were developed to improve the detection of focal point; confocal microscopy [2,3] is one of the important techniques that is worth to be pointed out. It uses a spatial filter at the confocal plane of the microscopy objective to block out-of-focus light to ensure high signal-to-noise images for surface height determination. Confocal microscopy can achieve very high vertical resolution by using objective with large numerical aperture (NA), however, since it is single point detection, the speed of data acquisition is a limiting factor which leads to a number of works on the improvement of this aspect.

Interferometry [4] might be the most popular and widely used non-contact optical profilometry in optical testing. It utilizes the wave nature of the light to achieve high accuracy measurement by detecting the optical path length difference between reference surface and test surface. One of the most common interferometry configurations is Fizeau interferometry. It minimizes the environmental influences by maintaining a common path of the reference beam and test beam. Through the analysis of interference fringe pattern, 2D surface topography of test surface can be obtained in one measurement. However, classical interferometry usually requires specially designed null optics such as

computer generated hologram (CGH) [5,6] for measuring steep surfaces, which can make the test very expensive and hard to align. And sometimes, a stitching process is needed. White light interferometry overcomes this limit by evaluating the interference intensity profile using low temporal coherence light source (white light) and vertical scanning [7]. Instead of capturing the 2D fringe pattern directly, a white light interferometer measures the sum of all the fringe intensities and the broadband spectrum of the light source ensures its high position measurement sensitivity. Typically white light interferometry can achieve vertical resolution ~ 3 nm and lateral resolution ~1 um. White light interferometer still requires synchronized lateral scanning of the sample. Therefore, measurement time is one of the major concerns of this method.

Deflectometry is another non-contact profilometry for measuring specular optical surface. Software Configurable Optical Test System (SCOTS) [8] developed at the University of Arizona is one of the deflectometric techniques. The basic principle of SCOTS uses a digital camera to capture light that is created by a controlled source and reflected from the surface under test. The reflected light is analyzed to provide an accurate measurement of slope variations in the surface under test. The slope errors are integrated to provide a full map of the surface errors. Comparing with interferometry, SCOTS is able to achieve high dynamic range slope measurement by using computer-controlled large displays

as light source such as LCD monitors. With careful calibration, we have demonstrated the accuracy of SCOTS measurement rivals that of interferometry but at lower cost and easier system setup.

Surface metrology techniques are not only limited to the methods that mentioned above, new applications drive the development of news methods and improvement of existing methods to meet different measurement requirements.

1.2 Motivation

The motivation of this dissertation is to advance SCOTS to higher accuracy and a mature test tool for optical metrology. High accuracy SCOTS metrology involves a great effort in system calibrations including test geometry, imaging camera and LCD display. Understanding and quantifying the effects of SCOTS components, such as geometry sensitivity, camera aberration, camera distortion, display nonlinearity, display shape distortion, and etc. are the fundamentals to guide the design and implementation of system calibrations.

Through this dissertation, we want to develop more solid understanding of the system fundamentals so that we can give accurate predication of system performance and error budget in future systems. From the engineering point of view, we hope to apply system calibrations on real test projects to have practical implementation and verification.

1.3 Dissertation Overview

This dissertation consists of six chapters. It gives an in-depth analysis of SCOTS components and summarizes engineering implementation of system calibrations in different metrology projects.

Chapter 2 PRINCIPLE OF DEFLECTOMETRY describes the test principle of SCOTS. A virtual null test model is established by Zemax ray tracing and an approximated equation based on transverse ray aberration is used for slope calculation.

Chapter 3 IMPROVED SYSTEM GEOMETRY FOR HIGH ACCURACY LOW-ORDER SURFACE MEASUREMENT provides a sensitivity analysis on the geometry of system components. An on-axis test configuration was proposed to reduce geometry sensitivity and a real test system was built for investigating the secondary mirror of Large Binocular Telescope (LBT).

Chapter 4 DISPLAY AND CAMERA CALIBRATION FOR HIGH ACCURACY SURFACE MEASUREMENT provides comprehensive discussions of LCD display and camera effects in SCOTS. Calibration methods with practical examples are also provided. A test system utilizing the calibration methods described in this chapter for measuring the primary mirror of Daniel K. Inouye Solar Telescope is presented at the end of this chapter.

Chapter 5 ADVANCED SYSTEM CALIBRATION USING REFERENCE SURFACE provides a calibration method to reduce systematic error by measuring a reference surface. An application example on testing an X-ray mirror is given.

Conclusions are given in Chapter 6.

APPENDIX A: includes a published peer-reviewed paper, focusing on the implementation of an on-axis SCOTS system for investigation of one of the secondary mirrors of Large Binocular Telescope (LBT).

APPENDIX B: includes a paper accepted by Optical Engineering. It reports a high accuracy SCOTS metrology on a super polished elliptical X-ray mirror using reference calibration. Detailed experiment procedures, including test model set up, test alignment, distortion correction and calibration with a reference flat are presented.

APPENDIX C: A Table of Standard Zernike Polynomials

2 PRINCIPLE OF DEFLECTOMETRY

In this chapter, development history of deflectometric technique is reviewed in Sec 2.1. The principle of SCOTS and test model are described in Sec 2.2, Sec 2.3. Sec. 2.4 summarizes current challenges in SCOTS measurements.

2.1 History of deflectometry

The fundamental of all deflectometric techniques is to detect the lateral displacement of reflected /refracted light from the test surface and thus to retrieve the slope of the measured wavefront or test surface.

The first realization of deflectometry is Foucault Knife Edge Test [9], dating back to 1858. It determines the topography of object by analyzing the shadow pattern created by a knife edge. Several advanced versions of the Foucault Knife Edge Test were developed after that, which include Wire Test, Ronchi Test [10,11] and Hartmann Test [12]. The knife edge is replaced by a thin wire and a binary grating in the Wire Test and Ronchi Test respectively. Hartmann Test uses a point light source and a grid mask in front of the test object to achieve one time 2D surface sampling on the test sample without the need of scanning. It was introduced by Johannes Hartmann in 1900 and further improved by Roland

Shack and Ben Platt in 1971 by replacing the grid mask with a lenslet array at transferred pupil, which is so called Shark-Hartmann Test [13,14].

As time goes by, a new deflectometric method called Phase Measuring Deflectometry (PMD) was developed and published by Knauer [15] et al, in 2004 with detailed system description and analysis. It uses an LCD display to generate intensity-modulated sinusoidal light pattern to illuminate test objects and a camera placed in the detection path to capture the distorted light patterns. The camera directly images the test object which provides a much denser spatial sampling than Hartman screen in Hartmann test and lenslet array in Shark-Hartmann Test; and the use of coded light pattern provides a precise measurement of illuminous light source position.

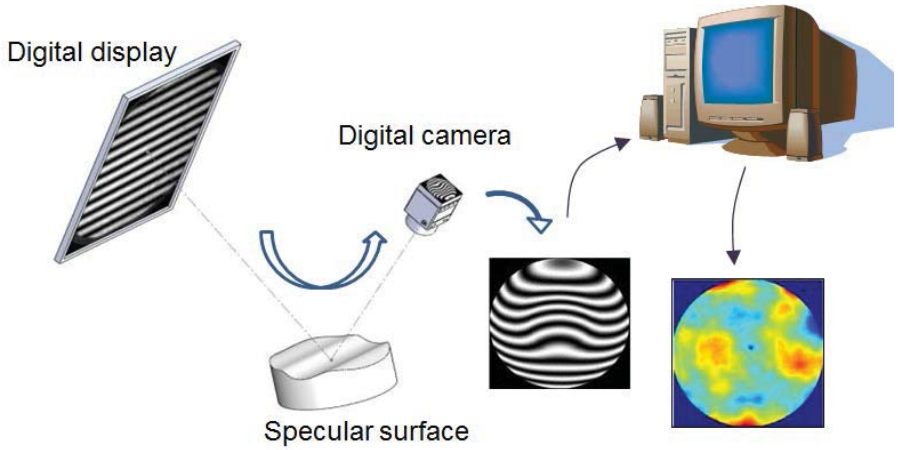

Figure 2.1 Example of Phase Measuring Deflectometry (PMD)

Software Configurable Optical Test System (SCOTS) developed in University of Arizona is one of the PMD techniques utilizing precise system calibration to

measure optics with high accuracy that rivals interferometry. The performance of SCOTS has been successfully demonstrated in testing many large astronomy telescope mirrors such as GMT primary [16], LBT secondary [17,18], DKIST primary and precision X-ray mirrors [19].

2.2 Reverse Hartmann model

As mentioned above, SCOTS and Hartmann Test are both based on similar deflectometric techniques. Therefore, to describe the measurement principle of SCOTS, we make analogy between SCOTS and classic Hartmann test.

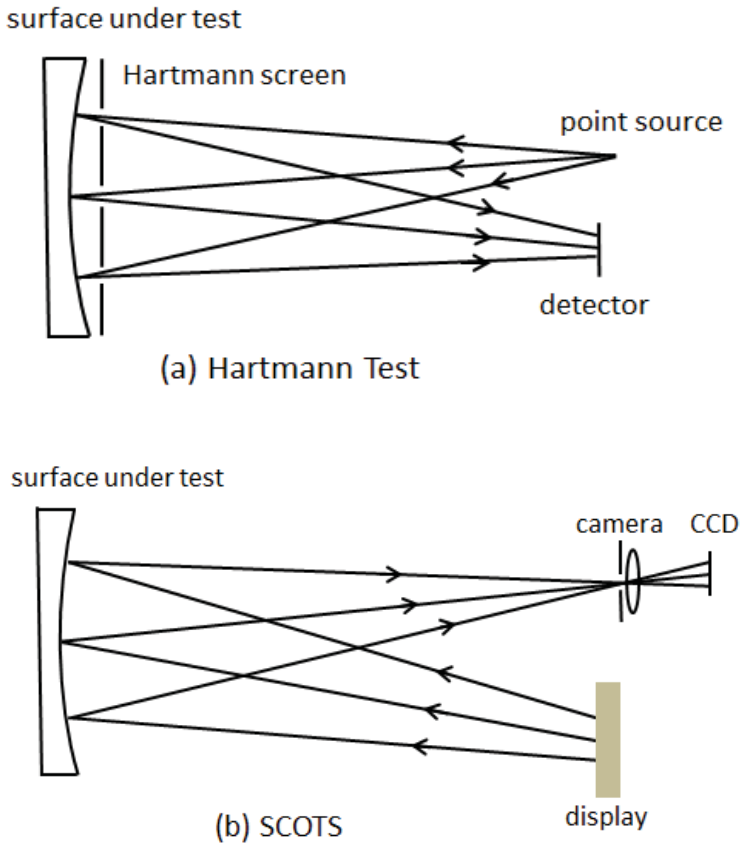

Figure 2.2 Schematic setup of (a) a Hartmann test and (b) a SCOTS test. The SCOTS traces the ray in reverse compared to the Hartmann test.

As shown in Figure 2.2 (a), in a Hartmann test, a point source of light is placed near the center of curvature of the test mirror, and a plate with a number of holes (Hartmann screen) is centered right in front of the test mirror. The point source illuminates the entire test mirror, but only the light passing through the holes is reflected. The Hartmann screen defines the sampling on the mirror and a set of corresponding ray bundles. A detector is placed near the focus and records the positions of reflected ray bundles. One or more images are recorded by the detector for slope calculation.

In SCOTS, the detector in Hartmann test is replaced by an LCD screen displaying coded light pattern and the point source is replaced by a camera focusing on the test mirror to detect the "distorted" light pattern reflected by the test mirror. Sampling on the test mirror is achieved by the ray bundles of the imaging system which are defined by camera aperture and each camera pixel. Therefore, no Hartmann screen is needed. The illuminating pixel position, reflection region on the mirror and camera aperture-center uniquely define an incident ray and its reflected ray. Using the coordinates of these three points, the local surface slope of test mirror can then be calculated by triangulations using Eq.(2.1) and (2.2). The parameters in Eq.(2.1) and (2.2) are defined in Figure 2.3.

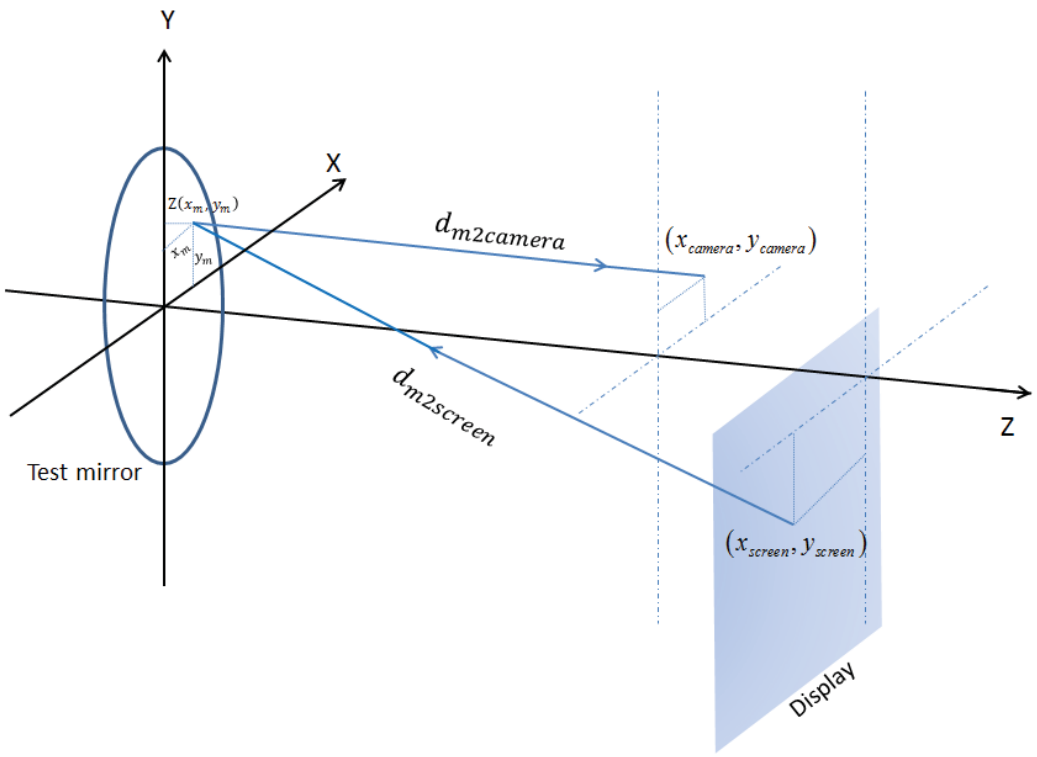

Figure 2.3 Geometry for slope calculation in deflectometry

$$\frac{\partial Z(x_m, y_m)}{\partial x} = \frac{\dfrac{x_m - x_{screen}}{d_{m2screen}} + \dfrac{x_m - x_{camera}}{d_{m2camera}}}{\dfrac{z_{m2screen} - Z(x_m, y_m)}{d_{m2screen}} + \dfrac{z_{m2camera} - Z(x_m, y_m)}{d_{m2camera}}} \tag{2.1}$$

$$\frac{\partial Z(x_m, y_m)}{\partial y} = \frac{\dfrac{y_m - y_{screen}}{d_{m2screen}} + \dfrac{y_m - y_{camera}}{d_{m2camera}}}{\dfrac{z_{m2screen} - Z(x_m, y_m)}{d_{m2screen}} + \dfrac{z_{m2camera} - Z(x_m, y_m)}{d_{m2camera}}} \tag{2.2}$$

where $\frac{\partial Z(x_m, y_m)}{\partial x}$ and $\frac{\partial Z(x_m, y_m)}{\partial y}$ are the surface slopes of the test mirror; x_m and y_m are coordinates of mirror pixel, x_{screen} and y_{screen} are the coordinates of corresponding screen position; x_{camera} and y_{camera} are camera aperture coordinates;. $d_{m2screen}$ and $d_{m2camera}$ are the distances from mirror to LCD and camera aperture

respectively; z is the surface height of test mirror; $z_{m2screen}$ and $z_{m2camera}$ are the z-directional distance from mirror vertex to LCD and camera aperture respectively.

In Eq.(2.1) and (2.2), the parameter $Z(x_m, y_m)$ is actually unknown and needs to be measured in the test, therefore, the nominal value of the test surface is used instead to calculate the slope of the mirror. Usually the surface under test is close to its nominal value within several μm and the error is very small comparing to the distance $z_{m2screen}$ and $z_{m2camera}$, which are usually in the range of meters, therefore, this approximation is valid and the error is negligible.

2.3 Virtual null using ray tracing

When testing a polished optical surface, we are interested in the surface departure of the test surface from its nominal shape. We achieve this by setting up a ray tracing model using Zemax with the test optics in its nominal shape and calculating the slope difference using transverse ray aberration model. Surface deviation (ΔZ) from the ideal shape is obtained by integrating the slope differences.

Since SCOTS works like a Hartmann test with the light path in reverse, the ray trace model in Zemax is quite similar to a Hartmann test. The camera is modeled as a point source sending the light to the test surface and the LCD screen is modeled as the image plane to capture the reflected light. Utilizing Zemax ray tracing function to sample the mirror aperture and trace those

individual rays, an ideal spot distribution on the image plane can be obtained (x_{ideal} and y_{ideal}) while in the experiment this spot distribution ($x_{measured}$ and $y_{measured}$) is calculated from line scanning or phase shifting method [8].

Based on transverse ray aberration model [20], system wavefront aberrations are approximately equal to the transverse ray aberration by dividing the spot coordinate differences (Δx_{screen} and Δy_{screen}) with measured mirror-to-screen distance ($d_{m2screen}$). The slopes of surface deviation ($\frac{\partial \Delta Z(x_m, y_m)}{\partial x}$ and $\frac{\partial \Delta Z(x_m, y_m)}{\partial y}$) are then obtained by half the wavefront aberrations as expressed in Eq. (2.3). Integration of $\frac{\partial \Delta Z(x_m, y_m)}{\partial x}$ and $\frac{\partial \Delta Z(x_m, y_m)}{\partial y}$ gives surface departure of test optics from its nominal shape.

$$\frac{\partial \Delta Z(x_m, y_m)}{\partial x} \cong -\frac{\Delta x_{screen}}{2d_{m2screen}}, \quad \frac{\partial \Delta Z(x_m, y_m)}{\partial y} \cong -\frac{\Delta y_{screen}}{2d_{m2screen}} \tag{2.3}$$

$$\Delta x_{screen} = x_{measured} - x_{ideal}, \qquad \Delta y_{screen} = y_{measured} - y_{ideal} \tag{2.4}$$

where $\frac{\partial \Delta Z(x_m, y_m)}{\partial x}$ and $\frac{\partial \Delta Z(x_m, y_m)}{\partial y}$ are the slope differences between measurement and calculated result from Zemax ray tracing where the surface is under its nominal shape. $d_{m2screen}$ is the distance from mirror to LCD display; $x_{measured}$ and $y_{measured}$ are measured spot distributions on the LCD display; x_{ideal} and y_{ideal} are spot distributions on the LCD display by Zemax ray tracing.

Playing the similar role as null optics in interferometry test, the Zemax model in SCOTS test acts like a virtual “null test”.

2.4 Challenges in deflectometry

Although deflectometry measurement is not subject to rigorous alignment in interferometry test, the absolute position of the illumination light source, observation point and test optics needs to be measured to a high accuracy for low uncertainty slope calculation. A geometry bias could easily generate fake low-order shape, such as power, astigmatism and coma.

Another issue with deflectometric measurement is the distortion mapping in the imaging system. Imaging camera in the deflectometry system can provide distorted sampling of the test optics due to camera lens distortion and viewing perspective. Careful mapping correction is required in data processing to avoid systematic error. Similar to test geometry, low-order shape is more sensitive than high-order shape in mapping correction.

Calibration of systematic error in deflectometry is the most important step to get reliable measurement result. Different methods have been developed to improve the calibrations. The calibration methods discussed in this dissertation include precise calibration of each individual element and system calibration as well, such as rotation average and reference calibration.

3 IMPROVED SYSTEM GEOMETRY FOR HIGH ACCURACY LOW-ORDER SURFACE MEASUREMENT

All deflectometric systems are very sensitive to geometry, and a large amount of calibration effort is put into the geometry calibration. SCOTS is no exception. As mentioned in Sec. 2.3, SCOTS utilizes Zemax ray tracing to generate ideal spot distribution (x_{ideal} and y_{ideal}) on the display to virtually "null" the test. To correctly setup race tracing model in Zemax, geometric parameters, such as the positions of the camera aperture, mirror and the screen need to be measured to a high accuracy.

In this chapter, geometry sensitivity of SCOTS test is analyzed in detail. Sec 3.1 introduces geometry measurement and calibration procedures. Then, test sensitivity on camera position, display position and mirror position are analyzed using parametric expressions. An on-axis SCOTS system with reduced sensitivity on astigmatism was built and presented in Sec 3.4 [17,18]. It was used for measuring low-order shape of secondary mirror of Large Binocular Telescope [21] and the results were excellent.

3.1 Geometry calibration

In most of the SCOTS tests for large telescope mirrors, a laser tracker system [22] is used to measure test geometry in a large test volume from a few meters to more than ten meters. The mirror position (mainly mirror center and tip/ tilt) is usually defined by measuring several (usually four) Spherically Mounted Retro-reflectors (SMR) clamped on the mirror edge as shown in Figure 3.1. Camera aperture center and display position are determined by measuring their reference SMRs mounted around the camera and the display.

To get the actual positions of aperture center and the display in the test configuration, the relative positions between camera aperture and its reference SMRs, display and its reference SMRs, are pre-calibrated using an optical CMM before mounting in the test tower. The layout and actual setup of pre-calibration are shown in Figure 3.2 and Figure 3.3.

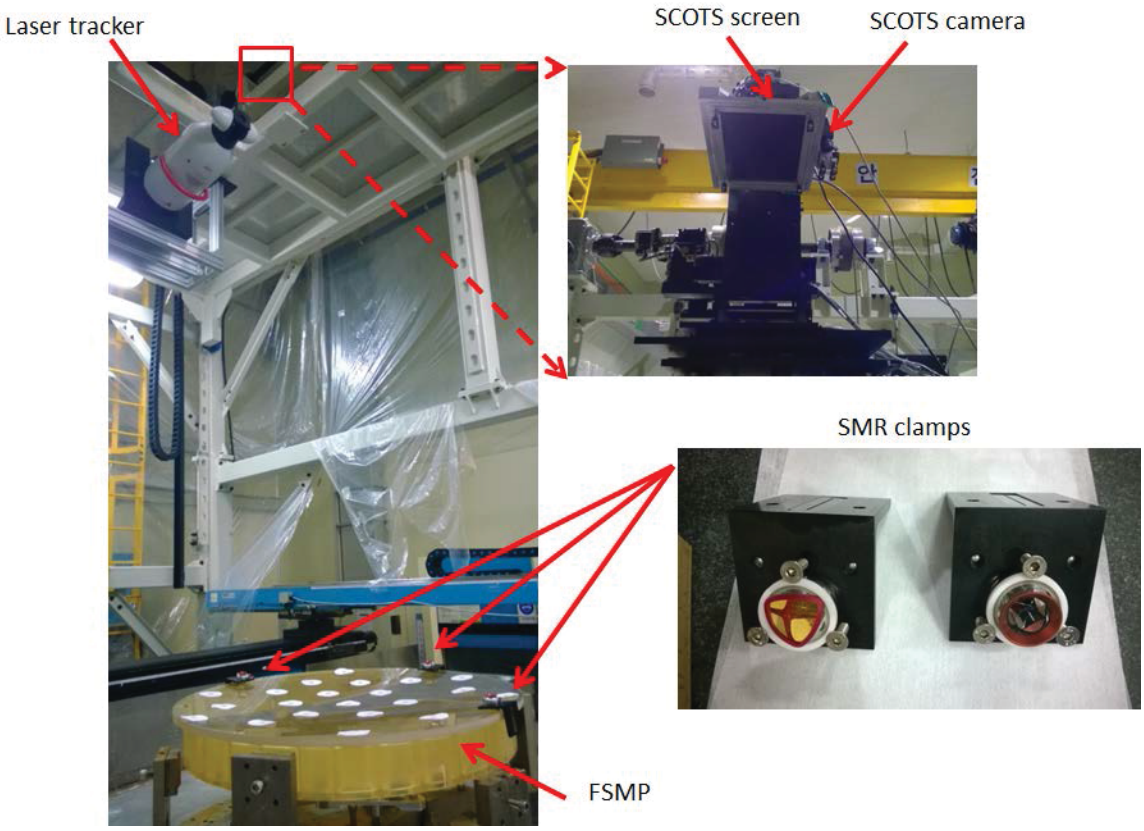

Figure 3.1 SCOTS test for measuring the prototype of fast-steering mirror (FSMP) of Giant Magellan Telescope (GMT). Laser tracker was mounted between the SCOTS and FSMP to measure test geometry. Fixtures were clamped on the mirror edge to define mirror position. Reference SMRs were mounted on SCOTS to determine display and camera aperture position.

The optical CMM is a modified CMM using a Point Source Microscope (PSM) [23] as the probing arm. The basic ideal of pre-calibration is to find out geometric relationship between camera aperture (or display pixels) and its reference SMRs. Take the pre-calibration of camera aperture as an example, as shown in Figure 3.2 (b): Firstly, the PSM is focused on the center of camera aperture and the centers of reference SMRs (usually in the calibration, the SMRs

are replaced by high quality steel balls with same size for better imaging quality); then the relative 3D locations of the camera aperture and reference SMRs are recorded under CMM coordinates. In the pre-calibration of display position, as shown in Figure 3.2 (a), usually several pixels on the display are light up and measured to define the plane of the display relative to its reference SMRs. With these calibration data, when the system is in the test tower, by measuring those reference SMRs, camera aperture center and display position can be determined accurately in real test geometry using straightforward coordinate transformation. Figure 3.3 gives an experimental setup for calibrating camera aperture and display pixel positions for a SCOTS system.

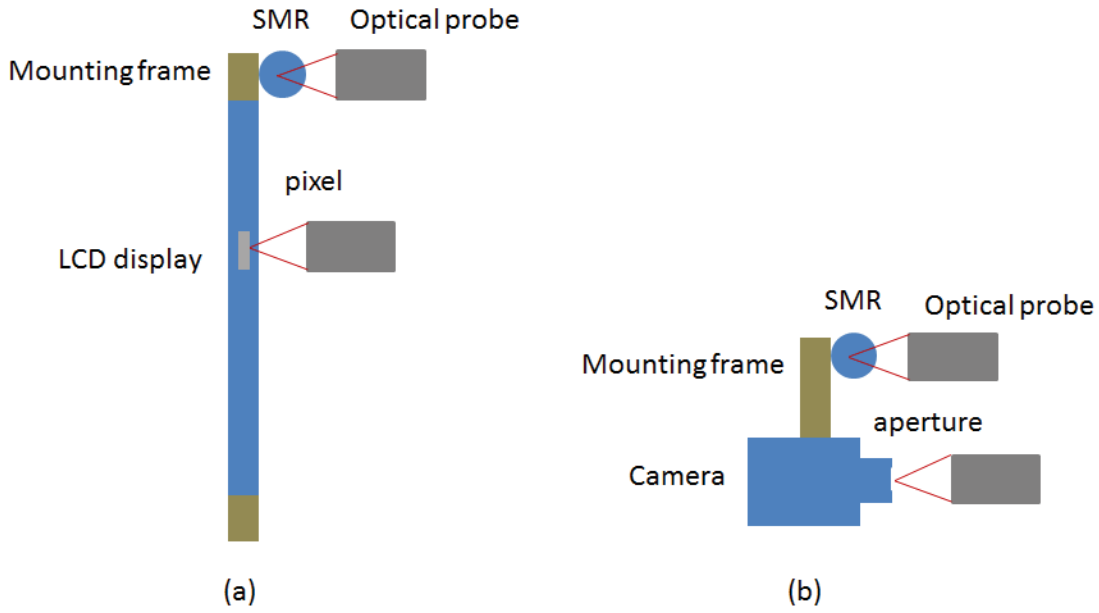

Figure 3.2 Layout for pre-calibration of (a) display and (b) camera aperture position

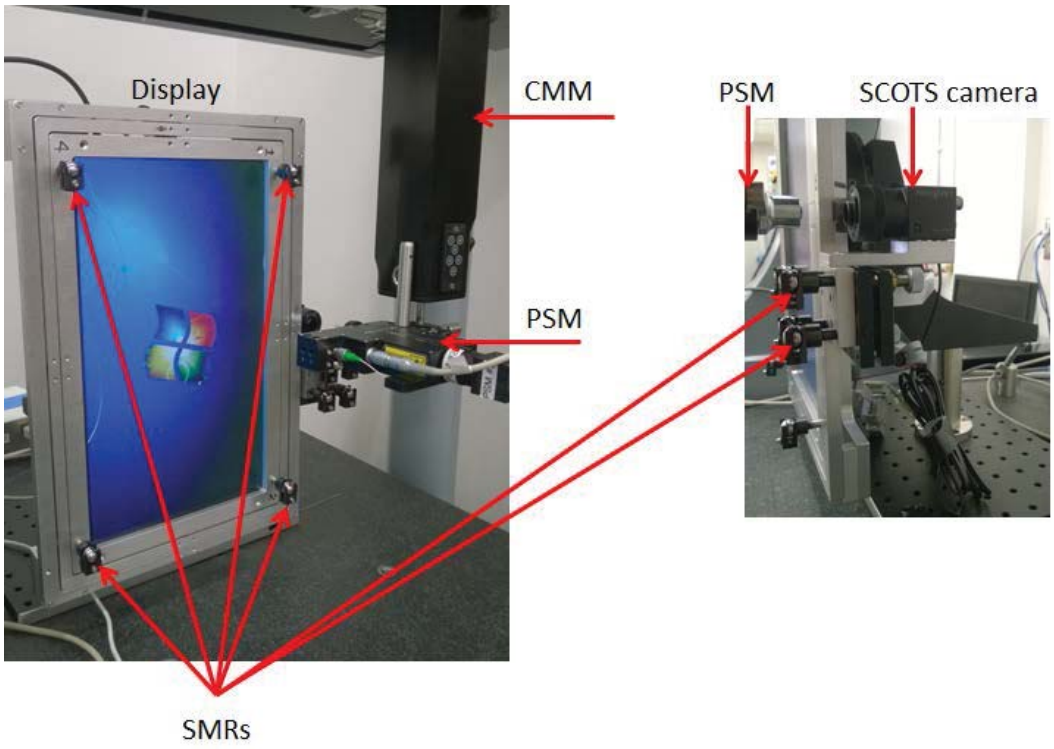

Figure 3.3 Experimental setup for pre-calibration of display and camera aperture position.

3.2 Geometry sensitivity

As described in Chapter 2, the ideal spot distribution on the display can be calculated using reverse ray tracing in Zemax where the camera is modelled as a point source sending the light on to the mirror and being reflected back to the display plane. For test configuration where the camera and display are placed near the conjugate positions of the test mirror, spot distribution (ε_x and ε_y) on the display can be approximated as transverse ray aberration, and wavefront departure $W(x, y)$ at display plane can be found using imaging aberration theory.

For an optical system with a circular exit pupil of radius r, it is convenient to use normalized coordinate. In the discussion of this dissertation, we use normalized Cartesian coordinates $\left(x_p, y_p\right)$, where $\left(x_p, y_p\right) = \rho\left(\sin\theta, \cos\theta\right)$, $0 \le \rho \le 1$ and $0 \le \theta \le 2\pi$. Taking four primary low order modes of $W\left(x, y\right)$, defocus, astigmatism, coma and spherical as examples, the shapes of these modes are in the form of

$$W\left(x_p, y_p\right) = W_{020}\left({x_p}^2 + {y_p}^2\right) + W_{222}{y_p}^2 + W_{131}\left({x_p}^2 + {y_p}^2\right)y_p + W_{040}\left({x_p}^2 + {y_p}^2\right)^2 \quad (3.1)$$

W_{020}, W_{222}, W_{131} and W_{040} are coefficients of defocus, astigmatism, , coma and spherical representing the peak values of the modes.

Spot diagram (ε_x and ε_y) on the display can be approximated as [24]:

$$\varepsilon_y\left(x_p, y_p\right) \simeq -2 f_{\#} \frac{\partial W\left(x_p, y_p\right)}{\partial y_p} \quad (3.2)$$

$$\varepsilon_x\left(x_p, y_p\right) \simeq -2 f_{\#} \frac{\partial W(x_p, y_p)}{\partial x_p} \quad (3.3)$$

$f_{\#}$ is the f-number of the image-forming light cone.

In the following parts of this section, we will discuss test sensitivity on camera position (including lateral and axial position), screen orientation (including tip/tilt and axial position), and mirror orientation (including tip/tilt and clocking) for measuring axisymmetric optics.

3.2.1 Sensitivity on camera lateral position

Traditional SCOTS test uses off-axis test geometry where the camera and display are configured with lateral separation about the axis of the test optics so that the light path will not be blocked. Off-axis test configuration introduces camera lateral position (h) dependent modes in the measured wavefront departure $W(x,y)$, which are usually dominated by astigmatism and coma.

For measuring spherical surface at its paraxial conjugate position, by using Seidel sums [25], we get Seidel coefficients of W_{222} and W_{131}

$$W_{222} = \frac{1}{2} S_{III} \tag{3.4}$$

$$W_{131} = \frac{1}{2} S_{II} \tag{3.5}$$

$$S_{II} = -\sum \bar{A} A y \Delta\left(\frac{u}{n}\right) \tag{3.6}$$

$$S_{III} = -\sum \bar{A}^2 y \Delta\left(\frac{u}{n}\right) \tag{3.7}$$

$$\bar{A} = n\bar{u} + n\bar{y}c \tag{3.8}$$

$$A = nu + nyc \tag{3.9}$$

$$\Delta\left(\frac{u}{n}\right) = \left(\frac{u'}{n'}\right) - \left(\frac{u}{n}\right) \tag{3.10}$$

where $\bar{y}$ is chief ray height, y is marginal ray height, $\bar{u}$ and $\bar{u}'$ are chief ray angles before and after reflection, u and u' are marginal ray angles before and after reflection, n and n' are the refractive index before and after reflection, respectively.

For measuring axisymmetric aspheric surface, the contribution from the aspheric surface to the Seidel sums S_{II} and S_{III} (δS_{II} and δS_{III}) [25] are given in (3.11) and Eq. (3.12).

$$\delta S_{II} = \left(\frac{\bar{y}}{y}\right) a \tag{3.11}$$

$$\delta S_{III} = \left(\frac{\bar{y}}{y}\right)^2 a \tag{3.12}$$

where $a = -\varepsilon^2 \left(\frac{1}{R}\right)^3 y^4 \Delta(n)$ for conic surface of eccentricity ε; and $a = 8\alpha_4 y^4 \Delta(n)$ for an aspheric surface with fourth-order coefficient α_4.

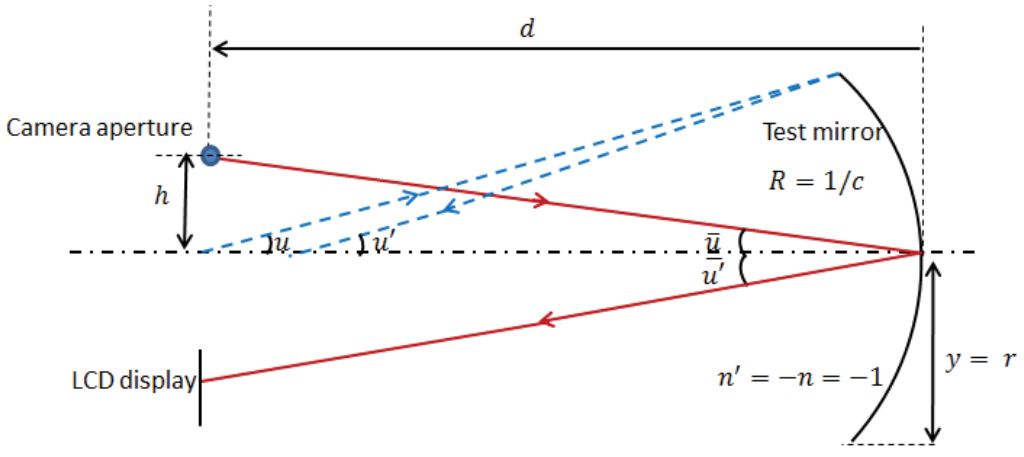

Figure 3.4 Ray tracing for Seidel aberration coefficients calculation

Applying Eq.(3.4) ~ Eq. (3.12) to a SCOTS test as shown in Figure 3.4, two rays are traced through the system, one is the marginal ray for full aperture (blue ray) and the other one is the chief ray for the maximum field, i.e. the camera off-axis distance (red ray). We get

$$W_{222} = \frac{h^2 r^2}{Rd^2} \tag{3.13}$$

$$W_{131} = \frac{hr^3\left(d-R\right)}{R^2 d^2} \tag{3.14}$$

Since $\bar{y} = 0$, the results of Eq. (3.13) and (3.14) can apply all the axisymmetric (including spherical and aspherical)surfaces.

The sensitivities of astigmatism and coma in the measured wavefront departure to camera off-axis distance are

$$\frac{\partial W_{222}}{\partial h} = \frac{2hr^2}{Rd^2} \tag{3.15}$$

$$\frac{\partial W_{131}}{\partial h} = \frac{r^3\left(d-R\right)}{R^2 d^2} \tag{3.16}$$

From Eq.(3.15) and Eq.(3.16), we can see sensitivity of astigmatism in measured wavefront departure to test geometry increases linearly as the test goes more off-axis, while the sensitivity of coma to camera lateral position is independent of camera lateral position h. To convert the wavefront sensitivity

$(\frac{\partial W}{\partial h})$ into surface height $(\frac{\partial Z}{\partial h})$ sensitivity, a factor of 2 needs to be considered in Eq.(3.15) and Eq.(3.16).

We usually use Zernike standard polynomials to represent wavefront or surface map. From the above analysis, we conclude that camera lateral position mainly affect the accuracy of Zernike Z5~Z8 (astigmatism is represented by Z5 and Z6, coma is represented by Z7 and Z8) in the measurement map.

3.2.2 Sensitivity on camera axial position

The uncertainty of camera axial position basically generates defocus W_{020} effect in the measurement.

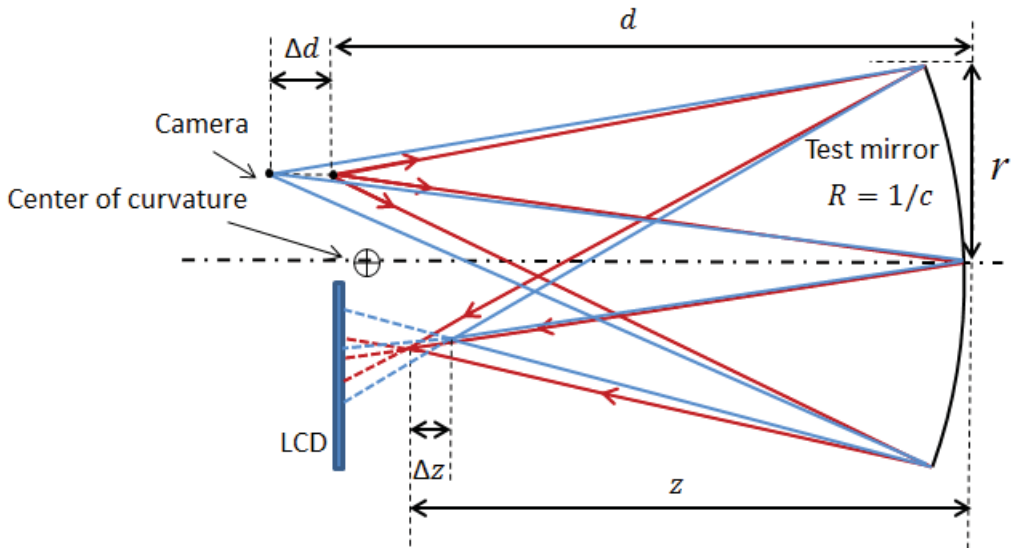

Figure 3.5 Layout showing test sensitivity on camera axial position. Red line represents nominal test position. Blue line represents perturbed test position.

In Figure 3.5, camera is at distance d to the mirror, the conjugate position is determined by first order imaging equation

$$z = \frac{Rd}{2d - R} \tag{3.17}$$

The sensitivity of the paraxial image position to camera axial position is

$$\frac{\partial z}{\partial d} = \frac{-R^2}{(2d - R)^2} \tag{3.18}$$

If the camera axial position shifts Δd , the paraxial conjugate position would shift

$$\Delta z = \frac{-R^2}{(2d - R)^2} \Delta d \tag{3.19}$$

ΔW_{020} is related to the amount of focus shift Δz, and can be expressed as [24]

$$\Delta W_{020} = \frac{1}{8 f_{\#}^{\ 2}} \Delta z \tag{3.20}$$

where $f_{\#}$ is the f-number of the image-forming light cone.

For configuration where the camera is very close to the center of curvature of the test mirror ($d \simeq R$), you will get $\Delta z \simeq -\Delta d$ by substituting $d \simeq R$ into Eq. (3.19) , and thus $\Delta W_{020} \simeq \frac{-1}{8 f_{\#}^{\ 2}} \Delta d$. Converting into Zernike standard coefficients, camera axial position uncertainty ΔW_{020} mainly introduces Zernike power (Z4) term.

3.2.3 Sensitivity on display tip/tilt

Tip/tilt of the display will generate a projection effect of the spot distribution on the display, but the projection direction of each ray is dependent on the test configuration and mirror pupil coordinate. For simplicity, we assume one-directional display tilt θ about x direction as showing in Figure 3.6. For a ray coming from specific mirror pupil coordinate $\left(x_{p,}y_{p}\right)$, the slope error of that ray is given by Eq. (3.21) and (3.22):

$$\Delta S_{y}\left(x_{p,}y_{p}\right)=\frac{\varepsilon_{y}-\varepsilon_{y}^{'}}{d_{m2screen}}=\frac{\varepsilon_{y}\left(1-\frac{\cos\gamma_{\left(x_{p},y_{p}\right)}}{\cos\left(\gamma_{\left(x_{p},y_{p}\right)}+\theta\right)}\right)}{d_{m2screen}} \tag{3.21}$$

$$\Delta S_{x}\left(x_{p,}y_{p}\right)=\frac{\varepsilon_{x}-\varepsilon_{x}^{'}}{d_{m2screen}}=\frac{\varepsilon_{x}-\varepsilon_{y}^{'}\cdot\sin\theta\cdot\tan\beta_{\left(x_{p},y_{p}\right)}}{d_{m2screen}} \tag{3.22}$$

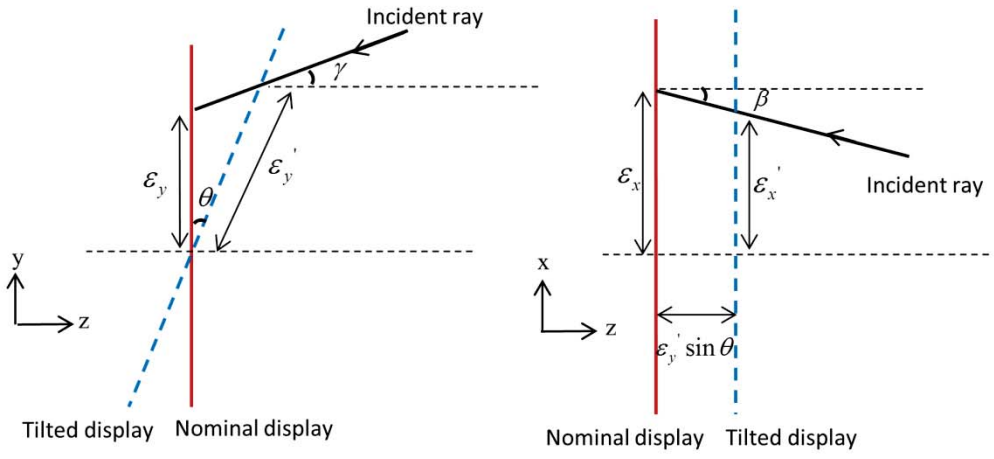

Figure 3.6 Layout showing test sensitivity on display tilt about x direction. Red line represents display at nominal position, blue line represents tilted display plane

where γ and β are the angles of incident ray from mirror pupil $\left(x_p, y_p\right)$ onto the display in yoz and xoz plane. The value of γ and β are functions of pupil coordinate $\left(x_p, y_p\right)$ on the mirror.

From Eq. (3.21), we can see the change of slope $\Delta S_y\left(x_{p,} y_p\right)$ is not a linear function of tilt angle θ, it is also dependent on incident angle $\gamma_{\left(x_p, y_p\right)}$ which is affected by the shape of the test optics and geometry of the test configuration. The slope change in the other direction $\Delta S_x\left(x_{p,} y_p\right)$ is even more complicated as shown in Eq.(3.22). A ray tracing software such as Zemax is suggested to get exact value of slope error.

Slope error due to display tilt about the other direction (y) can be derived using the similar procedure described above.

3.2.4 Sensitivity on display axial position

Test sensitivity on display axial position is similar as sensitivity on camera axial position as described in Sec. 3.2.2. If the display axial shifts Δz, then defocus ΔW_{020} is introduced in the measured wavefront departure, and $\Delta W_{020} = \frac{1}{8 f_{\#}^{\ 2}} \Delta z$

3.2.5 Sensitivity on mirror tilt

Measurement uncertainty due to mirror tilt can be decomposed into equivalent amount of error coming from camera lateral position and display tilt, the sensitivity of which are analyzed in Sec.3.2.1 and Sec. 3.2.3.

3.2.6 Sensitivity on mirror clocking

Error in mirror clocking (rotation of the mirror about its surface normal) could introduce measurement error. The sensitivity ($\frac{\partial Z(r,\theta)}{\partial \theta}$) is the first order partial derivative of the surface prescription of the test mirror. Mirror clocking error happens on test mirror which is non-axial symmetrical, such as the off-axis segment of the primary mirror of Giant Magellan Telescope.

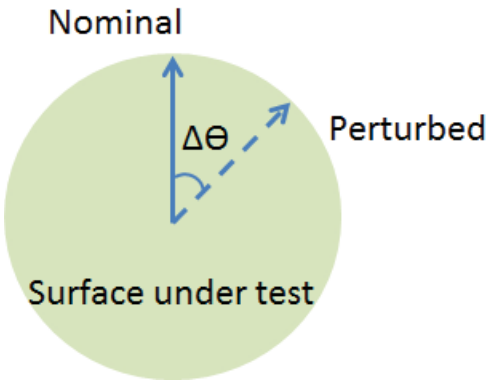

Figure 3.7 Layout showing uncertainty in mirror clocking

For a clocking error of $\Delta\theta$, the measured surface error would be

$$\Delta Z = \Delta\theta \frac{\partial Z(r,\theta)}{\partial \theta} \tag{3.23}$$

Z is the nominal surface shape of the test mirror as a function of r and θ .

3.2.7 Summary of geometry sensitivity

The above analysis uses imaging aberration theories to derive parametric expressions of test sensitivity on geometry. Calculations in Sec.3.2.1 use Seidel coefficients to illustrate sensitivity of field dependent wavefront departures (astigmatism and coma) on camera lateral position which assumes axisymmetric test surface and paraxial conjugate of camera and display about test surface. The spot distribution on the display can be calculated using transverse ray aberration theory (Eq.(3.2) and Eq.(3.3)). The calculation can hold a good accuracy if the camera and the display are not far away from the conjugate positions. To get exact spot distribution on the display, a rigorous ray trace should be performed when the test is far away from conjugation position. However, you can still use the sensitivity equations above to get a quick and good estimation of test sensitivity on geometry in the initial design of a SCOTS test.

3.3 Reduced geometry sensitivity using on-axis test configuration

From the analysis in Sec. 3.2.1 and Eq.(3.15) it can be seen that the sensitivity of astigmatism is proportional to camera lateral position h, indicating that under same amount of measurement uncertainty on camera lateral position Δh, test configuration with large amount of off-axis separation between camera and

optical axis of the test optics is vulnerable to large error of ΔW_{222} , as shown in Eq.(3.24).

$$\Delta W_{222} = \frac{\partial W_{222}}{\partial h}\Delta h = \frac{2hr^2}{Rd^2}\Delta h \tag{3.24}$$

Therefore, we can infer that although SCOTS allows off-axis configuration, for axial symmetric optics, if we can maintain coaxial alignment of the camera, display and test optics in the measurement, aberration sensitivity (especially astigmatism) to geometry errors can be reduced. The coaxial alignment can be implemented by use of a beamsplitter and the test configuration is shown in Figure 3.8.

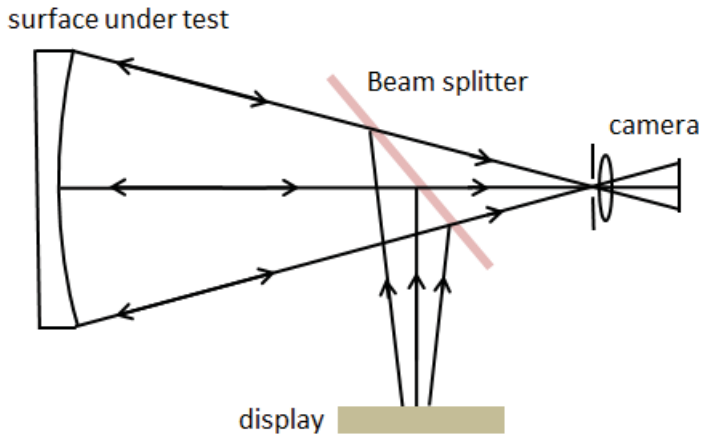

Figure 3.8 Layout of an on-axis SCOTS test configuration by using of a beamsplitter

However, beamsplitter inherently adds errors to the measurement. Several issues need to be considered when designing the test and budgeting the system

error. The potential measurement errors coming from the beamsplitter include the effect of beamsplitter thickness, base shape and thickness variation.

Firstly, to consider the effect of constant thickness, the beamsplitter is treated as a plane parallel plate (PPP), which causes a lateral displacement of the rays passing through. For small angles, the lateral displacement D can be approximated as [26]

$$D \approx \frac{TI(\mathrm{n}-1)}{n} \tag{3.25}$$

where T is the thickness of the beamsplitter and I is the incident angle on the beamsplitter.

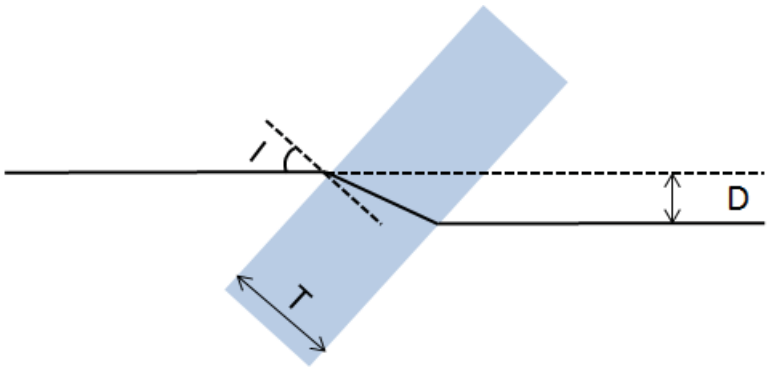

Figure 3.9 Lateral displacement of light caused by plane parallel plate

When a PPP is used with collimated light, there is no aberration introduced. However, in a SCOTS test, as shown in Figure 3.10, the beamsplitter is used with converging light where astigmatism, coma, and spherical aberrations arise. The reason for the aberrations is that in the converging beam, rays with large incident angle will be displaced more than small angles. Therefore, test optics with larger

numerical aperture (NA) will be more vulnerable to this effect. One way to minimize this effect is to use pellicle beamsplitter which only has 2-μm thickness instead of common plate beamsplitter which is about 5-mm thick. And it is implemented in the test of the secondary mirror of Large Binocular Telescope which will be discussed in Sec. 3.4.

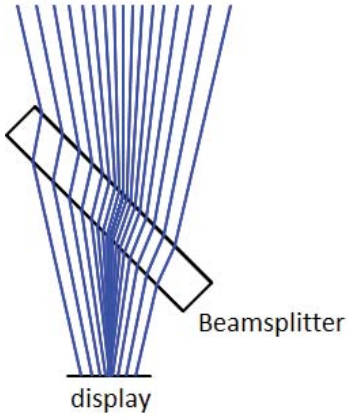

Figure 3.10 Aberrations occur in SCOTS since the beamsplitter is used with converging lights.

Secondly, the effect of base shape deviation of the beamsplitter from ideal flat also needs to be considered, especially for a pellicle beamsplitter. Due to the extremely thin thickness, the base shape of pellicle beamsplitter can be easily distorted by the mounting frame and air turbulence in the environment. One of the possible distortions is a quadratic shape bending, it would introduce extra power in focusing the coming lights.

Finally, the thickness of the beamsplitter varies due to wedge and some other surface imperfections, which would also introduce error in the measured surface

map. The thickness variation of the beamsplitter can be measured in transmission with a Fizeau interferometer by comparing measurement results with and without the beamsplitter in the light path.

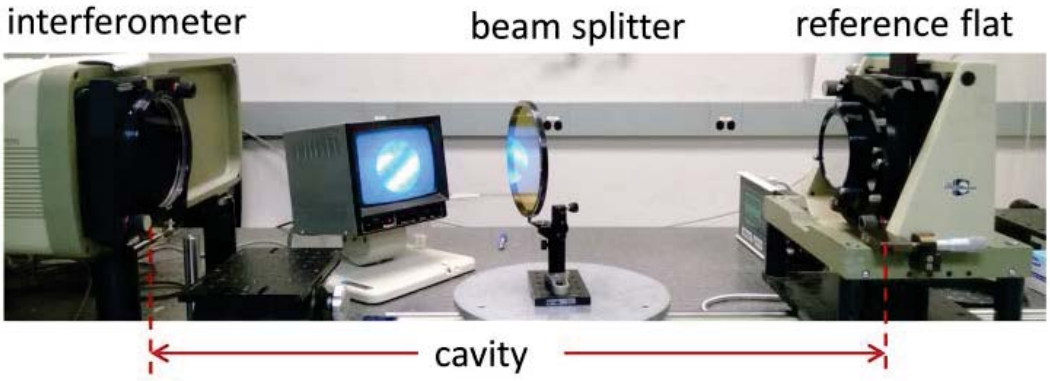

Figure 3.11 Experiment setup to check thickness uniformity of a pellicle beamsplitter

3.4 On-axis SCOTS for the secondary mirror of Large Binocular Telescope

Large Binocular Telescope Observatory (LBTO) noticed varying astigmatism (~10um RMS) in one of its secondary mirrors with change of mirror elevation. The secondary mirror is an f/1.1 deformable ellipsoid with 910 mm diameter and 231 μm aspheric departures. To help the observatory investigate this problem without requiring additional geometry measurement instrument such as laser tracker, I designed and constructed an on-axis SCOTS system for the observatory. The test aligned the camera and screen on the optical axis of the test mirror with the help of a 6-inch pellicle beam splitter. The SCOTS was constructed on a 16 inch by 16 inch breadboard as shown in Figure 3.12. The whole system was very

compact and flexible to be used at multiple gravity angles. Details about the system components are listed in **Table 3.1**.

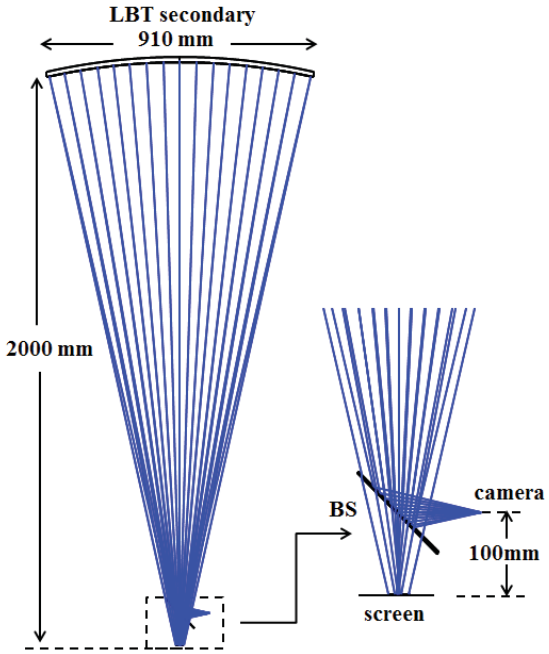

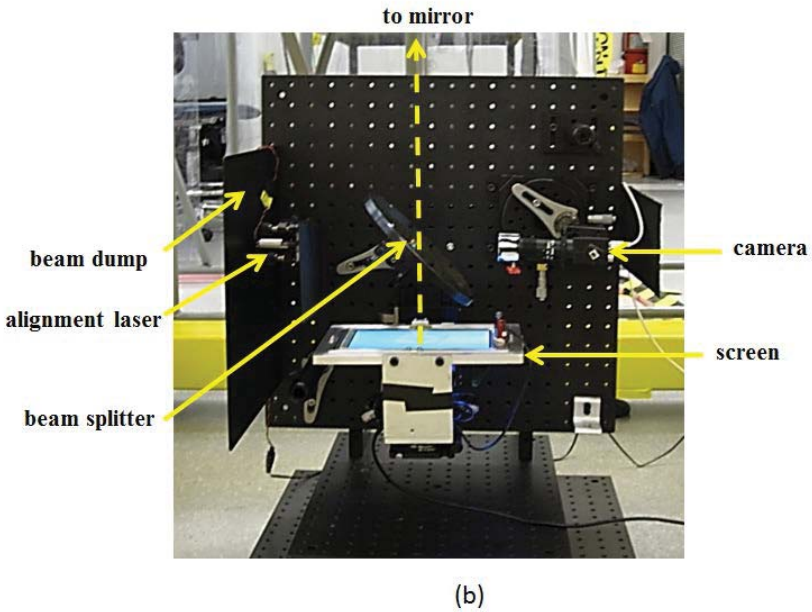

Figure 3.12 (a) Geometry layout of the test configuration and (b) Experiment setup

Table 3.1. Specification of SCOTS components for LBT secondary

	Brand	Specs
LCD Display	MIMO-UM-710S	Resolution:800*480, pixel pitch 0.1905 mm
CCD	Point Grey	FL2-08S2M-C, 1/3", pixel pitch 4.65μm
Camera lens	Marshall Electronics	V-PL60CS, f/1.8, focal length: 6 mm
Camera stop	National Aperture	1 mm round aperture(1-1000)
Beamsplitter	Edmund Optics	6 inch, pellicle, 50R/50T

3.4.1 Estimated beamsplitter effect

To simulate the effect of constant thickness of the beamsplitter, 2 μm thickness was added to the beamsplitter in LBT secondary SCOTS test Zemax model , the ray tracing result showed that it merely generated 3.4 nm RMS wavefront error (3 nm astigmatism, 0.4 nm coma and spherical). Therefore, measurement error coming from the constant thickness of the beamsplitter can be ignored for this test which does not require nm accuracy.

Simulation was also performed on a curved base shape of the pellicle beamsplitter with 1λ ($\lambda \approx 500nm$) PV surface departure. The results showed it would cause 17nm RMS measurement errors (mainly astigmatism). For the requirement of LBT secondary SCOTS test, this effect can also be ignored.

Thickness variation of the beamsplitter was measured using the test setup shown in Figure 3.11. The results are given in Figure 3.13. As shown in Figure 3.13(a), there are low-order thickness fluctuations (2-4 cycles/aperture) in the beamsplitter. Figure 3.13 (b) is the integrated 1-dimensional power spectral

density plot (PSD(υ)) of the difference map (Figure 3.13 (a)). The RMS value at certain spatial frequency can be calculated using Eq.(3.26) [27].

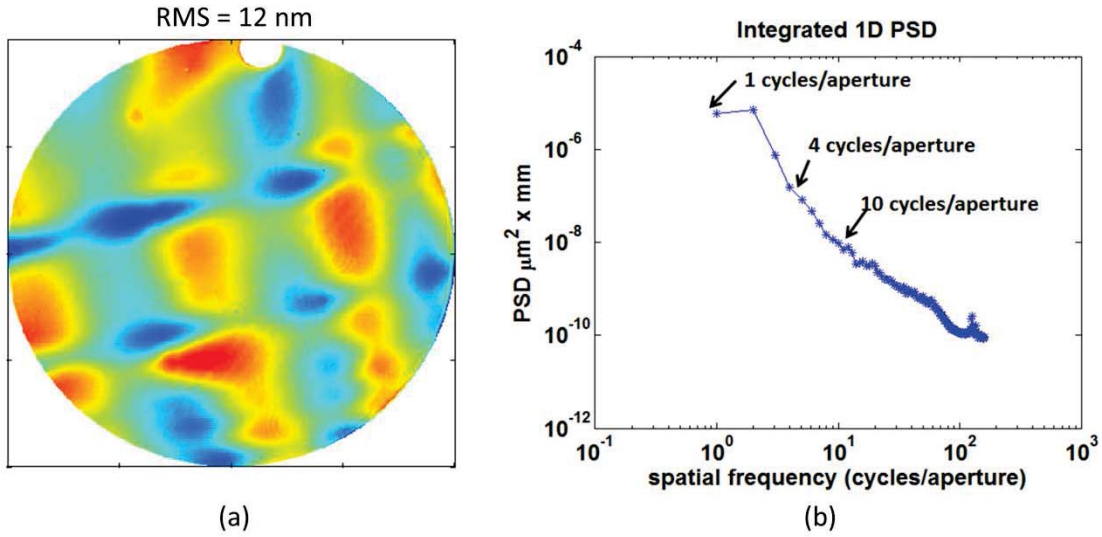

Figure 3.13 (a) difference map by comparing measured flat surface with and without beamsplitter in the light path.(b) 1-dimensional PSD of (a).

$$rms = \sqrt{\int_{\upsilon 1}^{\upsilon 2} PSD(\upsilon) d\upsilon} \tag{3.26}$$

Based on the PSD analysis, three sinusoidal shape error at 1 cycle/aperture, 4 cycles/aperture and 10 cycles/aperture with RMS amplitude of 3 nm, 0.5 nm and 0.05 nm respectively, were added to the front surface of the beamsplitter in the ZEMAX model. The ray trace result showed that the introduced measurement error was on the level of 1 nm RMS in the wavefront deformation and 10^{-8} rad in wavefront slope deviation, which were also negligible.

3.4.2 Alignment procedure

The on-axis SCOTS design requires a good control of the alignment to make sure that all the elements, the test mirror, camera and screen aligned coaxially. For the LBT secondary SCOTS test, the alignment was designed to be easily implemented in the observatory without using complicated geometry measurement instrument, such as a laser tracker. The entire test alignment was separated into two steps. The first was the in-lab integration of the SCOTS package with pre-alignment of the components. The second step was the alignment between the test mirror and the SCOTS package at the observatory.

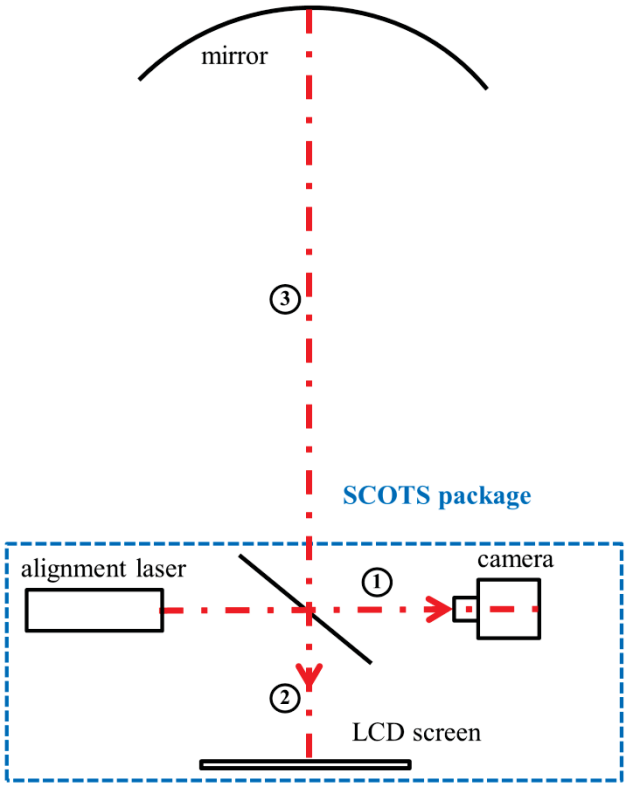

Figure 3.14 Illustration of alignment procedure for LBT secondary SCOTS test

In the SCOTS system package, an alignment laser was placed on the opposite side of the beamsplitter to the camera (Figure 3.14) sending a collimated beam to the beamsplitter with half of the light transmitted and half reflected. The laser beam served as the reference optical axis for the system. The first step of the pre-alignment procedure (Figure 3.14 ①) was to align the camera aperture and the center of the CCD onto the laser beam. The camera was translated so that the laser beam with diameter of approximately 1mm was able to go through the external aperture of the camera, which was also 1mm in diameter. Subsequently, by tilting the camera and monitoring the centroid of the laser beam incident on the CCD, the laser beam was positioned in the center of the camera sensor, within ~0.1 pixel accuracy. The second step of the pre-alignment (Figure 3.14 ②) was aligning the LCD screen to be perpendicular to the laser beam by adjusting its tip-tilt so that the laser beam reflected by the screen went back through the aperture of the alignment laser. The position where the laser beam was incident on the LCD screen was recorded for the second alignment step. With these pre-alignment steps, the SCOTS package was sent to the observatory.

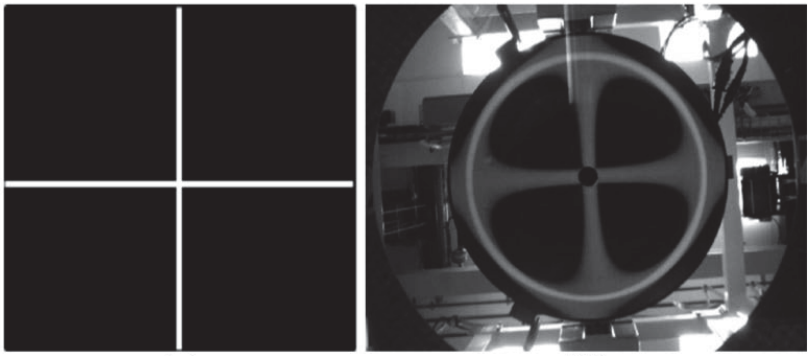

Figure 3.15 . (a) A bright cross on the screen was lit up to illuminate the mirror. (b) Reflected image of the cross captured by SCOTS camera

Before the test, the SCOTS package was aligned with the secondary mirror (Figure 3.14 ③) so that (1) the mirror is centered on the CCD and (2) the mirror is perpendicular to the SCOTS system axis. The mirror centering was controlled to approximately 0.2 mm accuracy by fitting a circle to the image of the mirror boundary (the image was taken with room light, the center of the circle could be calculated with sub pixel accuracy on the CCD). The major challenge in aligning the secondary mirror normal to the optical axis was due to its central obscuration, which prevented us from using the alignment laser for this task. Instead we used a bright cross (see Figure 3.15(a)) produced by the LCD screen at the previously recorded center position. By adjusting the mirror tip-tilt until the mirror and the bright cross image were centered on the CCD (as shown in Figure 3.15 (b)) the mirror was aligned with its vertex perpendicular to the optical axis. Considering the limitation of the mechanical mounting of the mirror and the width of the

reflected cross we estimated that the mirror tilt was aligned within 0.1 degree accuracy.

It is worth mentioning that the coaxial alignment of camera, LCD screen and test mirror also made the camera view of the secondary mirror free from perspective distortion which many SCOTS systems struggled with and had to calibrate out by putting customized fiducial targets on test mirrors.

3.4.3 Measurement results

The performance of the low-order aberration measurement of this SCOTS was first verified with the secondary mirror pointing straight down as shown in Figure 3.16 (a). At this position, SCOTS measured approximately 0.2 μm (RMS) astigmatism. This 0.2 μm (RMS) might be the combination effect from alignment uncertainty, systematic error in SCOTS, and a small amount of inherent errors in the secondary mirror.

Figure 3.16 . SCOTS test of the secondary mirror at (a) zenith position and (b) 30-degree elevation position

After the initial measurement, a series of controlled aberration, 1μm astigmatism (RMS), 1μm coma (RMS) and 1 μm trefoil (RMS) wavefront errors were intentionally added using the deformable secondary mirror. SCOTS accurately measured these aberrations with sub-μm accuracy. The wavefront maps shown in Figure 3.17 are the commanded wavefronts, measured wavefronts and the differences.

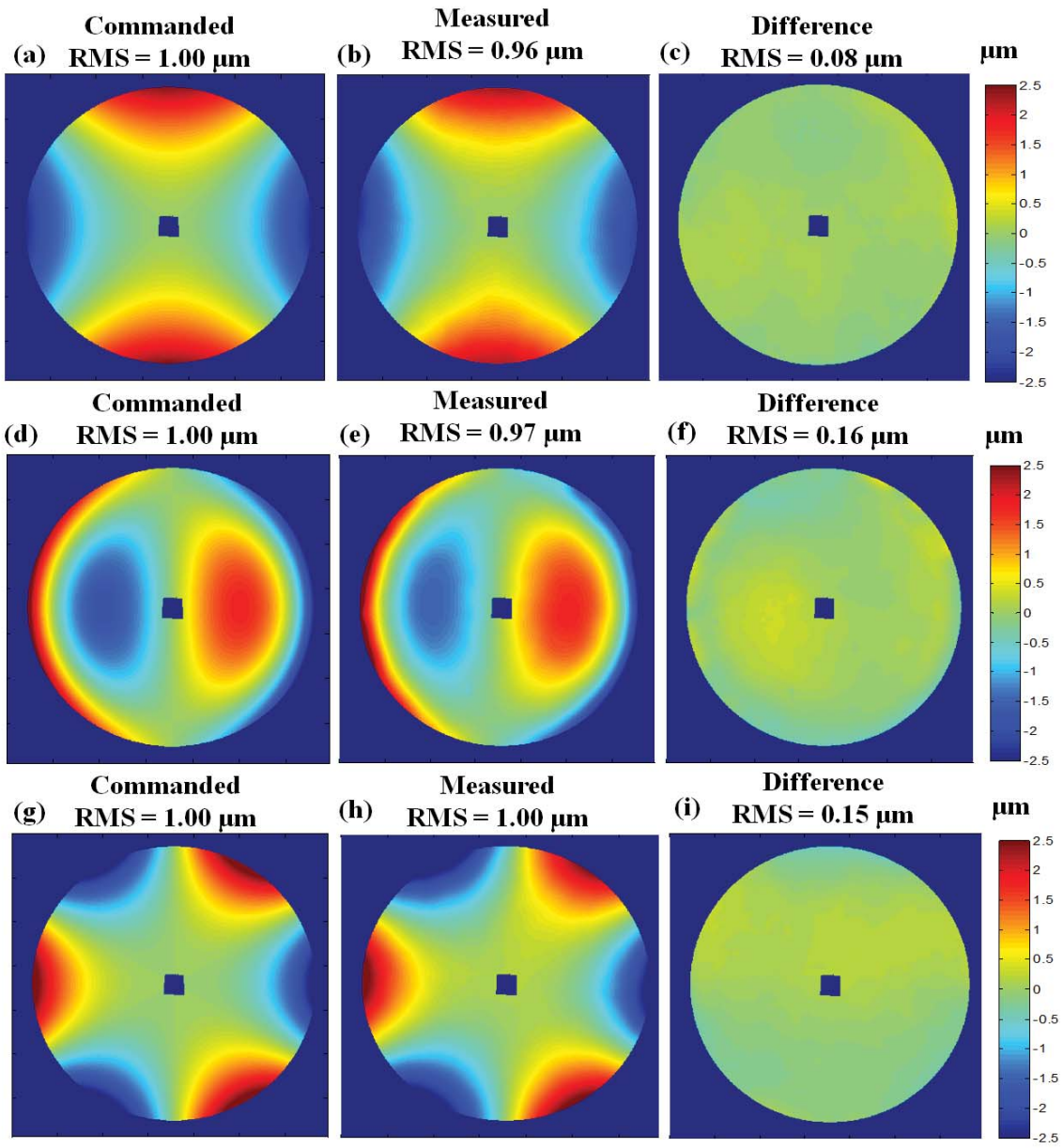

Figure 3.17 SCOTS measurement results with controlled aberration in secondary mirror. Unit: μm. (a),(d) and (g) are commanded wavefront aberrations which are 1 μm RMS astigmatism, 1 μm RMS coma and 1 μm RMS trefoil, respectively. (b),(e)and (h) are SCOTS measured wavefront aberrations. (c),(f) and (i) are the differences between commanded and measured wavefront aberrations.

After the verification tests with the secondary mirror pointing straight down, the observatory used this SCOTS system at 30-deg elevation to test the elevation dependency of the astigmatism. Figure 3.16(b) shows the test configuration at 30-deg elevation (i.e. optical axis at 60-deg from vertical). Moving the mirror to 30-deg elevation introduced a large amount of astigmatism, the value of which is a function of the path followed (hysteresis). SCOTS measurement showed that reaching 30-deg elevation from vertical position caused ~ 6.2 μm RMS astigmatism but only ~3.7 μm RMS astigmatism when the position was reached from horizon pointing (i.e. optical axis horizontal). This test result confirmed previous measurements taken with the unit installed at the telescope, including the hysteretic behavior of the introduced aberration.

Several other SCOTS measurements were also done after modifying the secondary mirror hardware configuration in an attempt to determine the causes of this aberration. Although no direct cause was found, the measurements eliminated several potential causes. It also helped the observatory to design a series of tests to further investigate the source of the astigmatism.

4 DISPLAY AND CAMERA CALIBRATION FOR HIGH ACCURACY SURFACE MEASUREMENT

In this chapter, the performance of the other two important test components, display and camera are analyzed thoroughly. Sec. 4.1 mainly discusses the performance and calibration of SCOTS display. Sec. 4.2 focuses on the camera calibration including distortion mapping correction using vision rays and simulation of aberration effect. A test system for measuring the primary mirror of Daniel K. Inouye Solar Telescope [28] implementing the comprehensive calibrations discussed in this chapter is presented in Sec 4.3.

4.1 Calibration of SCOTS display

The calibrations of SCOTS display discussed in this section include three major aspects: the thickness of display cover glass, intensity nonlinearity and bending of display shape.

4.1.1 Display cover glass

SCOTS uses a commercial LCD to generate fringe pattern where the LED light source is located behind several layers of cover material with certain thickness *t*.

Refraction occurs at the screen and air interface and causes a shift of illumination screen pixel position.

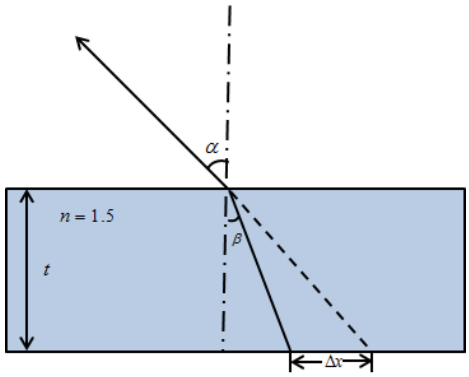

Figure 4.1. Illumination pixel position shift due to the cover glass.

The amount of shift Δx can be derived by Snell's law

$$\Delta x = t \cdot \left\{ \tan\alpha - \tan\left[\sin^{-1}\left(\frac{\sin\alpha}{n} \right) \right] \right\} \tag{4.1}$$

From the equation above, the shift Δx is dependent on the thickness of the cover glass (t), refractive index (n) and illumination angle (α). The thickness (t) and refractive index (n) are the intrinsic parameters of an LCD display which are determined by its manufacture. Thick glass and high refractive index cause large shift and therefore increase the measurement uncertainty. The illumination angle (α) varies for different test configurations depending on the test optics. For most SCOTS tests, the camera and the screen are configured near the center of curvature (CoC) of the test optics forming a stigmatic pair to have loose sensitivity on camera mapping; and in this scenario, the maximum illumination

angle (α) is approximately equal to the numerical aperture (N.A.) of the test optics. Therefore, testing of fast optics has larger screen pixel shift Δx than testing slow optics.

4.1.1.1 Measuring and compensating the thickness of cover glass

In some test cases, the cover glass introduced measurement error can be partly cancelled out during a reference calibration (Chapter 5). In other test cases when calibration with a reference surface is not available, the thickness of the cover glass needs to be measured and compensated in the measurement data as well as in the ideal ZEMAX ray trace model. Figure below shows an example of using an optical CMM to measure the thickness of the cover glass.

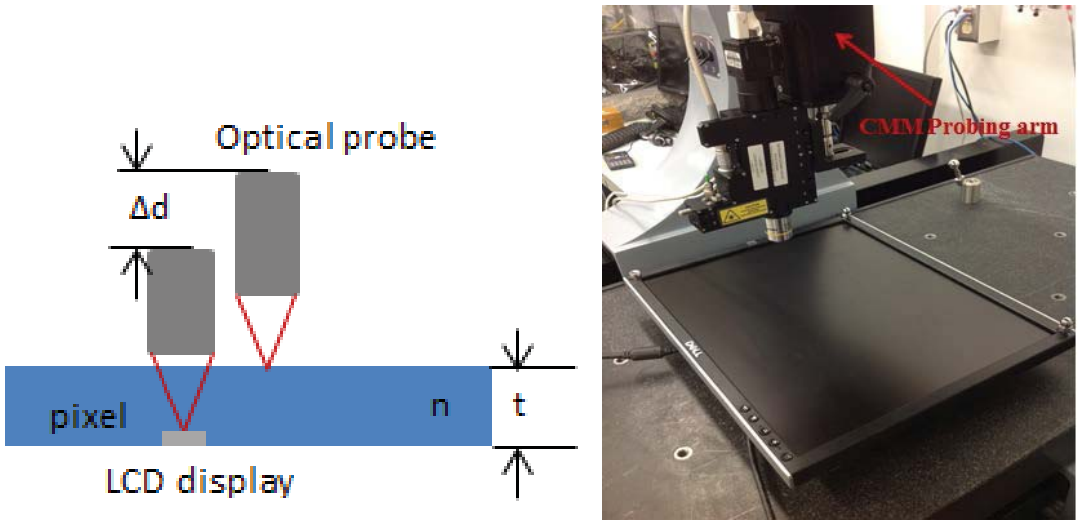

Figure 4.2 Schematic and experimental setup for measuring display thickness

In the measurement, several screen pixels are lit up through control software. By moving the probe, the objective on the optical CMM firstly focuses on the

front surface of the LCD and subsequently on the luminous pixel. The move distance (Δd) is recorded by the CMM. Assuming an averaged refractive index (n), the thickness (t) of the cover glass can be estimated as

$$t = \Delta d \cdot n \tag{4.2}$$

Objective with large NA is recommended to be used in optical probe since its small depth of field gives better visual focusing justification. Usually more than one point is measured and the averaged result is used to give a best estimation of the display thickness.

The thickness of commercial displays varies depending on the manufacturing technique. It can range from 0.5 mm~ 2 mm. The one that is used for SCOTS test of primary mirror (M1) of Daniel K. Inouye Solar Telescope (DKIST) is a Dell 30" LCD display with model number U3014, the measured thickness of the cover glass is 0.675 mm assuming an averaged refractive index of 1.5.

To compensate the effect of display cover glass, in the "virtual null" Zemax ray tracing model, the display plane is no longer modelled as a single plane but a slab with measured thickness and refractive index so that ideal ray tracing can take refraction at display and air interface into account.

To evaluate final surface measurement error caused by the cover glass, we took DKIST M1 as the example (detailed test descriptions are provided in the last

section of this chapter). The mirror diameter is 4.2 meter and the testing distance from SCOTS to the mirror is ~ 17 meter, so angle α in Eq. (4.1) is in the range of [-7^0, 7^0]. Using Eq. (4.1), cover glass with 0.675 mm thickness and an averaged refractive index n = 1.5 would cause maximum ± 27.8 μm lateral illumination pixel shift, which corresponds to ± 0.8 μrad PV surface slope error. The simulated final surface measurement error is ~ 250 nm RMS and is plotted in Figure 4.3. The dominated error is Zernike power term (Z_4).

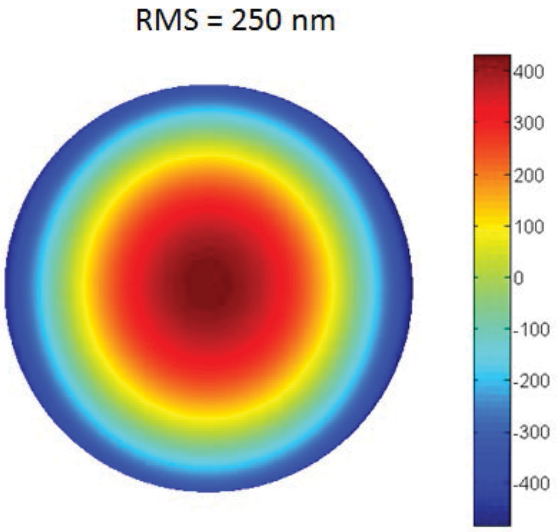

Figure 4.3 Simulated SCOTS measurement error of DKIST M1 due to display cover glass. The simulation is done by comparing test model in Zemax with and without a layer of glass in front of the display.

4.1.2 Display nonlinearity

The luminance of commercial LCD displays used in SCOTS tests is usually nonlinear for better human visual perception that has greater sensitivity to

relative differences between darker tones than between lighter ones. However, camera responses differently to the luminance as human eyes; the intensity sinusoidal fringe generated by the display is not real sinusoidal seen by the camera if the nonlinear effect is not addressed. Similar to fringe projection, display nonlinearity mainly leads to fringe print-through artifact in SCOTS measured surface map.

4.1.2.1 Calibration of display nonlinearity

There are different ways to correct the nonlinear effect of the display. Measuring the gray-scale curve and building a look up table is one of the mostly used methods [29]. We applied this method in calibrating the nonlinear effect of display in SCOTS measurement. Example below shows the nonlinearity calibration of the display for DKIST M1 SCOTS test.

In the calibration, the display was set up to display grey scale with constant step from minimum to maximum. A camera was used to capture the intensity image and the averaged intensity of a 10*10 pixel center area of the camera is recorded as the measured grey scale. The measured gray-scale curve was fitted using up to fifth-order polynomials, as shown in Figure 4.4. An inverse function (look-up table) was then built, as shown in Figure 4.5. Figure 4.6 is the measured camera response after correction of display nonlinearity.

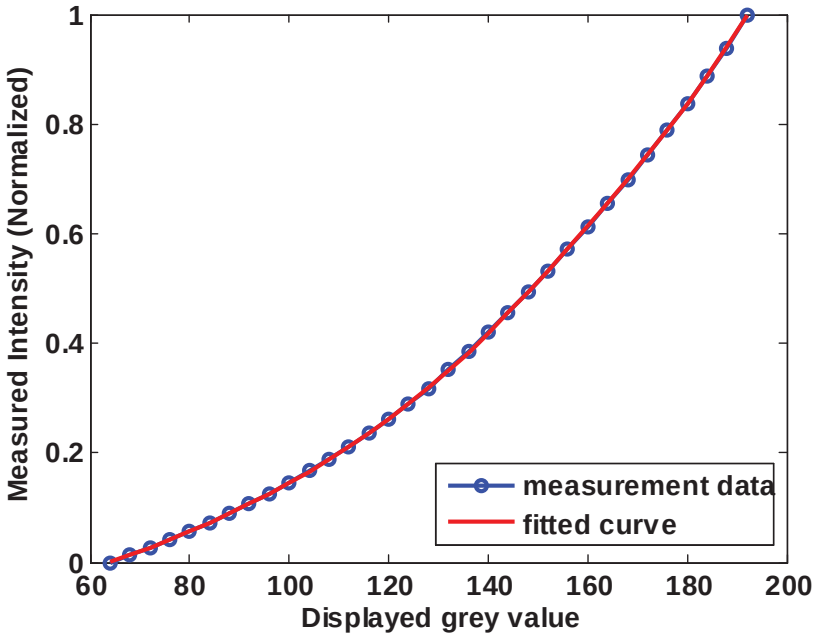

Figure 4.4 Measured gray-scale and the fitted curve before display linearity compensation

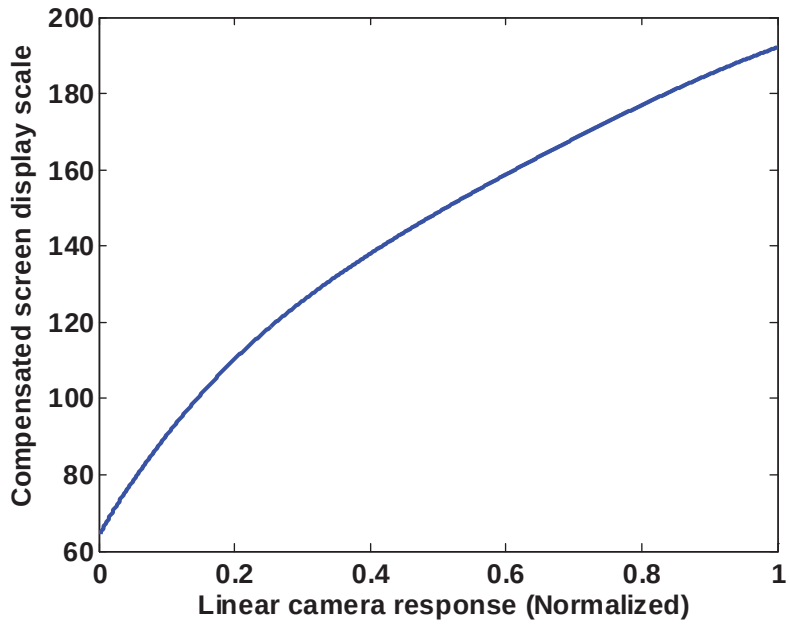

Figure 4.5 Look up table based on the inverse function of the fitted curve in Figure 4.4

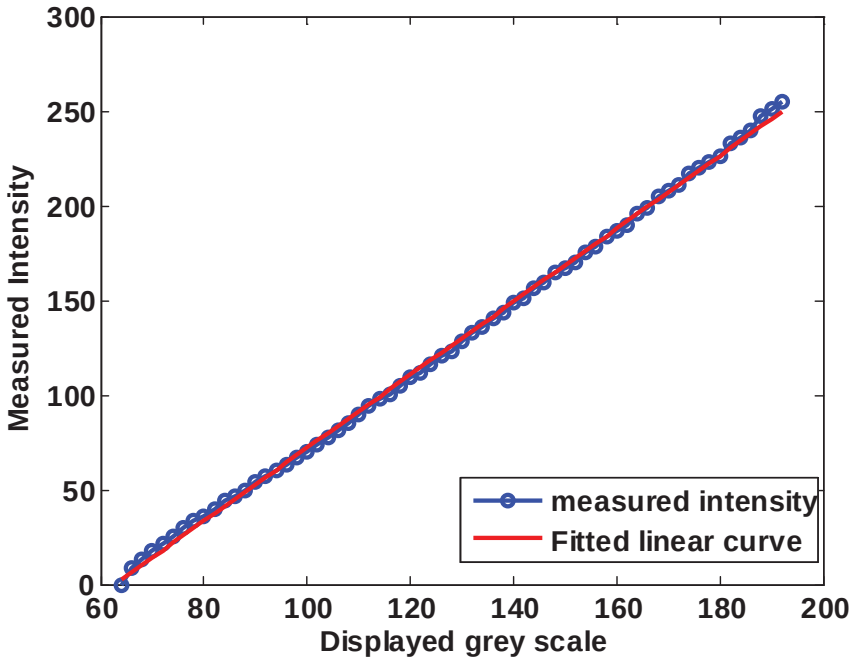

Figure 4.6 Measured gray scale and the fitted linear curve after LCD nonlinearity compensation

4.1.2.2 SCOTS measurement with calibrated linear display

Figure 4.7 (a) and (b) are SCOTS measured surface map of DKIST M1 during polishing stage before and after display nonlinearity compensation. The fringe print-through effect in the surface map is greatly reduced after display nonlinearity compensation. The print-through artifact can be further reduced by using more shifting steps or increasing the fringe density [30,31], and the result is given in Figure 4.7 (c).

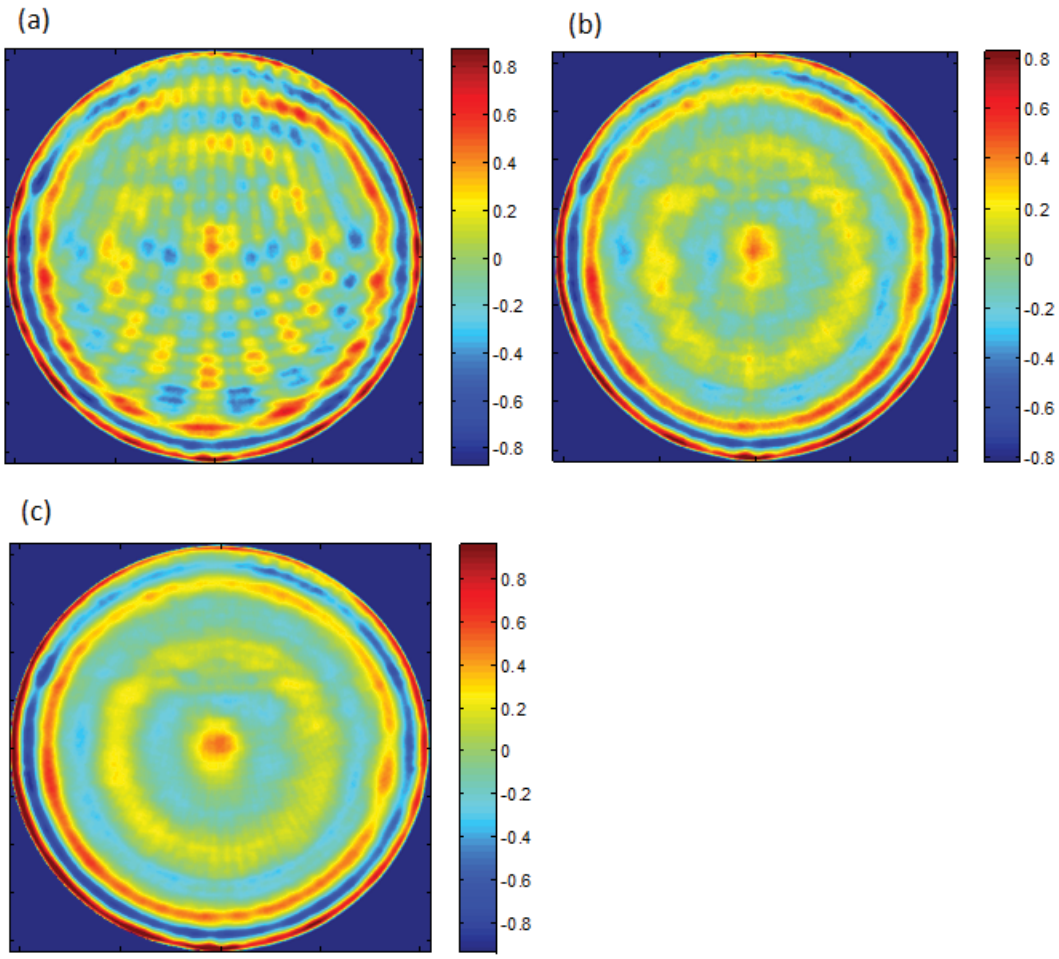

Figure 4.7(a) Measured surface map of DKIST M1 during polishing stage using 4 step phase shifting without display nonlinearity compensation (b) Measured surface map using 4 step phase shifting with display nonlinearity compensation (c) Measured surface map by using 16 step phase shifting with display nonlinearity compensation.

Literature [32] shows that the nonlinearity of LCD display is even more complicated as it is viewing-angle dependent, and the angular dependency of the nonlinearity is much more obvious when there is a large viewing angle change (for example, from 0^0 ~ 60^0). This can be a difficult problem for multi-camera system where the cameras are mounted with large angular separation, since it is

impossible to calibrate the display to be linear in all the viewing directions. One way to solve this problem is to use medical clinical displays which are designed to have great uniformity across the display.

4.1.3 Display shape deformation

Most SCOTS tests using phase-shifting technique and in the data processing the display surface is assumed to be perfectly flat with even pixel spacing so that we can convert the unwrapped phase value of each mirror pixel to the luminous display pixel position by applying a scale factor, where

$$\begin{aligned} x_{measured} &= \frac{\varphi_x}{2\pi} T_x \\ y_{measured} &= \frac{\varphi_y}{2\pi} T_y \end{aligned} \tag{4.3}$$

$x_{measured}$ and $y_{measured}$ are measured luminous pixel positions; T_x and T_y are displayed fringe periods in x and y direction which are determined by the fringe density (pixels/period) and the display pixel pitch (mm); φ_x and φ_y are unwrapped phase values.

However, in real situation, the shape of the LCD display is highly possible to be distorted or bent due to the fabrication uncertainty, mechanical mount, gravity, and etc. Shape deformation of the display changes the luminous pixel positions in x, y and z directions, which means the pixel spacing between two individual pixels (and thus fringe period T_x and T_y) is no longer a constant value

but varying with the local surface shape of the display. We cannot simply use a constant scale factor (T_x and T_y) to convert phase value into luminous pixel position from unwrapped phase map as described in Eq.(4.3). Otherwise, systematic error could be introduced in the measurement. The shape deformation is much more severe especially when a relatively large display is used in the test.

4.1.3.1 Measuring display shape deformation

To compensate the measurement error introduced by display shape deformation, we propose to calibrate display pixel position in 3D (x, y and z direction) so that we can take care of the varying pixel pitch (e.g. pixel lateral position x and y) in the measurement data and compensate the shape (e.g. pixel axial position z) in the ideal ZEMAX ray trace model as well.

To correctly measure and model the display shape, we need to measure the actual shape of the display in its final mounting frame and at the same orientation as it is in the test. For the test configurations where the SCOTS display needs to be facing up, PSM connected optical CMM (shown in Figure 4.2) can be used for the calibration. However, for applications where the SCOTS display needs to be facing down, like the one for DKIST M1 (mirror sits on the polishing table and is facing up), an upside down optical CMM is needed to measure the display shape deformation. Figure 4.8 and Figure 4.9 shows the

constructed calibration setup for calibrating the display shape deformation for SCOTS test of DKIST M1 using PSM and a laser tracker. The PSM was mounted on a xyz translation stage, and the focus point of the PSM was first calibrated and registered to 3 SMRs on the PSM as shown in Figure 4.8 using laser tracker. This process was referred as PSM pre-calibration. After the PSM pre-calibration, the PSM was then translated to focus on several display pixels. At each focus position, the SMRs on the PSM were measured by the laser tracker; and the display pixel positions (x, y, z) were calculated using the PSM pre-calibration information. Finally, all the calibrated display pixel positions were registered to the 4 reference SMRs on the display frame with the laser tracker. Once in the real test, by measuring the 4 reference SMRs on the display frame, the screen shape and all the pixel positions in test geometry can be retrieved using the calibration information.

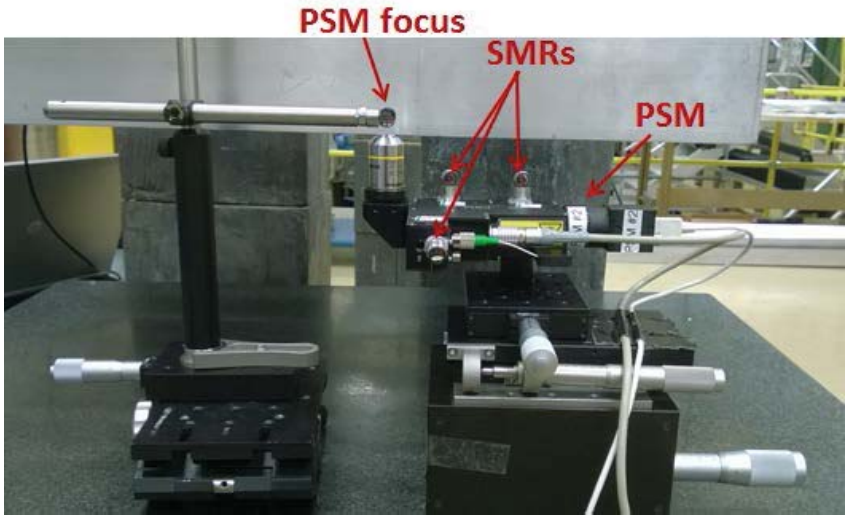

Figure 4.8. Setup for registering PSM focus position to three SMRs on the PSM.

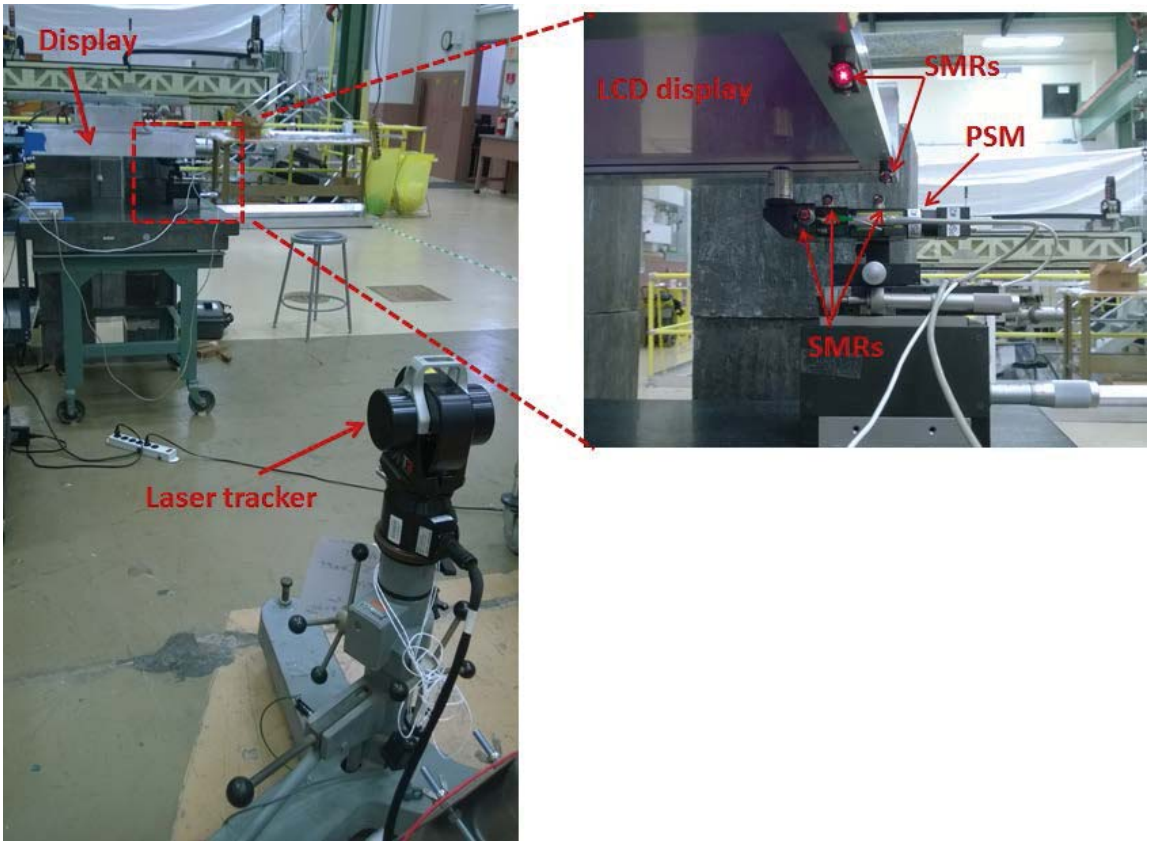

Figure 4.9. Setup to measure display shape deformation and register its pixel position to the reference SMRs for DKIST primary SCOTS test system.

For the display used in DKIST M1 SCOTS test, 20 pixels sampled in a display area ~400 mm * 640 mm were measured. At each pixel position, the measurement was performed 4 times and the averaged result was used to reduce measurement noise. The display surface (x, y, z) was estimated by fitting the measured 20 pixel positions using 2D Chebyshev polynomials [33] up to quadratic term with fitting residual around 5 μm RMS. Higher order surface shape fitting was not used to avoid introducing artificial high-order errors. Figure 4.10 shows the fitted

display shape of SCOTS system for DKIST M1. The display is cylindrically curved along the short dimension of the display with ~0.8 mm PV departure from an ideal flat plane which corresponding to a radius of curvature ~25 meter. Measurement also shows that the display bends towards gravity which indicates gravity might be a major cause of display shape deformation.

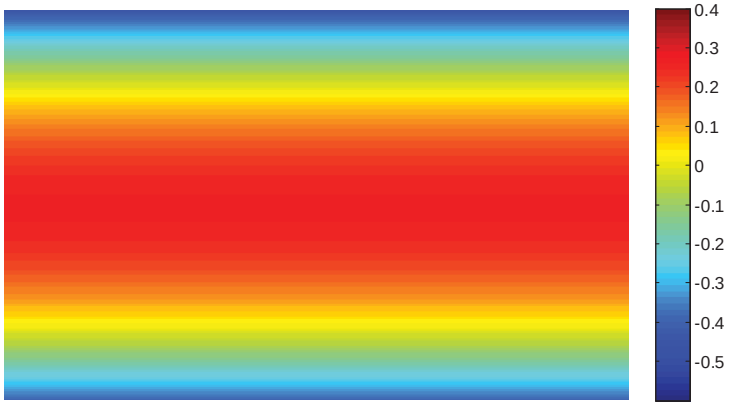

Figure 4.10 Fitted display shape in the final mounting frame of DKIST M1 SCOTS.

If the shape deformation of the display (assuming the display is curved along one direction with radius of curvature ~25 meter based on the measurement result in Figure 4.10) is not compensated in the measurement model, it would create 275 nm RMS surface measurement error in DKIST M1. The simulated error map is plotted in Figure 4.11. The dominated error is Zernike power term (Z4), which is ~260 nm RMS; but it also includes a small amount of astigmatism (~20 nm RMS), coma (~70 nm RMS) , spherical (~29 nm RMS) and ~37 nm RMS high-order surface error after removing up to Zernike 11 (spherical) term.

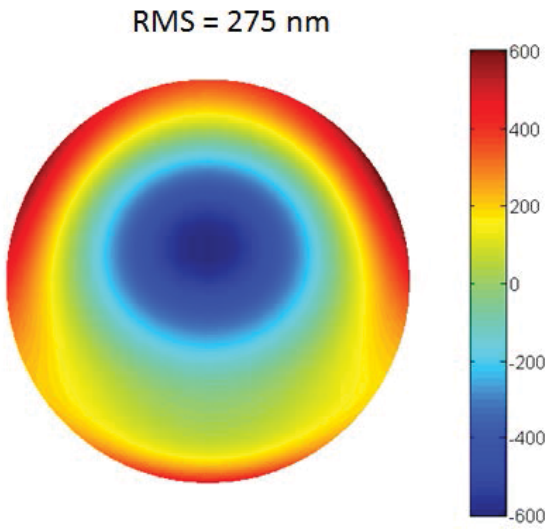

Figure 4.11 Simulated SCOTS measurement error of DKIST M1 due to display shape deformation

4.1.3.2 Display shape measurement uncertainty

The accuracy of the method described in Sec 4.1.3.1 measuring the shape deformation of the display is limited by the accuracy of the laser tracker, stability of the setup and the sampling points on the display. Without putting great effort to re-design and build the calibration setup, increasing the sampling points gives much more fidelity on the fitting result. To evaluate the calibration uncertainty of the example in Sec. 4.1.3.1 (display for DKIST M1 SCOTS), 10 out of the measured 20 pixel points of were selected to repeat the fitting and compared with the result using total 20 points. The comparison shows that there was about 2 μm RMS uncertainty. For testing of DKIST M1, the difference would cause 10^{-8} rad RMS slope uncertainty in the measurement as shown in Figure 4.12; and 16

nm RMS in surface map, which is dominated by low-order surface shape (astigmatism) as shown in Figure 4.13 (a). After removing up to Zernike 11 term, the uncertainty in surface map is only 3 nm RMS, as shown in Figure 4.13 (b), which is well within the metrology uncertainty budget.

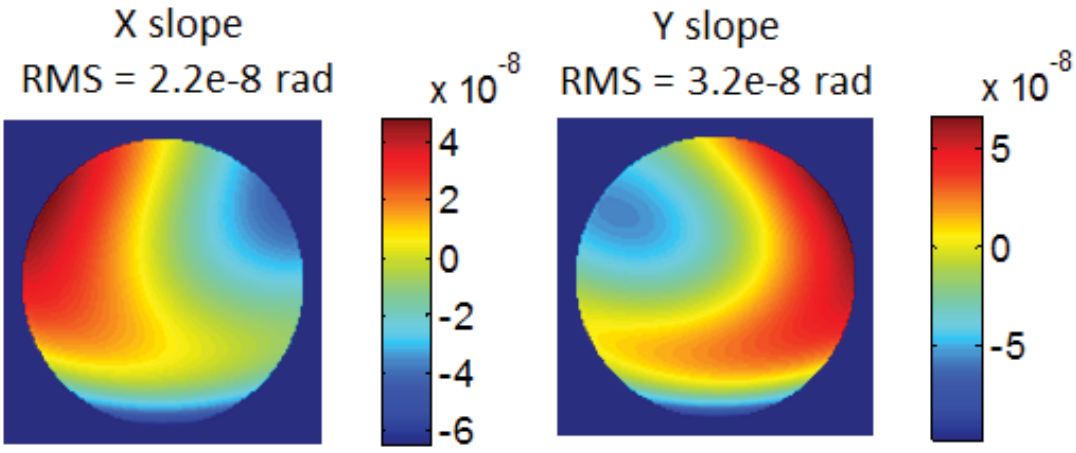

Figure 4.12.Estimated slope error due to display shape fitting uncertainty

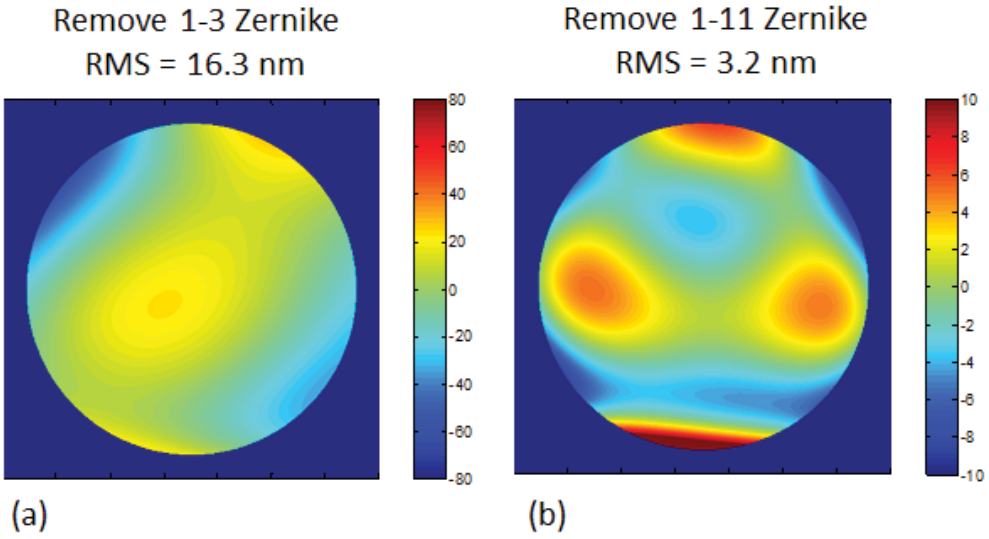

Figure 4.13. Integrated surface map of slope uncertainty in Figure 4.12

4.1.3.3 Compensate display shape deformation in the measurement

Shape deformation characteristic is localized on the display, to apply the calibration information in the real measurement; we need to know the absolute luminous pixel index and its position of each mirror pixel. However, usually the unwrapped phase map from phase shifting method only gives relative luminous pixel position ($x_{measured}$ and $y_{measured}$ in Eq.(4.3)) of each mirror pixel, to get absolute luminous pixel index without sacrificing test speed, the phase shifting and line scanning methods can be combined together: after collecting phase shifted fringe images, we spatially scan straight lines on the display in both x and y direction over a small region of the test mirror and centroiding the scan images. Having the information of scan start pixel, scan step and end pixel, the centroid data gives the absolute luminous display pixel indices of each mirror pixel in the scanned area. Selecting one mirror pixel in that region to offset the relative luminous pixel index calculated by phase shifting method, the absolute luminous display pixel index of each mirror pixel in the full aperture can be obtained. Then, applying the calibration data of the display pixel positions measured in Sec 4.1.3.1, spatially varied display pixel pitch is compensated in the measurement data ($x_{measured}$ and $y_{measured}$) of each mirror pixel. At the same time, the measured display deformation data is also used in Zemax ray trace of the test model so that the calculated (x_{ideal} and y_{ideal}) also take display shape effect into account.

4.2 Calibration of camera mapping

In SCOTS test, camera mapping calibration refers to the correction of non-uniform sampling in camera-captured images due to inherent distortion such as radial distortion, which will be discussed in Sec 4.2.1, and extrinsic perspective projection, which will be discussed in Sec 4.2.2.

4.2.1 Camera distortion

Almost all camera lenses have distortions. Distortion is magnification error varying with image height which maps straight lines in the objects to be curved lines in the camera image. Brown's model [34,35] is a common model describing camera distortion in computer vision which includes radial distortion and decentering distortion and thin prism distortion. Due to camera distortion, the image coordinate is shifted from its ideal position so that

$$\begin{aligned} x_d &= x + \Delta x \\ y_d &= y + \Delta y \end{aligned} \tag{4.4}$$

where x_d and y_d are distorted point coordinates, x and y are undistorted point coordinates, Δx and Δy are the amount coordinate shifts due to lens distortion. For radial distortion, it is defined as

$$\begin{aligned} \Delta x &= x(k_1 r^2 + k_2 r^4 + k_3 r^6 + ...) \\ \Delta y &= y(k_1 r^2 + k_2 r^4 + k_3 r^6 + ...) \end{aligned} \tag{4.5}$$

where k_1, k_2, k_3 are the radial distortion coefficients and $r^2 = x^2 + y^2$. Figure 4.14 shows the effect of camera radial distortion.

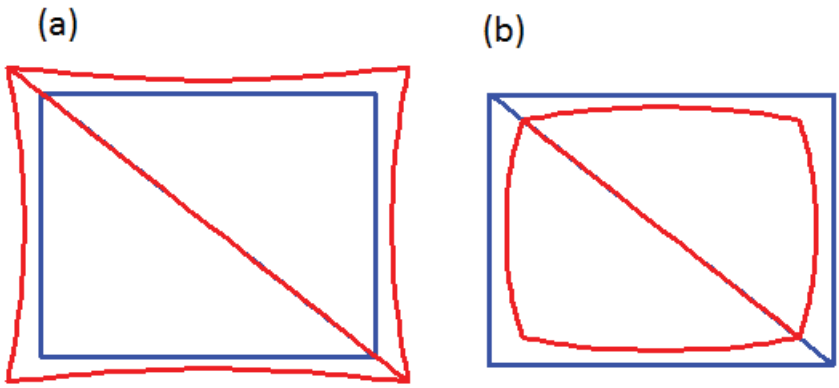

Figure 4.14 Effect of camera radial distortion k_1 (a) k_1 is positive (b) k_1 is negative.

Decentering distortion arises when the center of the lens element are not aligned collinear. It is modelled as

$$\begin{aligned} \Delta x &= 2p_1xy + p_2\left(r^2 + 2x^2\right) \\ \Delta y &= p_1\left(r^2 + 2y^2\right) + 2p_2xy \end{aligned} \tag{4.6}$$

where p_1, p_2 are coefficients of decentering distortion.

Thin prism distortion is due to the tilt of lens element or CCD sensor in the manufacturing or assembly of the camera. It can be expressed as

$$\begin{aligned} \Delta x &= s_1r^2 \\ \Delta y &= s_2r^2 \end{aligned} \tag{4.7}$$

where s_1, s_2 are coefficients of thin prism distortion.

Letting $q_1 = s_1 + p_2$ and $q_2 = s_2 + p_1$, Eq. (4.6) and (4.7) can be reorganized and combined as [36]

$$\Delta x = 2x(p_2 x + p_1 y) + q_1 r^2$$
$$\Delta y = 2y(p_2 x + p_1 y) + q_2 r^2 \tag{4.8}$$

The distortion effect in Eq.(4.8) is illustrated in Figure 4.15. The coefficient of p_1 and p_2 generate keystone effect, q_1 and q_2 cause "bowing" effect.

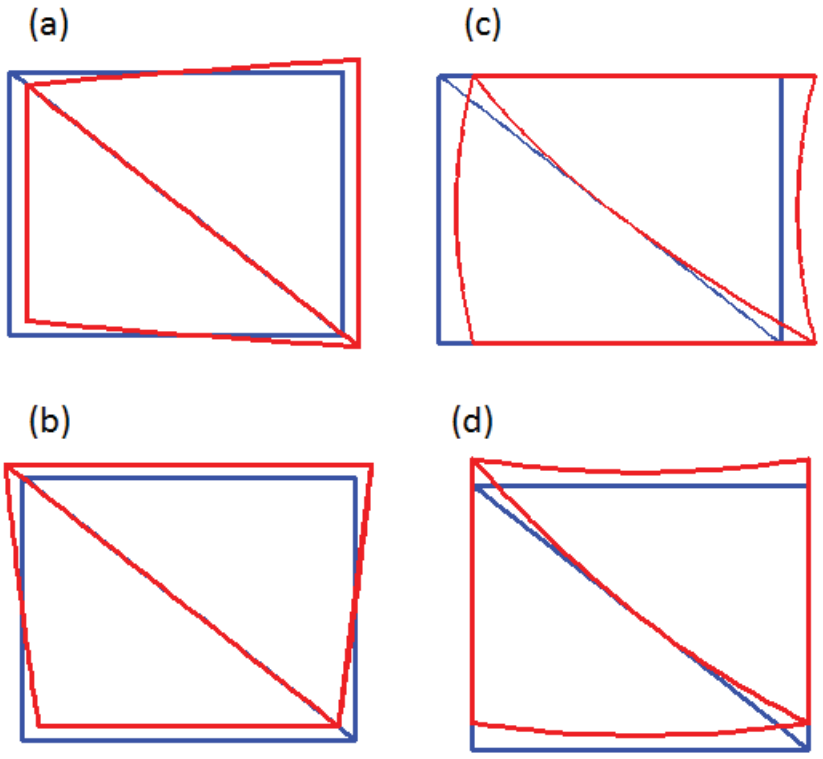

Figure 4.15 Effect of lens distortion. (a) and (b) show the effect of p_1 and p_2 , where $p_2 = 0$ in (a) and $p_1 = 0$ in (b). (c) and (d) show the effect of q_1 and q_2 , where $q_2 = 0$ in (c) and $q_1 = 0$ in (d).

Camera distortion causes image-height dependent nonlinear mapping error and needs to be corrected accurately. Usually the dominated camera distortion is first-order radial distortion, which corresponds to k_1 in Eq. (4.5). For the SCOTS test of DKIST M1, 0.04 % radial distortion (k_1) at the edge of the mirror (r = 2100

mm) would cause around 400 nm RMS measurement error, which are mainly astigmatism and coma. The Zernike coefficients of the error map are given in **Table 4.1**.

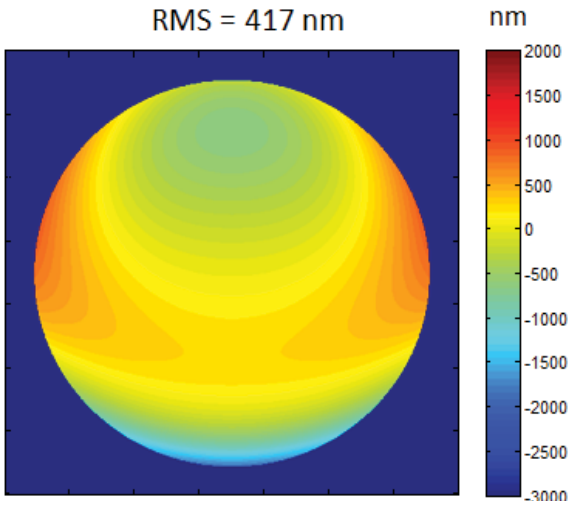

Figure 4.16 Simulated measurement error of DKIST M1 due to camera radial distortion ($k_1 = 0.04\%$)(parent vertex is defined in positive y direction)

Table 4.1. Zernike coefficient for 0.04% radial distortion (nm)

Z4 (power)	-44
Z5 (astigmatism)	1
Z6 (astigmatism)	336
Z7 (coma)	237
Z8 (coma)	0
Z9 (trefoil)	10
Z10 (trefoil)	0.5
Z11 (spherical)	-25

4.2.2 Perspective projection

Imaging through the camera, a three-dimensional object is transformed into a two-dimensional image on camera sensor. Such mapping is called perspective

projection. Perspective projection is a non-linear transformation. In this mapping, distance and angles of 3D object is not preserved, parallel lines do not generally project to parallel lines, scaling and foreshortening also occurs. An example showing the effect of foreshortening is given in Figure 4.17. A camera matrix including a rotation matrix and a translation vector, which is also known as "view matrix" is used to describe the perspective projection in computer vision. Camera perspective projection also needs to be taken care in SCOTS mapping process.

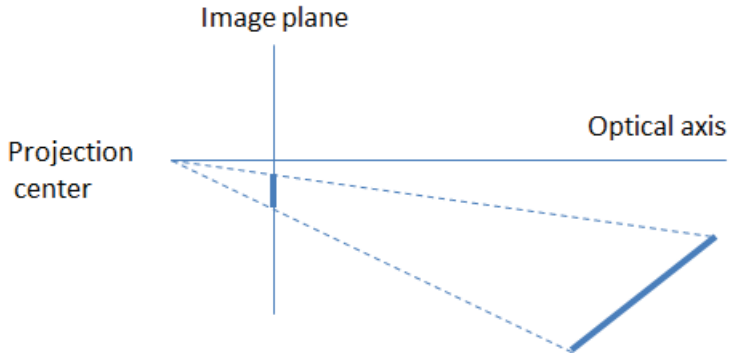

Figure 4.17 Effect of foreshortening. The dimension parallel to the optical axis is compressed relative to the frontal dimensional.

4.2.3 Mapping correction

In SCOTS tests, usually the mapping is corrected using fiducials on the test surfaces. Physical locations of the fiducials are measured with a laser tracker and the fiducial images are recorded by the SCOTS camera. We used a set of orthogonal vector polynomials [37,38] to fit the mapping between laser tracker

measured fiducial positions, which represent the local samplings on the test mirror, and the camera-captured fiducial positions. The diameter of each fiducial was chosen that each fiducial image can fill less than 10 pixels on the camera CCD to avoid distortion bias to be introduced into centroiding [39]. The overall mapping process can be described in 4 steps:

1. Obtain (x,y) coordinate of each fiducial from laser tracker measurement;
2. Obtain (x′,y′) coordinate of each fiducial from centroiding of fiducial images;
3. Fit mapping relation between (x′,y′) and (x,y) using the base function (vector polynomials) and get fitting coefficients.
4. Use fitted coefficients to map raw slope map from (x′,y′) coordinate to (x,y) coordinate and resample the map with even spacing .

(a)

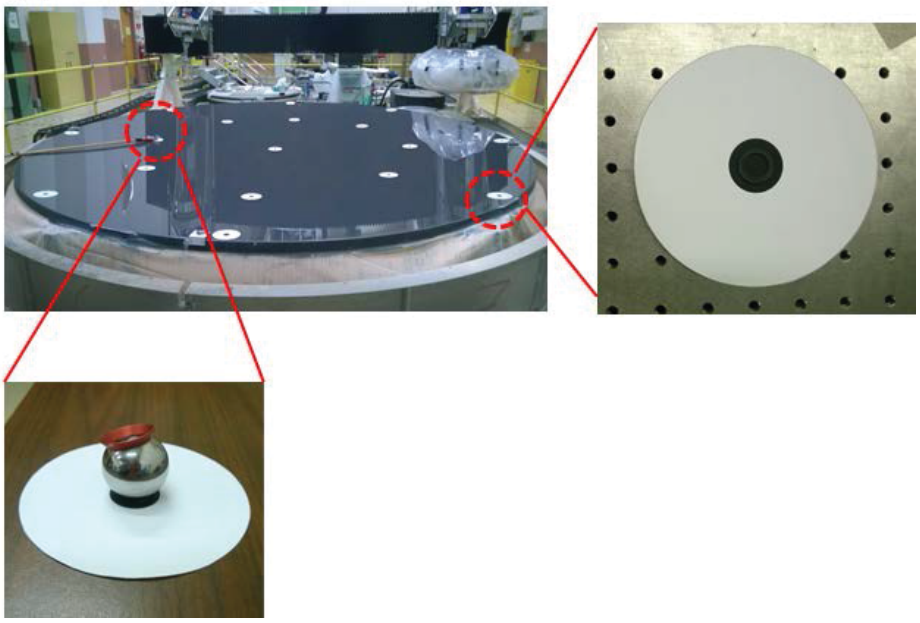

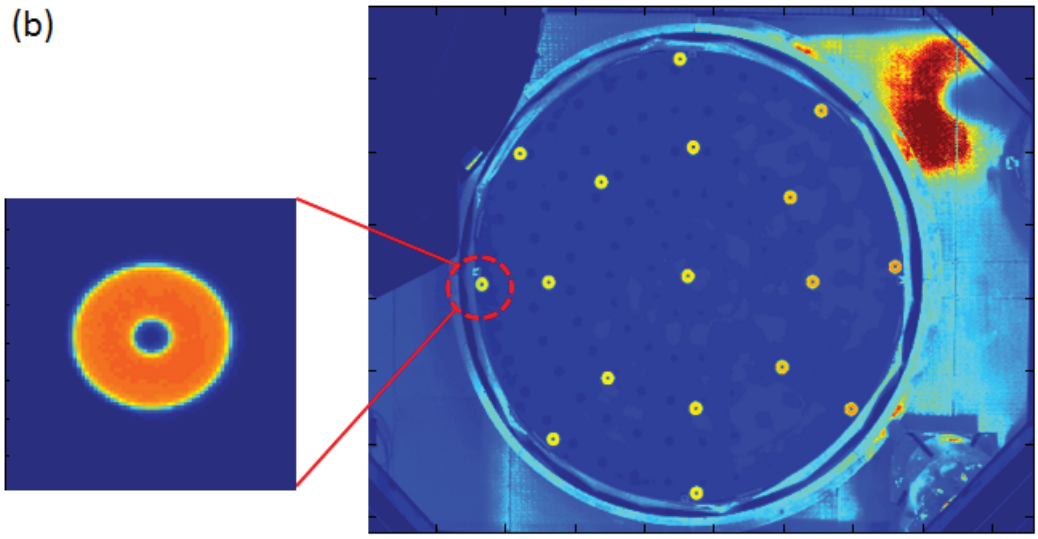

Figure 4.18 Example of fiducials used in testing DKIST M1 (a) fiducial targets on the mirror (b) fiducial image captured by SCOTS camera

For radial distortion k_1, S4 and S11 in vector polynomials can fully describe this nonlinear mapping. However, if lens decentering and tilt effect are presented, more polynomials are needed to fit the distortion mapping. For a small amount of keystone projection, using up-to S11 and T11 polynomial fitting can correct the residual mapping error to less than 0.1 pixel RMS. For most of metrology applications, the residual is small enough so that the induced error in the final surface map is negligible.

4.2.4 Calibration of mapping using camera 3D ray directions

Different from traditional camera distortion calibration in photogrammetry, the in-situ camera calibration method mentioned in Sec. 4.2.3 takes only one image and calibrates the camera distortion (intrinsic) and perspective (extrinsic) at the same time. It avoids the adverse effects from camera instability and uncertainty in the estimation of external parameters in the bundle adjustment algorithms commonly used in photogrammetry. However, the drawback is that camera intrinsic distortion and extrinsic perspective parameters are not separable in the fitting coefficients; and the calibration needs to be performed every time if the camera pointing or test geometry (mirror orientation, etc.) changes between the measurements. Sometimes, more than one mirror orientation is needed in the rotation measurements to average out systematic error; doing laser tracker measurement of the fiducials (for large telescope mirror like a 8.4 meter diameter segment of the GMT primary, more than 50 fiducials are needed) for mapping correction at each mirror orientation will be an extremely time consuming task. And sometimes, the test optics is too small or contact restricted, putting fiducials on these test optics is not applicable.

To solve the mapping correction in testing smaller optics and avoid repeated fiducials measurements for multiple mirror orientations, we measure the ray directions [40] of each camera pixel in 3D and use Zemax to trace the rays through the test system to find the intersection point on the test optics. Mapping

coefficients are then found by fitting the camera pixels and the intersection points on the mirror to correct mapping of raw slope maps.

This method has been implemented in the SCOTS metrology of DKIST M1 which needs multiple mirror rotation measurements and evaluating a transmission lens system [41]. The two tests used different control targets (active and passive) for measuring camera ray directions. Sec. 4.2.4.1 and Sec. 4.2.4.2 describe the methods of using the two kinds of targets, respectively; Sec. 4.2.4.3 discusses uncertainty in camera ray measurement; Sec. 4.2.4.4 gives a summary about measuring camera ray directions and suggestions of selecting targets in practical implementation.

4.2.4.1 Measuring camera ray directions using active target

To measure the ray direction of each camera pixel, 3D control targets are needed in space. The targets can be passive fiducials on the test optics or active self-illuminous structured light pattern such as LCD display. I have used both targets in ray direction measurements according to practical implementation and sensitivity requirement. Measuring the ray direction using pre-calibrated commercial LCD display (active target) was implemented in evaluating a transmission lens system [41] with system uncertainty analysis. In this section, I will describe the measurement procedure.

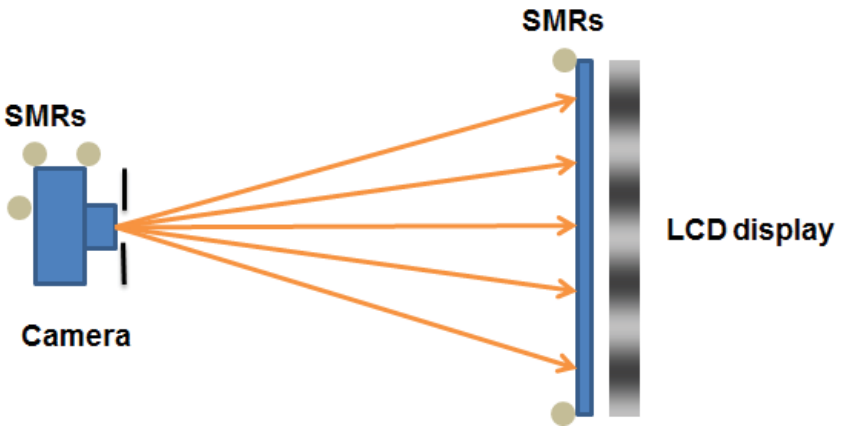

Figure 4.19. Layout of measuring ray direction of each camera pixel using LCD display

Before the measurement, positions of several display pixels and camera aperture were pre-calibrated and registered to several SMRs using the method described in Sec 3.1. After the pre-calibration, the LCD display was placed in front of the camera displaying intensity modulated sinusoidal fringes as illustrated in Figure 4.19. Camera captured the phase-shifted fringe images, and the corresponding display pixel of each camera pixel was calculated from the unwrapped phase map (φ_x, φ_y). By measuring the reference SMRs on the camera and display using laser tracker, camera aperture and display pixel position in the measurement setup can be obtained by coordinate transform of pre-calibration data. Under pinhole camera model, knowing camera aperture $(x_{\text{camera}}, y_{\text{camera}}, z_{\text{camera}})$ and each camera pixel associated display pixel position $(x_{\text{target}}, y_{\text{target}}, z_{\text{target}})$, the ray direction of each camera pixel (l,m,n) can then be

represented by a unit vector starting from the aperture of the camera to its associated display pixel position, as shown in Eq.(4.9).

$$\begin{bmatrix} l \\ m \\ n \end{bmatrix} = \frac{1}{\sqrt{\left(x_{\text{target}} - x_{\text{camera}}\right)^2 + \left(y_{\text{target}} - y_{\text{camera}}\right)^2 + \left(z_{\text{target}} - z_{\text{camera}}\right)^2}} \left(\begin{bmatrix} x_{\text{target}} \\ y_{\text{target}} \\ z_{\text{target}} \end{bmatrix} - \begin{bmatrix} x_{\text{camera}} \\ y_{\text{camera}} \\ z_{\text{camera}} \end{bmatrix} \right) \quad (4.9)$$

4.2.4.2 Measuring camera ray directions using passive target

For some of the tests, the camera ray direction can be measured in-situ using passive target (e.g. fiducials) on the test optics. Camera captures fiducials image and the fiducial positions are measured by a laser tracker. After projecting the measured SMRs position on to the mirror surface, the camera ray direction can be calculated using Eq.(4.9). Passive targets are usually used in measuring large astronomy telescope mirrors which requires a large field of view.

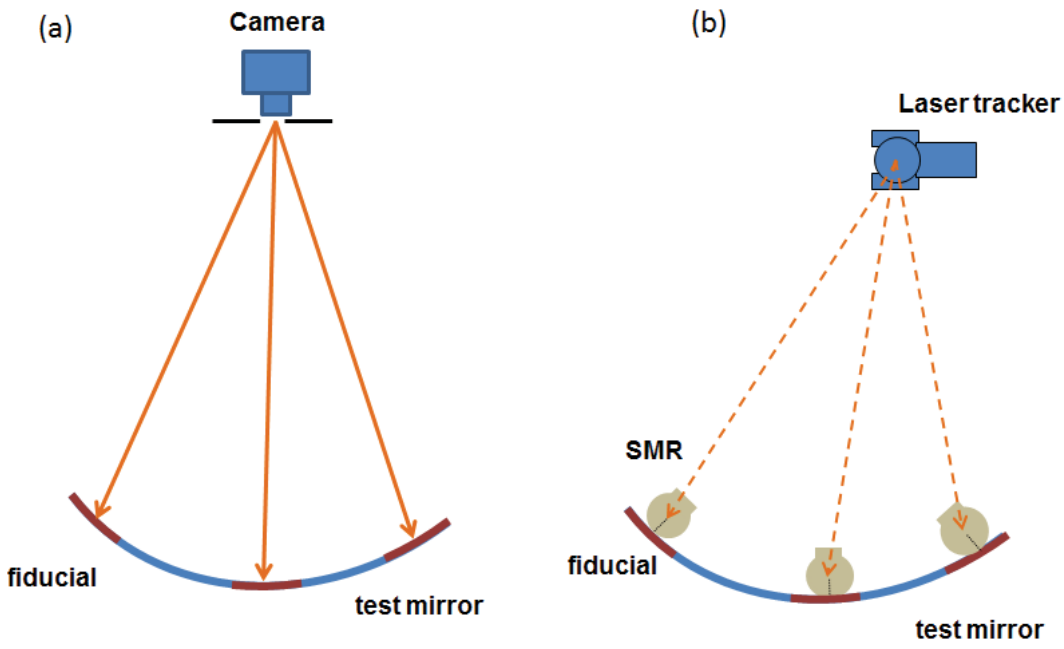

Figure 4.20 Layout of measuring camera ray direction using fiducial targets. (a) Camera takes the image of the fiducials and (b) laser tracker measures the physical locations of the fiducials.

4.2.4.3 Uncertainty in ray direction measurement

Using the above measurement procedure and camera ray model, the ray direction of each camera pixel is defined by two points which is the camera aperture and camera pixel associated target position; uncertainty or bias in measuring either of the two points would introduce error in the measured ray angle. For example, a bias in measuring camera aperture lateral position will tilt the entire camera ray bundle. When those tilted rays are traced through the test system, the intersection points on the test optics for mapping correction will be shifted, as shown in Figure 4.21 (a). Scaling error may occur when the pixel pitch of the LCD display used as active target for measuring camera ray directions is

not correctly calibrated. Those rays also give wrong intersection points on the test optics, as shown in Figure 4.21 (b).

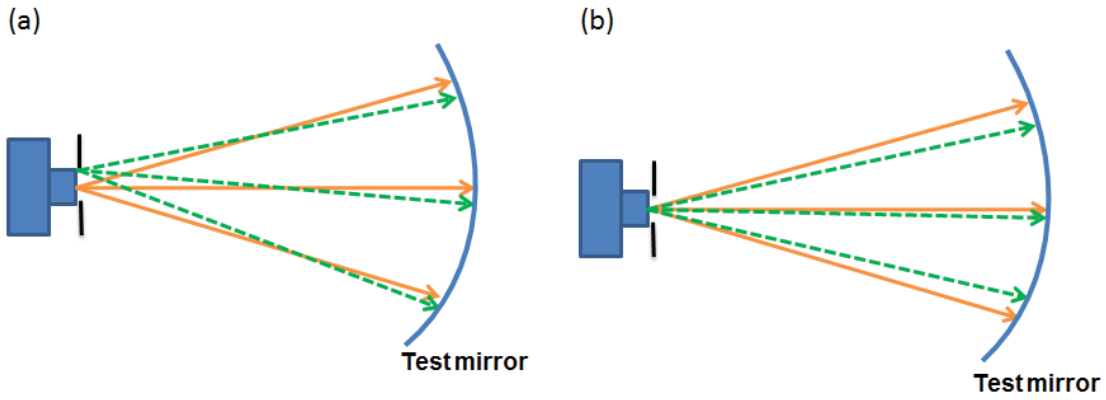

Figure 4.21. Biased ray direction (green dashed) causes error in calculating intersection points on the test mirror. (a) Shift of ray directions (b) Scaling error in ray directions

For SCOTS test of DKIST M1, ~10 μrad tilt of camera ray direction would cause ~0.2 mm systematic lateral shift of the intersection points on the mirror for mapping correction. For mapping error with 0.2 mm constant lateral shift in x ($\overrightarrow{\Delta \mathbf{r}} = 0.2\hat{i}$ mm) and y direction ($\overrightarrow{\Delta \mathbf{r}} = 0.2\,\hat{j}$ mm), the surface measurement errors are given in Figure 4.22 and Figure 4.23.

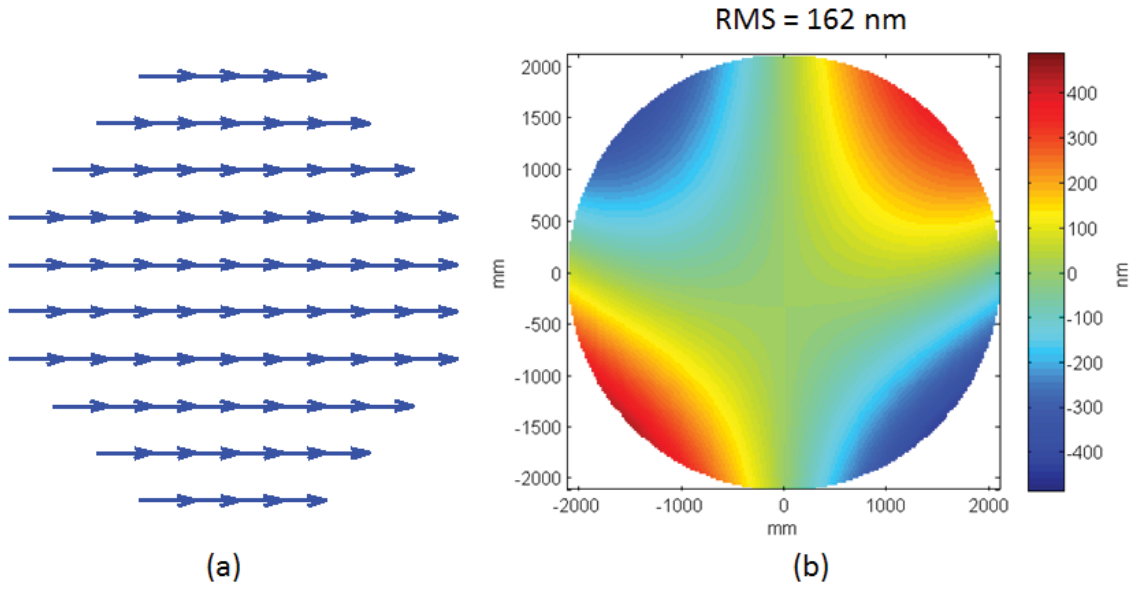

Figure 4.22 (a) Vector plot of mapping error $\overrightarrow{\Delta \mathbf{r}} = 0.2\hat{i}$ mm (b) Surface measurement error of DKIST M1 (parent vertex is defined in positive y direction).

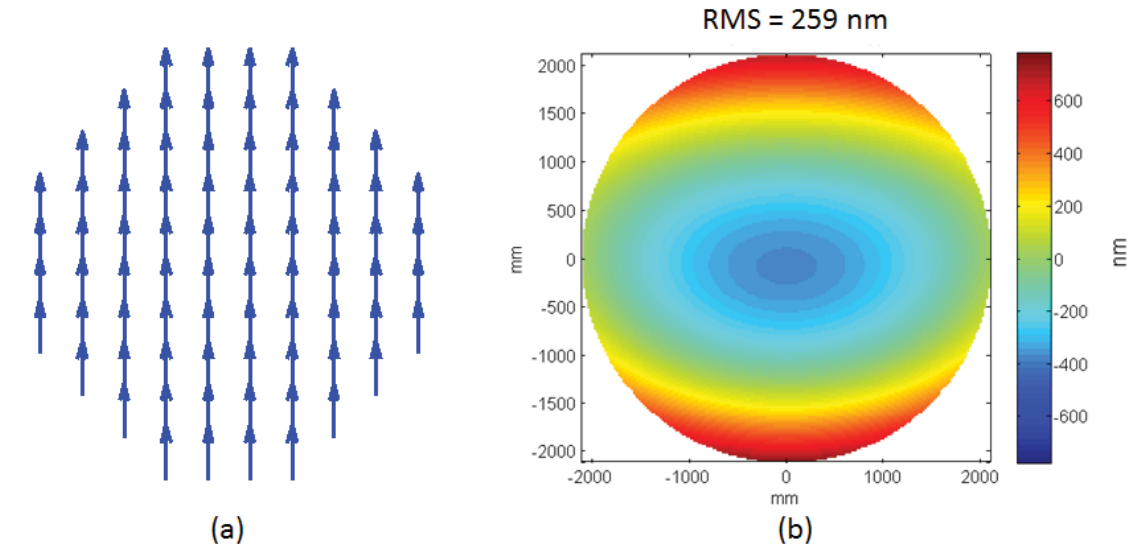

Figure 4.23 (a) Vector plot of mapping error $\overrightarrow{\Delta \mathbf{r}} = 0.2\hat{j}$ mm (b) Surface measurement error of DKIST M1 (parent vertex is defined in positive y direction).

Table 4.2. Zernike coefficient (nm) for 0.2 mm shift in mapping

	$\overrightarrow{\Delta \mathbf{r}} = 0.2\hat{i}$	$\overrightarrow{\Delta \mathbf{r}} = 0.2\hat{j}$
Z4 (power)	0	215
Z5 (astigmatism)	160	0
Z6 (astigmatism)	0	-145
Z7 (coma)	0	-15
Z8 (coma)	-22	0
Z9 (trefoil)	0	-3
Z10 (trefoil)	-3	0
Z11 (spherical)	0	0

4.2.4.4 Summary of ray directions measurement

In the calculation of finding intersection points on the mirror for mapping correction using calibrated camera ray directions, the ray-tracing starts from camera aperture, and a ray is traced through the system following its direction until it hits the test optics. Since the measured camera ray directions are unit vectors, if there is an error in the measured camera ray directions, the longer the distance a ray needs to travel before hitting the test optics, the larger the error it would be in the traced intersection point on the test optics. Error in the intersection points lead to incorrect mapping relation which will propagate to the final surface map. Figure 4.24 shows the distance sensitivity of using camera rays to correct mapping in SCOTS tests.

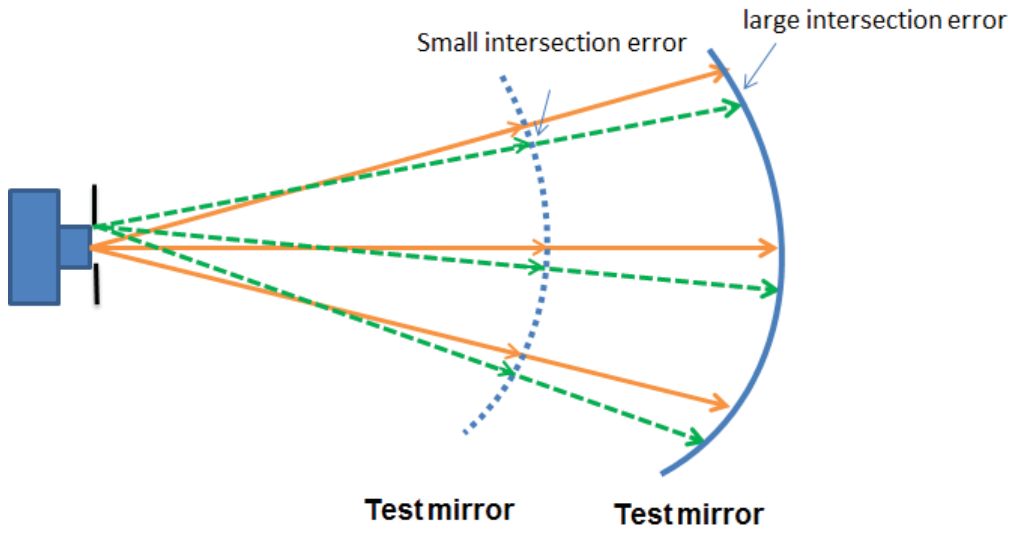

Figure 4.24 Biased ray direction (green dashed) generates larger error in finding the intersection points on the test mirror for mapping correction when the testing distance gets longer.

Therefore, a large distance separation between the camera and the control target is recommended in practical measurement to minimize position measurement uncertainty introduced error in determining ray direction of each camera pixel.

For the selection of target type (passive or active) in camera ray direction calibration, it really depends on sensitivity, accuracy requirement, practical implementation, and etc. Passive pattern gives less mapping resolution (the measured camera ray directions are limited by the number of targets that used). Interpolation or extrapolation is also needed if denser camera pixel ray directions are desired. A uniform illumination is required if centroiding is used to detect target positions in the image. Passive targets are usually used when a large

camera field of view (such as 4.2 meter diameter DKIST M1) needs to be covered. On the other hand, active self-illuminous structured light pattern such as gray code pattern and scanning lines generated by LCD display give higher measurement resolution. It can measure the ray angle of every camera pixel and thus provide a dense sampling in mapping correction. Phase-shifted sinusoidal pattern can provide even better signal to noise ratio to be much more time efficient. However, a stitching processing might be required if you want to have a large measurement distance to maintain low measurement uncertainty but do not have a large enough LCD display.

4.2.5 Effect of camera lens aberration

The image quality of the camera lens plays an important role in the measurement. Aberrations in camera lens degrade the fringe images and affect the phase retrieval in the data processing. Image simulation tool in optical design software is capable of simulating some of the aberration effects. However, it runs into problem when a large camera field of view is required which needs a dense sampling of field dependent point spread function (PSF) to get accurate simulation results. A Matlab [42] simulation tool has been developed to study the camera lens aberration effect in SCOTS test. The program is optimized in computational speed to be able to simulate a large camera field of view without scarifying accuracy.

The imaging system (camera) in SCOTS is an incoherent imaging system. For a diffraction limited incoherent imaging system [43,44],

$$I_i(\hat{u},\hat{v}) = \left|h(u,v)\right|^2 \otimes I_g(\hat{u},\hat{v}) \tag{4.10}$$

$$\left|h(u,v)\right|^2 = \left|\Im^{-1}\{H(f_u, f_v)\}\right|^2 \tag{4.11}$$

$$H(f_u, f_v) = P(-\lambda z_{xp} f_u, -\lambda z_{xp} f_v) \tag{4.12}$$

$I_g(\hat{u},\hat{v})$ is the ideal geometric irradiance image; $\otimes$ denotes convolution; $\left|h(u,v)\right|^2$ is point spread function (PSF); $H(f_u, f_v)$ is known as the optical transfer function (OTF); and $P(-\lambda z_{xp} f_u, -\lambda z_{xp} f_v)$ is the pupil function.

For a diffraction-limited incoherent imaging system, the pupil function is defined by the shape of the pupil. For a circular pupil, the pupil function is

$$P(x,y) = circ\left(\frac{\sqrt{x^2+y^2}}{r_{xp}}\right) \tag{4.13}$$

When aberration is taken into account, an additional phase term is then added to the pupil function, and the pupil function is written as

$$P(\hat{u}_o,\hat{v}_o;x,y) = circ\left(\frac{\sqrt{x^2+y^2}}{r_{xp}}\right)\exp\left(-jkW\left(\hat{u}_o,\hat{v}_o;\frac{x}{r_{xp}},\frac{y}{r_{xp}}\right)\right) \tag{4.14}$$

W denotes the wavefront aberration which is typically described in terms of Seidel sums or Zernike expansion.

Comparing Eq. (4.13) and Eq. (4.14), the pupil function of aberrated imaging system is dependent on the imaging position coordinate $(\hat{u}_o, \hat{v}_o)$, which means the system is space variant and PSF for every position in the image is required to get its aberrated image. Space-variant incoherent imaging cannot be described by a single convolution in Eq. (4.10). Instead, superposition integral is needed (Eq.(4.15)) to get aberrated images.

$$I_i(\hat{u}_o, \hat{v}_o) = \iint_{\infty} I_g(u, v) \left| h(\hat{u}_o, \hat{v}_o; u, v) \right|^2 du dv \tag{4.15}$$

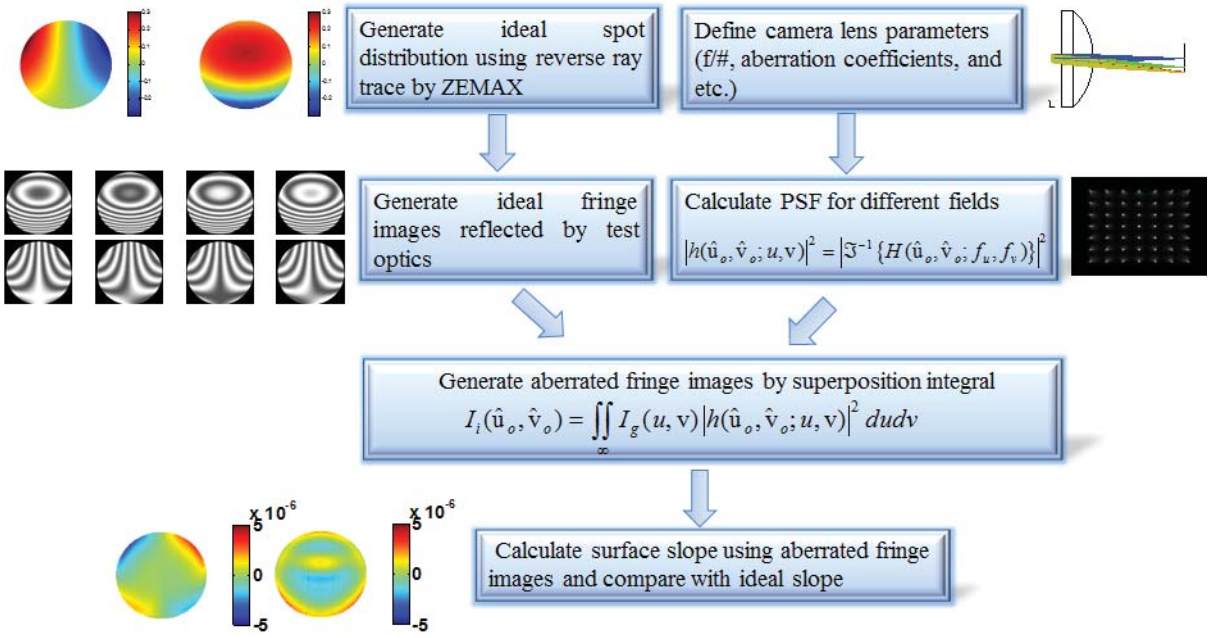

Figure 4.25. Simulation flowchart of camera aberration effect in SCOTS measurement

Figure 4.25. gives the flowchart of the simulation process:

1. Generate ideal spot distribution on the display using Zeamx ray tracing.

2. Generate camera captured ideal phase shifted fringe images ($I_g(u,\mathrm{v})$) from the ideal spot distribution got from step 1.
3. Define camera parameters, such as f/#, aberration coefficients (which can be from a real lens model), calculate PSF ($\left|h(\hat{\mathrm{u}}_o,\hat{\mathrm{v}}_o;u,\mathrm{v})\right|^2$) for different fields.
4. Generate aberrated fringe images using Eq.(4.15)
5. Calculate spot distribution on the display from aberrated fringe images and compare with ideal spot distribution generated in step 1.
6. Convert the difference of spot distribution in step 5 to slope difference.
7. Integrate the slope difference to get surface error.

4.2.5.1 Simulation case study

Two test cases were evaluated using the developed simulation tool. One was a spherical mirror SCOTS test, the other one was an off-axis ellipsoid mirror SCOTS test. Three major camera aberrations coma (W_{131}), astigmatism (W_{222}) and spherical (W_{040}) were investigated in the simulation.

Case 1: Spherical mirror. **Table 4.3** gives the simulation parameters. The radius of curvature of the mirror was the same as the parent radius of curvature of the fast-steering secondary mirror (FSM) of Giant Magellan Telescope (GMT). The distance between mirror and camera was set equal to the distance between mirror and display, which was 4400 mm.

Table 4.3. Simulation parameters of a spherical mirror

Mirror diameter	435.6 mm
Radius of curvature	4166.747 mm
Distance from mirror to display	4400 mm
Camera f/#	10
Camera field of view	6^0

Figure 4.26 is the plot of simulated slope errors (RMS) due to the camera aberrations. The aberration coefficients are normalized Seidel coefficients. From the figure, we notice that test is much more sensitive to coma, the odd aberration, than astigmatism and spherical. This is because the point spread function of coma is non-symmetric and thus biases the ideal fringe images heavily and non-uniformly in radial direction. For W_{222} and W_{040}, slope errors introduced by these two even camera lens aberrations are at sub-μrad level, which is usually the noise level of the test.

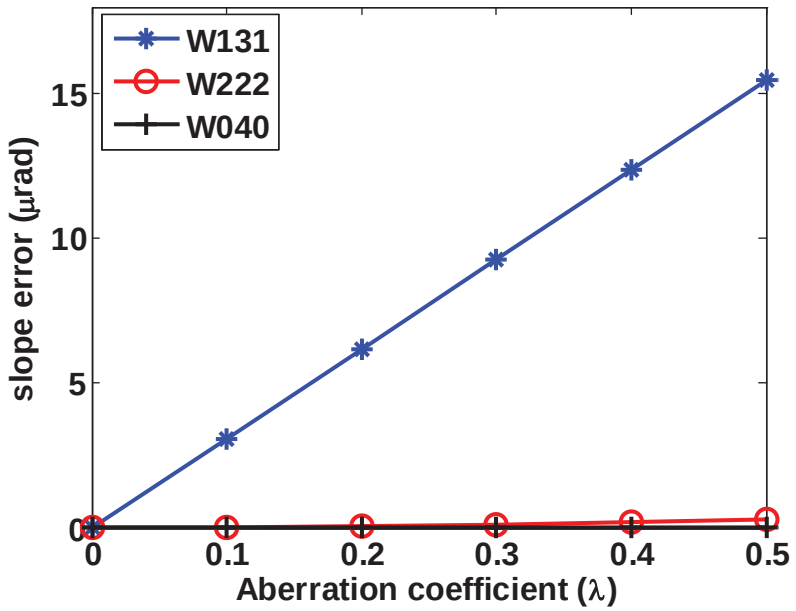

Figure 4.26. Simulated slope errors of testing spherical mirror due to camera aberrations.

Once we integrated the slope error caused by coma in camera lens (blue line in Figure 4.26), the shape of the surface error was mainly in Zernike power. Figure 4.27 is the plot of integrated surface error (RMS value) as a function of W_{131}. As shown in Figure 4.27, error increased linearly as coma (W_{131}) in camera lens increased.

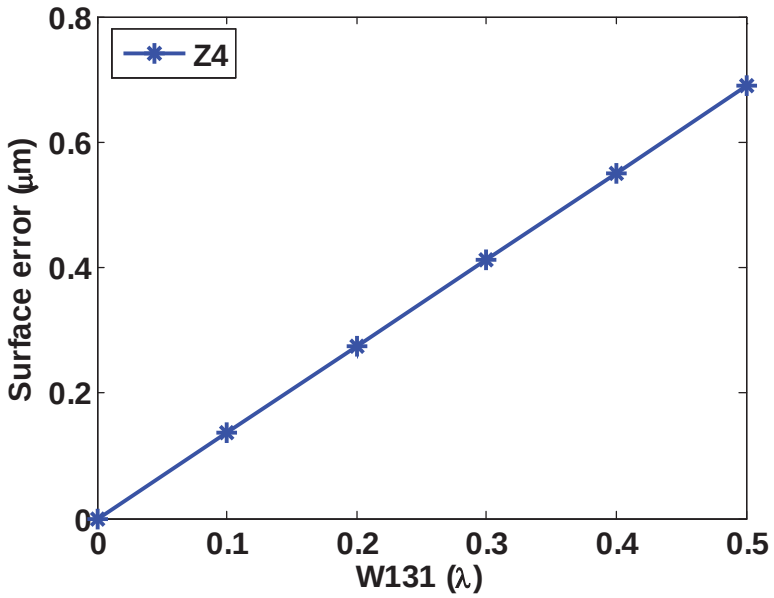

Figure 4.27. Surface error of testing spherical mirror due to coma (W_{131}) in camera lens

Case 2: off-axis ellipsoid mirror. **Table 4.4** gives the simulation parameters. The mirror parameters were the same as the off-axis segment of the FSMP of GMT but the mirror size (diameter) is only 40% of the actual segment.

Table 4.4. Simulation parameters of an off-axis ellipsoid mirror

Mirror diameter	435.6 mm
Radius of curvature	4166.747 mm
Conic constant	-0.7154
Off-axis distance	1088.92 mm
Distance from mirror to display	4400 mm
Camera f/#	10
Camera field of view	6^0

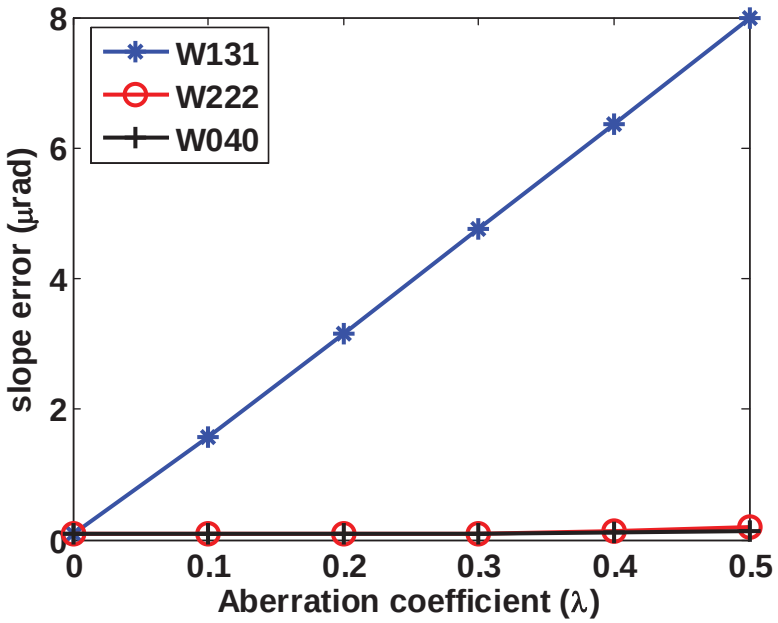

Figure 4.28. Simulated slope errors of testing off-axis ellipsoid mirror due to camera aberrations

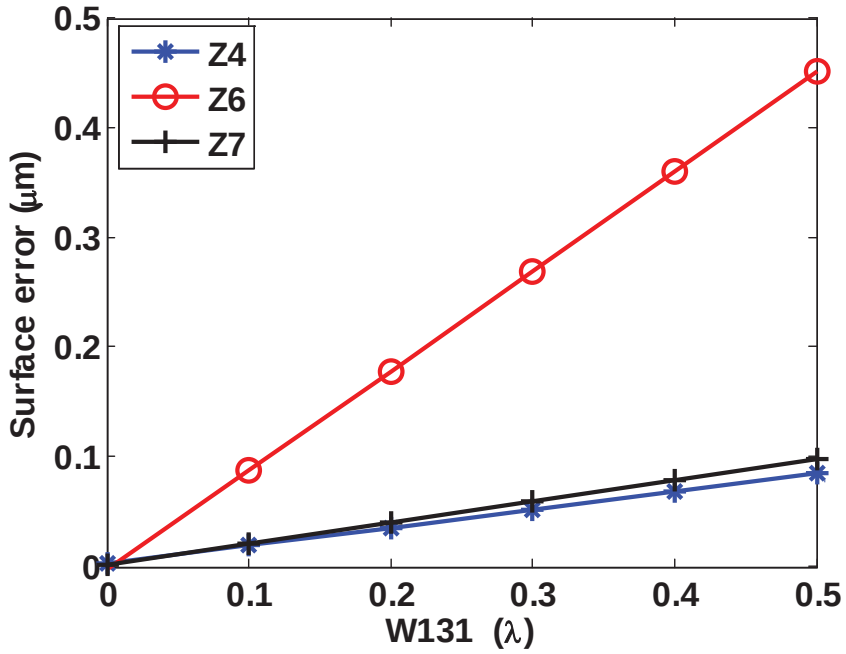

Figure 4.29. Surface error of testing off-axis ellipsoid mirror due to coma (W_{131}) in camera lens

Figure 4.28 and Figure 4.29 summarize the simulation results. Coma in camera lens was still the main error source. The natural surface property of this off-axis ellipsoid mirror made the error in surface shape not limited to Zernike power (Z4), but also astigmatism (Z6) and coma (Z7).

The above simulations assumed mapping-error-free fringe images. However, camera lens aberration can also introduces bias in camera ray direction measurement and fiducial centroiding process which can cause error in distortion mapping process. Therefore, in practical measurement, camera aberration effect might be more complicated since the induced measurement

errors can come from the combination effect of biased raw phase map and biased mapping correction.

Unfortunately, aberration-free image is generally not recoverable from degraded image through image post-processing. Therefore, to avoid aberration effect, the SCOTS camera lens should be designed with diffraction-limited performance, whose modulation transfer function (MTF) limits the system instrument transfer function (ITF) [45].

4.2.6 Example of camera lens designed for DKIST M1 SCOTS

Figure 4.30 is the camera lens designed for SCOTS test of DKIST M1. It is a single doublet with a physical stop in front of the lens. Besides owning the advantage of physically measurable aperture position, this landscape lens design also help to eliminate pupil aberration [46] in the imaging system. Based on the field of view of the test ($\pm 7^0$) and CCD format (2/3″), the focal length of the imaging lens is selected as 22.5 mm from commercial available off the shelf lens. The diameter of the stop is chosen as 2 mm so that the system can still have 70% modulation at 0.043cyc/mm on the test mirror. The lens also has diffraction-limited performance over 110% of required FOV (2 meter) as shown in Figure 4.31 and Figure 4.32.

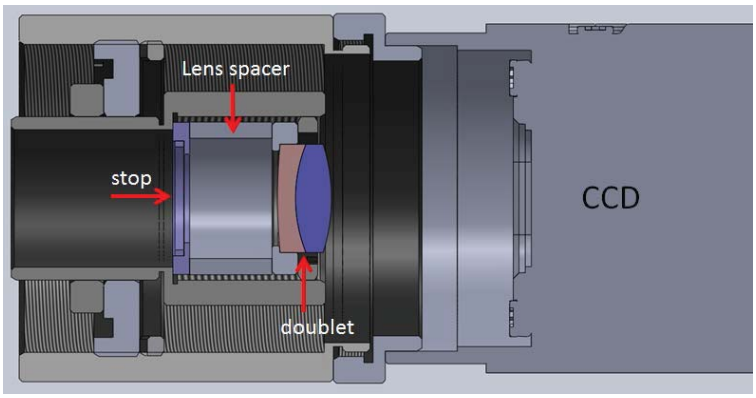

Figure 4.30. Landscape camera lens designed for DKIST M1 SCOTS

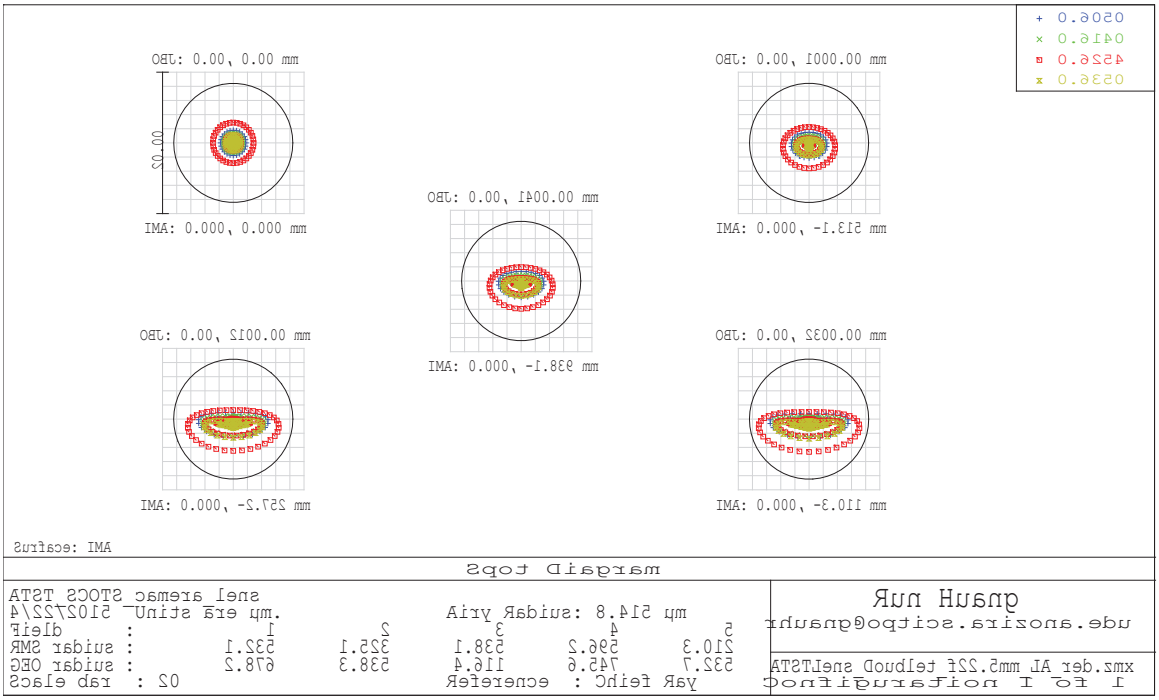

Figure 4.31. Spot diagram of the camera lens designed for DKIST M1 SCOTS

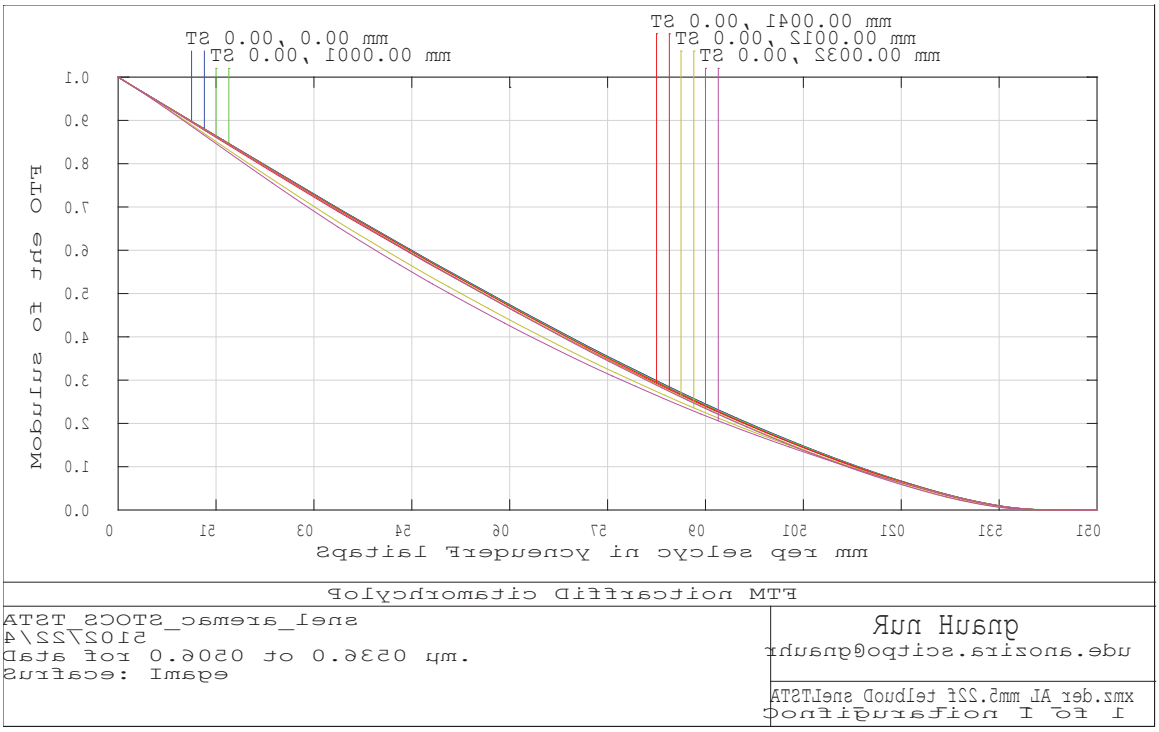

Figure 4.32. MTF of the camera lens designed for DKIST M1 SCOTS

4.3 Measurement of DKIST M1

Many sections of this chapter have already mentioned the SCOTS test of DKIST M1, either using it as an example for describing calibration setup and procedures or for discussion of calibration uncertainty, which is being fabricated at the time of writing this dissertation in the optical shop in University of Arizona. In this section, I give a summary of the SCOTS system and show some test results by carefully applying calibrations mentioned in this chapter. During the writing of this dissertation, the SCOTS system is being used as the primary metrology tool to provide feedback of the polishing process while interferometry test is being prepared.

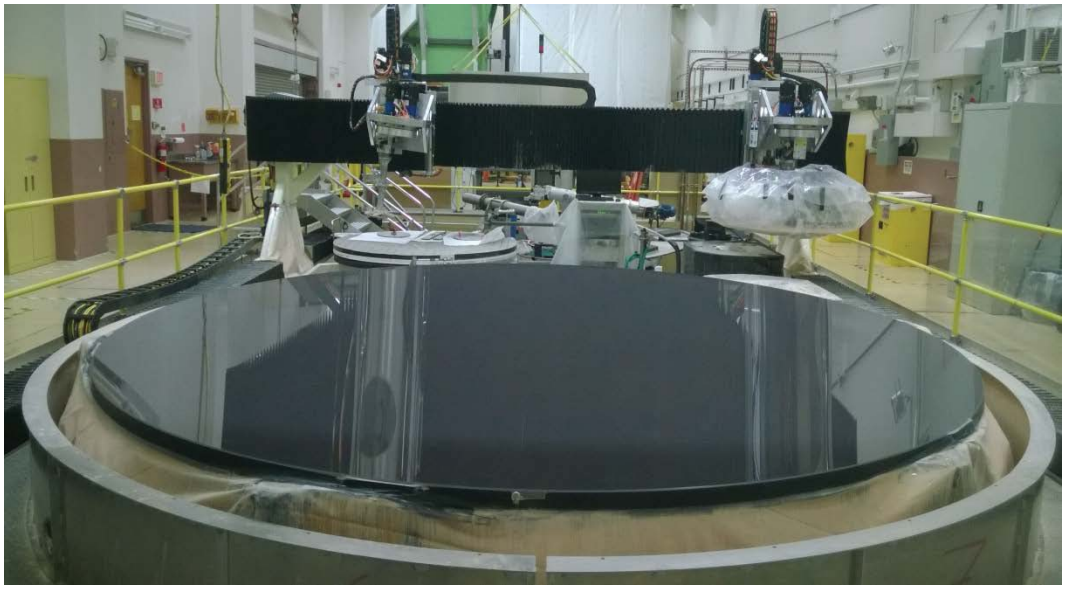

Figure 4.33. A photograph of the primary mirror of DKIST in Optical Shop in U of A. The primary mirror of DKIST is an off-axis parabola whose parent sphere has a radius of curvature of 16 meter. The mirror is 4.2 meter in diameter with more than 9 mm peak-to-valley aspheric departure.

4.3.1 Test geometry and system configuration

The test distance between SCOTS system and the mirror was 17.1 meter. Having the capability of 360 degree rotation of the polishing table, a rotation test of the mirror was designed. Measurements at different mirror orientations were averaged to help to reduce non-radial symmetric systematic error. The surface normal of local mirror center was tilted 0.2 degree about y direction (parent vertex is pointing to -x direction) to compensate lateral shift of the illumination area on the display for different mirror orientations.

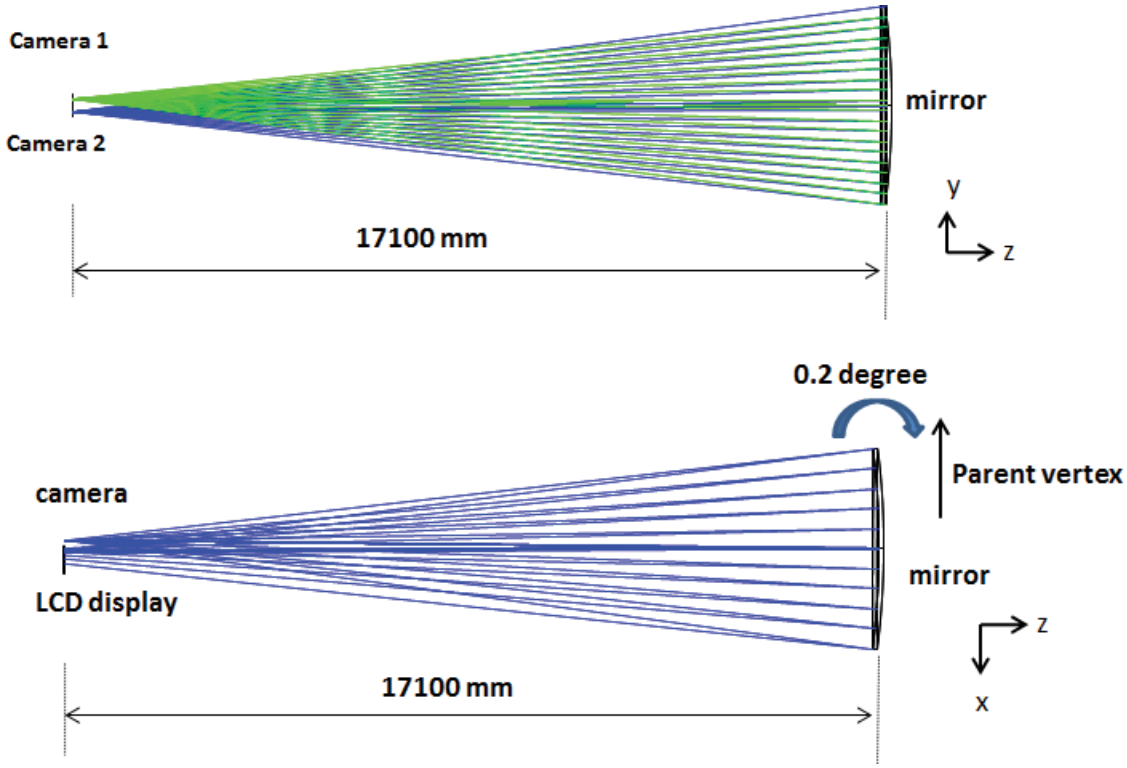

Figure 4.34. Geometrical layout of SCOTS test for DKIST M1

For a self-verification test, dual-camera setup was employed in the system. The two cameras were designed to be mounted at the same side of the display with ~100 mm lateral separation. By using two cameras, the system required slightly larger LCD display area as shown in Figure 4.35. A Dell 30" LCD with 400mm by 640mm illumination area was selected to meet the requirement. The specification of system components is listed in **Table 4.5**.

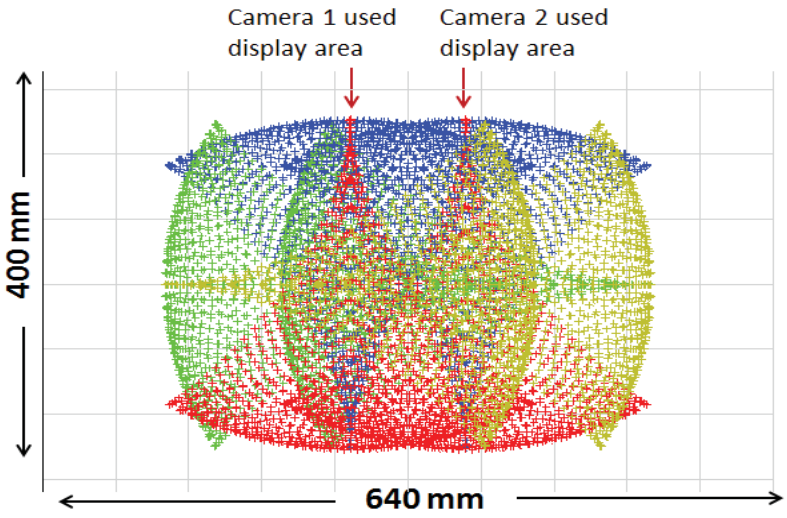

Figure 4.35. Simulated required display area for two cameras with 100mm lateral separation at mirror 0 degree, 90 degree, 180 degree and 270 degree orientations through Zemax ray tracing.

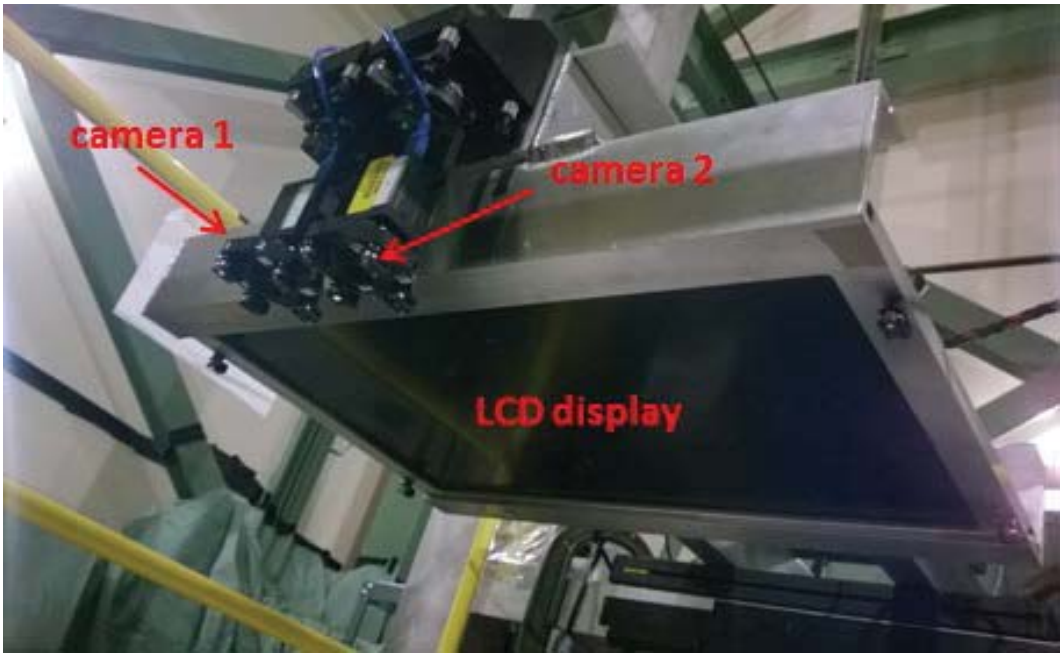

Figure 4.36. SCOTS on the test tower to measure DKIST M1

Table 4.5. Specification of SCOTS components for DKIST M1

	Brand	Specs
LCD Display	Dell U3014	Resolution:2560*1600 pixel pitch 0.2505 mm
CCD	Point Grey	GS3-U3-28S5M-C, resolution:1920*1440, pixel pitch: 4.54um
Camera lens	Edmund Optics	# 49939, diameter: 9 mm, focal length: 22.5 mm
Camera stop	National Aperture	2 mm round aperture, black 2 sides , mounted on 0.5 inch disk

4.3.2 Tolerance analysis

Measurement uncertainty includes 3 major error sources, which are test geometry, camera mapping and random noise. Test geometry refers to measurement uncertainty in determining camera aperture position, mirror tip/tilt, mirror clocking, screen tip/tilt and etc, which is usually limited by the accuracy of laser tracker. Mapping error might be generated due to the bias in determining fiducial position, which is discussed in detail in Sec.4.2.4.3. Random noise includes measurement noise due to system instability, mechanical vibration, air turbulence as well as noise in camera mapping correction.

System geometry tolerance was done by perturbing the test model in Zemax. Take 0.01 degree uncertainty of mirror clocking as an example. The mirror was rotated 0.01 degree in the Zemax model and ray tracing was performed to get the slopes. The result was then compared with the one where mirror was at its nominal position. The surface error map was obtained by integrating the slope difference.

Mapping tolerance was done by perturbing the measurement data. For example, for the tolerance of mapping decenter in y, the measured fiducial positions were shifted in y direction by 0.5 mm in data processing. The processed surface map was then compared with the original one which was processed without shifting of fiducial positions.

System repeatability was estimated using the method describe in Ref [47]. Total 50 measurements were taken and the estimated noise in a single measurement was about 80 nm RMS from Figure 4.37. This number will be reduced by a factor of $\sqrt{8}$ in the real test since 2 cameras, each with 4 mirror rotations (total 8 measurements) results are averaged to provide the final surface map.

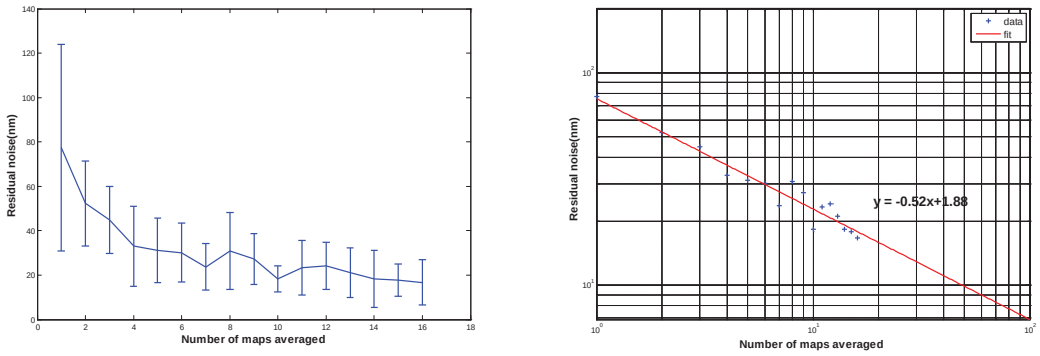

Figure 4.37 Random noise in SCOTS test of DKIST M1.

Random noise in camera mapping correction came from the centroid uncertainty of fiducial image, centration uncertainty of fiducial nest on the paper target. +/- 400μm uncertainty was budgeted in mapping correction. A Monte

Carlo simulation was performed to evaluate the random error in mapping correction. Errors with uniform distribution on an interval of -400 μm to 400 μm were added to the fiducial positions measured by the laser tracker. Figure 4.38 gives the averaged error map of 50 trials.

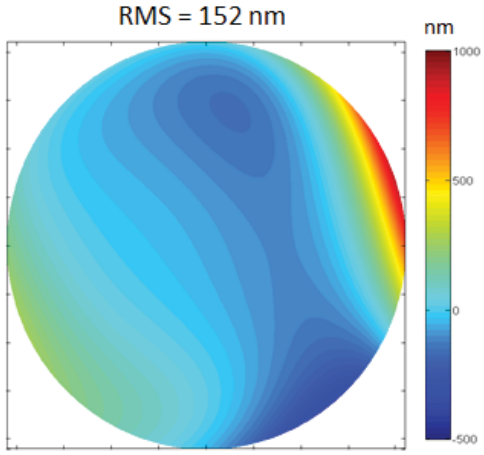

Figure 4.38 The averaged error due to random noise in mapping correction.

Table 4.6 provides a thorough tolerance analysis of DKIST M1 SCOTS test showing the predicted measurement uncertainty. (Parent vertex is defined in minus x direction)

Table 4.6. Tolerance for DKIST M1 SCOTS (nm)

	Camera y 0.2 mm	Camera x 0.2 mm	Camera z 0.2 mm	Mirror tilt y 0.006deg	Mirror tilt x 0.006deg	Mirror clocking 0.01 degree
Z4	1.4	3.2	218	18	19.2	0
Z5	5.2	1.4	0	13.2	50.4	551
Z6	1.4	5.2	0.2	48	15.6	0
Z7	0.6	0	0	0	12	78
Z8	0	0.6	0.2	10.8	0.6	0
Z9	1.2	0	0	0.36	12	11
Z10	0	1.2	0	10.8	0.6	0
Z11	0	0.4	0.2	6	0	0

Table 4.6. Tolerance for DKIST M1 SCOTS (nm) (continued)

	Screen tilt y 0.03deg	Screen tilt x 0.03deg	Screen z 0.2 mm	Screen clocking 0.02 degree	Mapping decenter y 0.5 mm	Mapping decenter x 0.5 mm
Z4	30.0	20.0	218	0.0	0.0	606.7
Z5	0.5	12.5	0	548.0	450.0	0.0
Z6	7.5	2.5	188	0.4	0.0	408.3
Z7	0.0	25.0	1	0.0	61.7	0.0
Z8	15.0	0.5	54	0.0	0.0	43.3
Z9	0.0	0.8	0	6.7	6.7	0.0
Z10	2.5	0.0	2.4	0.0	0.0	6.7
Z11	7.5	0.0	0.8	0.0	0.0	0.0

Table 4.6. Tolerance for DKIST M1 SCOTS (nm) (continued)

	Mapping scaling 99.98%	Noise in mapping	Random with 8 average	RSS
Z4	4	64.9	13.9	685.2
Z5	0.6	80.9	5.2	903.3
Z6	302	68.7	11.3	548.4
Z7	0	35.6	3.1	109.2
Z8	172	33.9	4.8	189.4
Z9	0	40.6	3.4	44.9
Z10	8	36.5	3.6	39.8
Z11	18	23.1	1.5	30.9

4.3.3 Measurement results

4.3.3.1 Measurement at different mirror orientations

Averaging measurements at different mirror orientations helped to greatly reduce non-radial-symmetric systematic errors. In the test of DKIST M1, SCOTS measured the mirror at 4 different orientations, where the mirror was rotated 90 degree between each orientation. Figure 4.39 shows measurement results of one of the two cameras at 4 mirror orientations. The averaged map at 4 mirror

orientations was calculated ($\overline{W}$). The fluctuation was calculated by comparing the difference between measurement at each mirror orientation and the averaged map $\Delta W = W_i - \overline{W}$. The fluctuation ΔW of the low-order terms including power, astigmatism and coma between different mirror orientations is plotted in Figure 4.40; and they were all within the tolerance analysis.

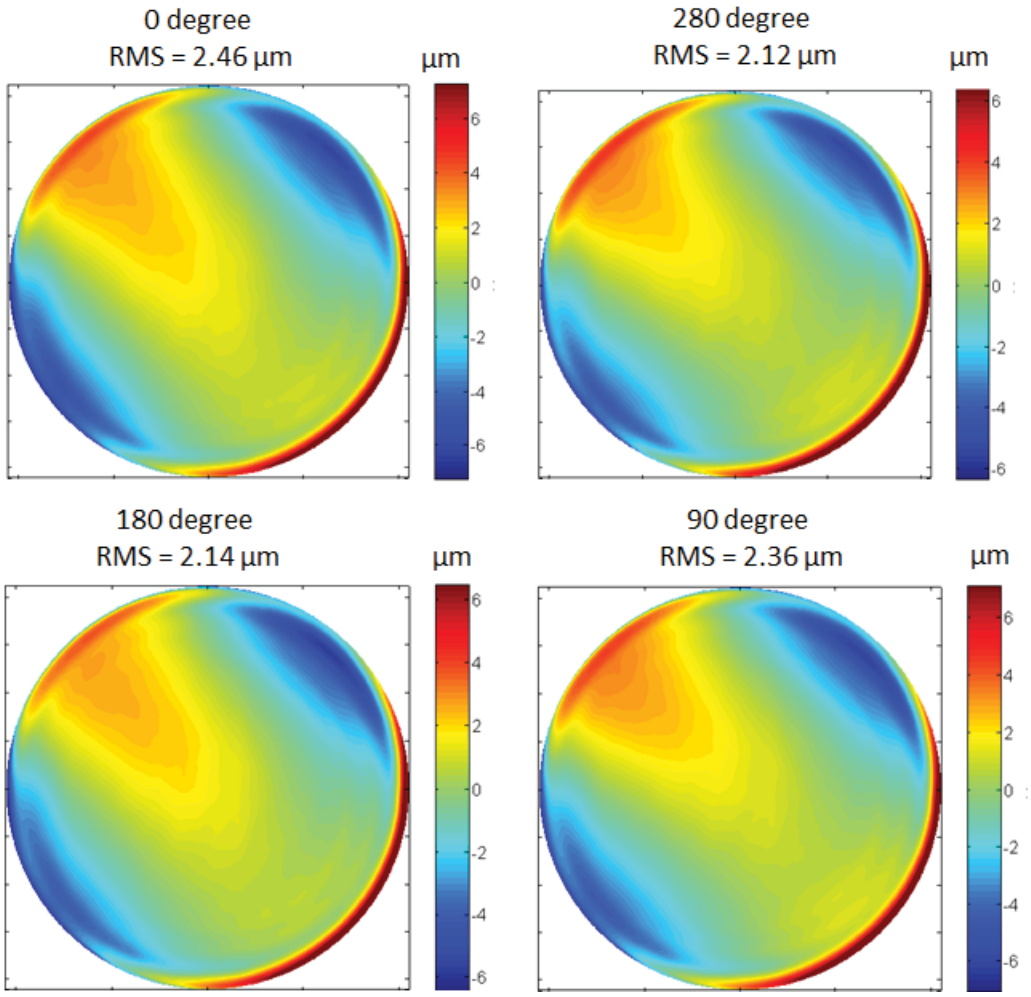

Figure 4.39 Camera #1 measured surface map of DKIST M1 at 4 different mirror orientations.

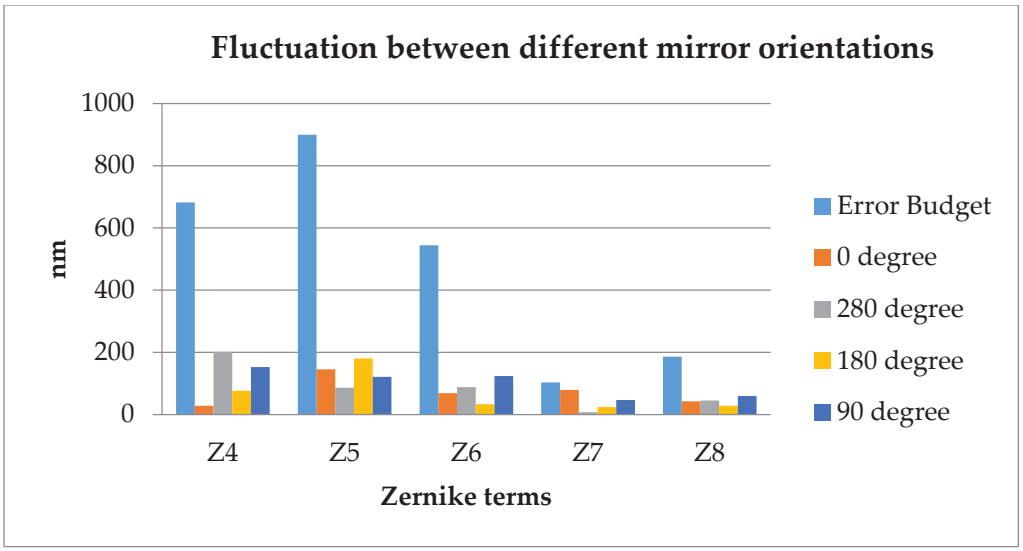

Figure 4.40. Fluctuation between measurements at different mirror orientations

4.3.3.2 *Comparison of the two camera results*

The two cameras in SCOTS system can provide a self-verification and the comparison of the two camera results is given in Figure 4.41. The result of each camera was the averaged map at 4 mirror orientations. The difference between two cameras was shown in Figure 4.41 (c). **Table 4.7** lists the Zernike coefficients of the difference map. The major difference between the two cameras was Z4.

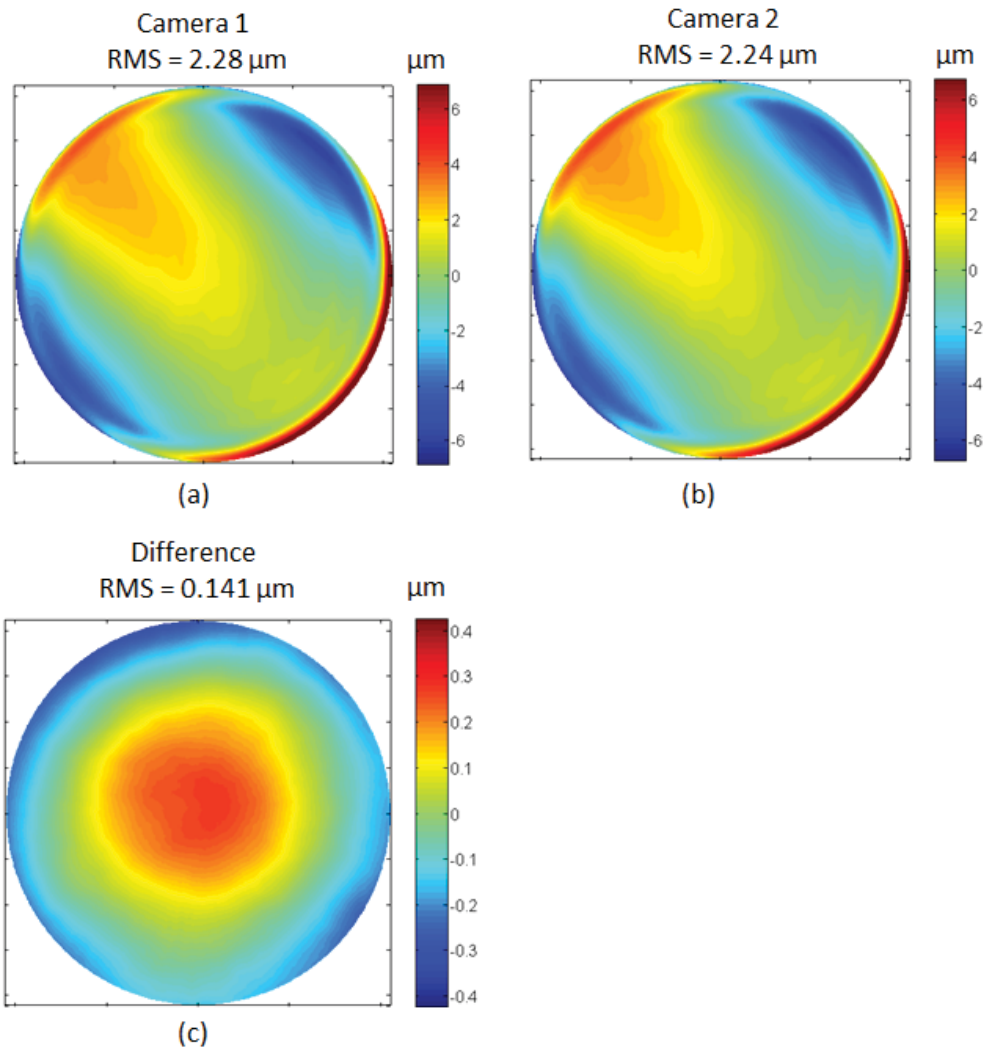

Figure 4.41. (a) Surface map of DKIST M1 measured by camera1 (b) Surface map of DKIST M1 measured by camera2 (c) difference map between camera 1 and camera 2.

Table 4.7. Zernike coefficient of the difference map in Figure 4.41(c) (nm)

Z4 (power)	-139
Z5 (astigmatism)	-14
Z6 (astigmatism)	0
Z7 (coma)	4
Z8 (coma)	17
Z9 (trefoil)	5
Z10 (trefoil)	8
Z11 (spherical)	13

The two cameras shared the same mirror geometry (tip, tilt, and rotation) and screen geometry (orientation and position), therefore, the measurement uncertainty between two cameras were mainly from the uncertainty of camera z position and mapping correction. For the result shown in Figure 4.41, after looking into the tolerance table in **Table 4.6**, the difference between the two cameras which was mainly in Zernike power term was most likely due to the camera z position uncertainty, the amount of which was about 0.13 mm. This 0.13 mm uncertainty was within the geometry tolerance analysis in **Table 4.6**.

4.3.3.3 Feedback on fabrication

While interferometry test was being prepared, SCOTS was being used as the principle metrology tool to guide the fabrication process. It played a critical role in the whole project and worked very well. Figure 4.42 (a) is SCOTS measured removal map before and after one polishing run, Figure 4.42 (b) shows predicted removal map when designing that polishing run. The difference between measured and predicted removal map is given in (c). In this polishing run, it mainly targeted on knocking down the edge which was always a hard part in both fabrication and metrology. Interferometry usually cannot measure such a steep slope change due to its limited dynamic range. However, SCOTS overcame this limit and successfully measured it, as shown in Figure 4.42 (a). This can provide very important information for the mirror edge quality. The difference

map in Figure 4.42 (c) which is around 100nm RMS is mainly low-order shape uncertainty. This is a combination uncertainty from polishing and metrology.

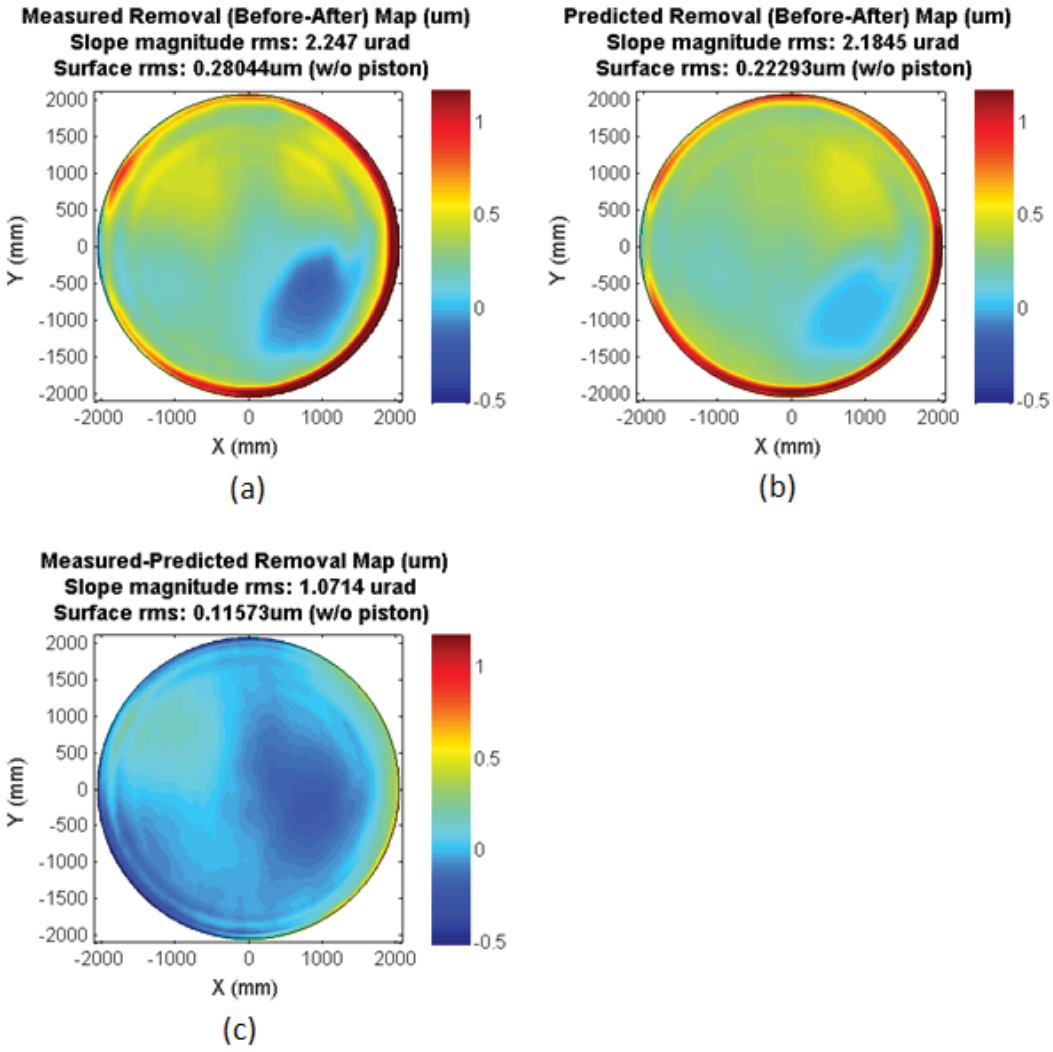

Figure 4.42. (a) SCOTS measured surface removal in one polishing run (b) Predicted surface removal in one polishing run. (c) Difference between measured and predicted.

5 ADVANCED SYSTEM CALIBRATION USING REFERENCE SURFACE

Chapter 4 shows that many systematic errors of SCOTS are a function of camera's field of view, perspective, screen pixel distortion and test geometry. Besides performing the calibration of each individual component as described in Chapter 4, test accuracy can also benefit from a calibration by measuring a high quality reference surface with similar radius of curvature of the test optics. After the measurement of test optics, the test optics is removed and a reference is precisely aligned at the same position as test optics and measured with SCOTS. Systematic errors can be eliminated by subtracting the measured reference map from the map of the test optics. Reference calibration was proved experimentally in the metrology of two X-ray mirrors [19,48].

5.1 Reduced sensitivity on geometry alignment

A great improvement of reference calibration is that it helps to reduce test sensitivity on geometry. In Sec. 3.2, we have already derived a series of parametric expressions of test sensitivity on geometry. In this section, we continue to use those parametric expressions to show the fundamentals of the

improved sensitivity by using reference calibration. Improved sensitivities on camera lateral position h and display tilt θ are given as two examples below.

Since astigmatism and coma are two major field-dependent (camera lateral position h) aberrations, reference calibration would mainly improve the sensitivity of these two aberrations to camera lateral position h. The sensitivity of astigmatism and coma in the measured wavefront departure to camera lateral position h is given in Sec. 3.2.1

$$\frac{\partial W_{222}}{\partial h} = \frac{2hr^2}{Rd^2} \tag{5.1}$$

$$\frac{\partial W_{131}}{\partial h} = \frac{r^3\left(d-R\right)}{R^2d^2} \tag{5.2}$$

If we calibrate the test with a reference surface which has small ΔR comparing to the test optics, assuming the camera and the display are near paraxial conjugate of test optics, the sensitivity of astigmatism and coma to camera lateral position h can be approximated as

$$\frac{\partial W_{222}}{\partial h} = \frac{2hr^2}{R^2d^2}\Delta R \tag{5.3}$$

$$\frac{\partial W_{131}}{\partial h} = \frac{r^3\left(R-2d\right)}{R^3d^2}\Delta R \tag{5.4}$$

Comparing Eq. (5.1) and Eq. (5.3), Eq. (5.2) and Eq. (5.4), the sensitivity of astigmatism is reduced by a factor of $\frac{\Delta R}{R}$, and coma is reduced by $\frac{\left(R-2d\right)\Delta R}{R}$.

For the improvement of test sensitivity on display tilt, we use the same geometry as shown in Figure 3.6. Take y slope sensitivity as an example. For defocus-dominated test configurations, without reference calibration, slope error ΔS_y due to display tilt θ is obtained by calculating ε_y using Eq.(3.2) and substituting ε_y into Eq. (3.21):

$$\Delta S_y \simeq \frac{2(R-d)r \cdot y_p}{R} \cdot \left(1 - \frac{\cos\gamma}{\cos(\gamma+\theta)}\right) \cdot \frac{1}{d} \tag{5.5}$$

With reference calibration, assuming the differences of γ and β are negligible between test mirror and calibration reference (ΔR is small), the measurement error is reduced to

$$\Delta S_y \simeq \frac{2d \cdot r \cdot y_p \cdot \Delta R}{R^2} \cdot \left(1 - \frac{\cos\gamma}{\cos(\gamma+\theta)}\right) \cdot \frac{1}{d} \tag{5.6}$$

Eq. (5.5) and Eq.(5.6) show that reference calibration helps reduce ΔS_y by a factor of $\frac{R(R-d)}{\Delta R d}$.

5.2 Reduced sensitivity on other systematic errors

The validation of reference calibration procedure requires the reference surface shape not have a large departure from the test optics so that they share a similar light path and geometry sensitivity in the measurement. Besides sharing same camera distortion and perspective, the similar light path guarantees the two

measurements use same local screen region, the defect from which can also be subtracted.

5.3 Error from reference surface

Although system error in SCOTS can be greatly reduced by reference calibration, directly subtracting a single measurement of the flat mirror could introduce the surface error of the reference surface itself into the measurement. The reference surface usually has better surface quality than the test optics so that the error from reference surface can be ignored. However, when the test optics has similar or superior surface quality as the reference surface, it becomes necessary to compensate the surface error from the reference surface to further improve the measurement accuracy.

One possible solution to eliminate error from reference surface is a random test of reference surface. In the experiment, the reference surface can be translated randomly and a series of random patches on the reference surface is measured. By averaging the measurement results of random test, the imperfection from reference surface is averaged out leaving only fixed systematic error from test system. Subtracting the systematic error map from the measured surface map of test optics, system error is removed from the calibration.

5.4 Application example: X-ray mirror surface metrology

System calibration using a reference surface was implemented in testing a high precision X-ray mirror. The measured off-axis elliptical X-ray mirror was 100 mm

long and 50 mm wide with a working area of 90mm by 8 mm. The local radius of curvature of the mirror was around 260 m with maximum surface sag around 4.5 μm. The overall shape error in the useful area of the mirror was less than 1nm RMS, based on inspection report from the manufacturer.

5.4.1 Test system setup

The SCOTS test setup is shown in Figure 5.1(a). The illumination screen, set up 2.7 meters away from the mirror, was a 19" LCD display chosen to give enough illumination area for this 100 mm long elliptical mirror. The camera, which was composed of a 1/3" CCD sensor and a commercial camera lens of 50 mm focal length, was set up right next to the LCD screen to capture the reflected screen image.

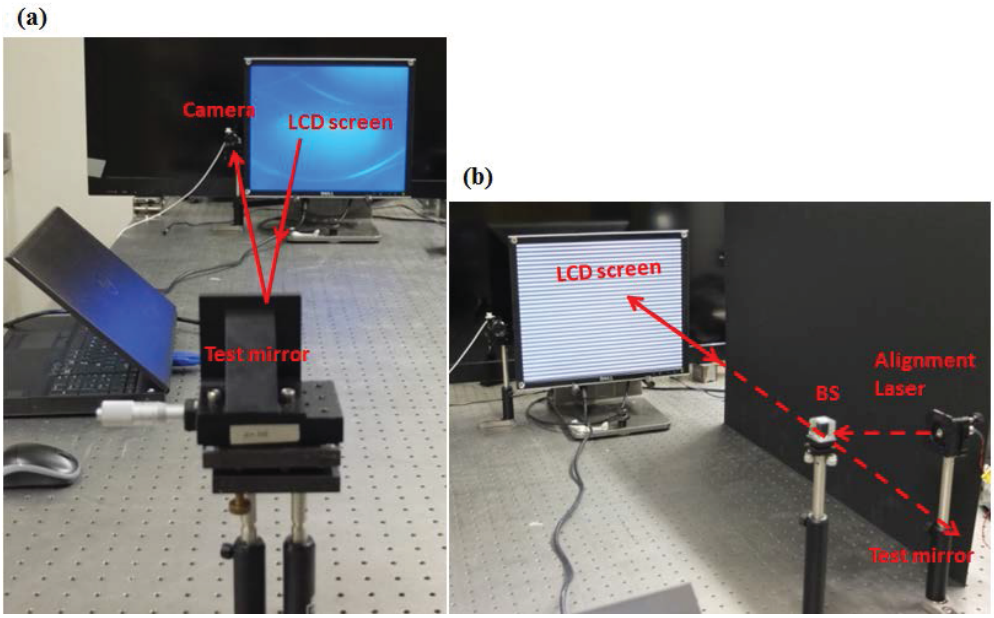

Figure 5.1 (a) Experiment SCOTS setup. (b) Geometry control with an alignment laser

5.4.2 Noise estimation

Averaging measurements were conducted to reduce the noise in the measurement, which was probably induced by the stability of mechanical mounts, thermal expansion, detector noise, and etc. The residual error in the average map was estimated using the method mentioned in Ref [47]. 600 measurements were taken and N maps were chosen at random and averaged. The comparison of $\overline{W_N}$ and total averaged map $\overline{W_{600}}$ is plotted in Figure 5.2. In Figure 5.2 (b), the fitted line has a slope of -0.53, indicating the dominated noise was random noise which drops approximately as $1/\sqrt{N}$. From Figure 5.2, the error in the final surface map was less than 0.1nm RMS with 200 averages. Therefore, we chose 200 averages in the test for high precision measurement.

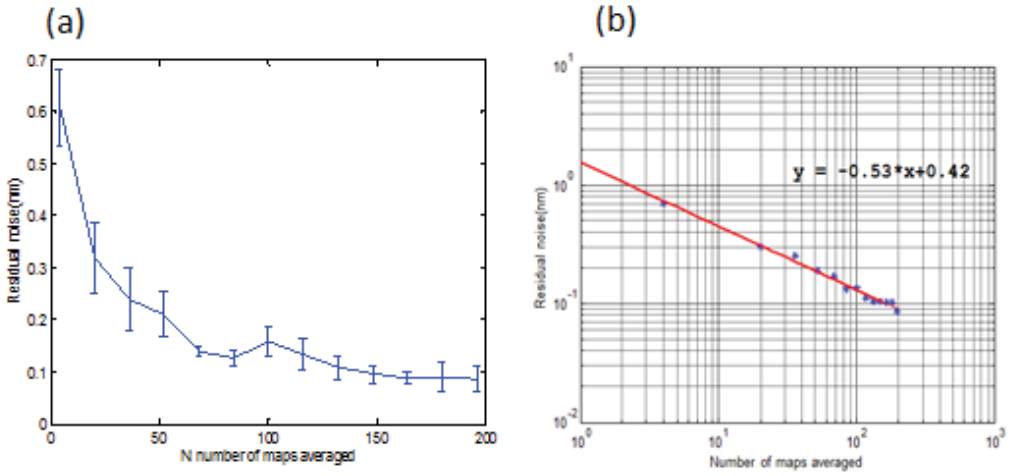

Figure 5.2 Estimated residual noise in average of N maps in (a) normal scale (b) log-log plot

5.4.3 Calibration with a reference flat

In our test, a 300 mm x 50 mm high-precision flat mirror was used as a reference surface. The precision flat was carefully aligned at the test mirror position with 1μm accuracy in distance and 10 μrad in tip/tilt. As pointed out in Sec.5.1, a geometry sensitivity analysis with and without reference flat calibration was performed and the comparison is provided in **Table 5.1**

Table 5.1 Geometry sensitivity of SCOTS test of X-ray mirror

System geometry uncertainty	Measurement uncertainty with power removed (nm RMS)	
	Without flat calibration	With flat calibration
1 mm camera x position uncertainty	0.02	0.02
1 mm camera y position uncertainty	0.002	0.002
1 mm camera z position uncertainty	0	0
0.05° screen tilt about x-axis	0.01	0
0.05° screen tilt about y-axis	0.54	0.05
1mm screen z position uncertainty	0	0

The coordinates were setup locally at the mirror where the x direction was along the long side of the mirror, the y direction was along the short side of the mirror and the z direction was perpendicular to the slope of mirror center. This SCOTS test was very insensitive to the positioning of the components, except for the relative tilt between the screen and mirror about the y-axis. This is understandable since the elliptical mirror only has optical power in the x direction. Comparing column 3 and column 2 in **Table 5.1**, reference calibration greatly reduced geometry sensitivity on elements tilt. Measurement error due to 0.05° screen tilt about y-axis was only about 0.05 nm RMS if apply reference

calibration, which was 10 times smaller than the test without the reference calibration. Measurement error due to camera lateral shift cannot be compensated by the reference calibration since it only caused a constant shift of the measured screen coordinate, and was removed in the data reduction as a piston term.

5.4.4 Measurement results

The measurement result of the X-ray mirror is given in Figure 5.3. It is clear by comparing Figure 5.3(a) and (b) that the measurements were dominated by systematic errors, which were a combination effect of geometry uncertainty and camera lens, display defects. Shown in Figure 5.3 (c), after subtracting the reference calibration (Figure 5.3 (b)) from the uncalibrated map (Figure 5.3 (a)), the major systematic error was removed and the measured surface RMS of the elliptical X-ray mirror was reduced to 0.62 nm.

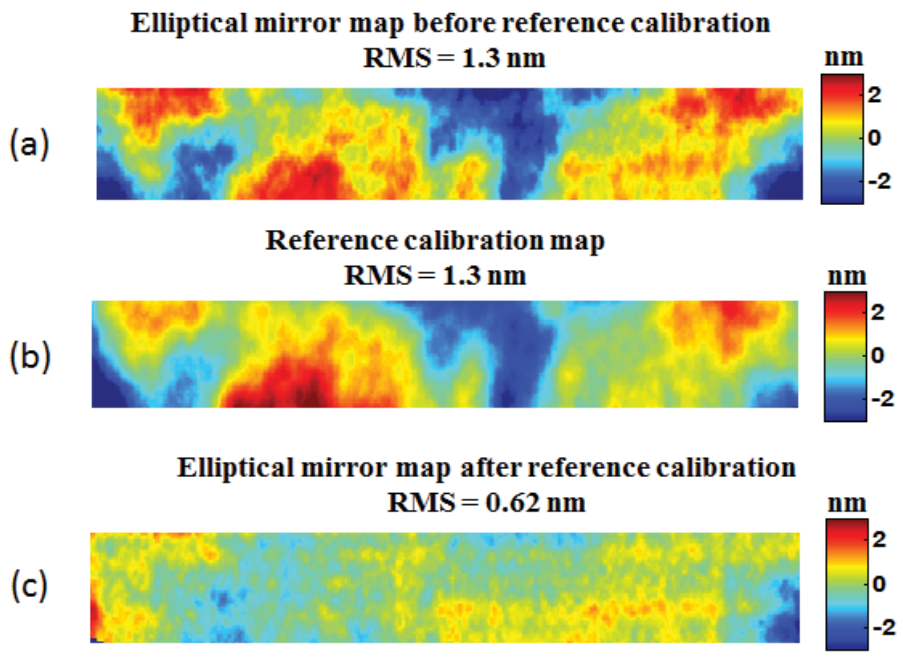

Figure 5.3 (a) Measured surface irregularity of the elliptical mirror before reference calibration applied, RMS = 1.3 nm; (b) Averaged calibration map with translation of reference flat, RMS = 1.3 nm; (c) Surface map of elliptical mirror with calibration of reference applied, RMS = 0.62 nm.

For an ideal random test, RMS error from reference surface drops as $\frac{1}{\sqrt{N}}$, where N is the total number of measurements. Therefore, the slope in log-log plot of measured surface RMS as a function of number of measurements is -0.5. To check the residual error from the reference surface in the average map, I evaluated the slope of the measurement data using the same method described in Sec. 5.4.2. N maps (N = 1,2,3,4) were randomly selected and averaged. After subtracting the averaged map (W), the fitted slope of residual RMS in log scale was about -0.7, indicating certain correlation existed between the 8 maps and

therefore some residual error from reference surface stayed in the averaged map in Figure 5.3 (b). Small shear step between each measurement, which was limited by the relative size of the test surface and reference surface, might be the major cause that reduced the effectiveness of the random test. In practical measurement, it is always good to have a large shear of the reference flat to reduce the correlation between different sample patches. Rotation of the reference flat can also help to increase the test efficiency.

6 CONCLUSION

SCOTS is a promising, non-contact, high dynamic-range and full-field metrology technique. The basic slope measurement principle allows easy adaptation for SCOTS to the measurement of any free-form optics without using null optics. Careful calibrations of the system make the measurement achieve comparable accuracy with interferometry testing but at lower cost and easy setup.

This dissertation provides a thorough analysis of three major SCOTS components: geometry, camera and display. Calibrations of these components have also been investigated in detail and implemented in practical metrology projects. The application examples of the calibration methods and excellent measurement results stand out engineering significance of this dissertation.

APPENDIX A: OPTICAL METROLOGY OF A LARGE DEFORMABLE ASPHERICAL MIRROR USING SOFTWARE CONFIGURABLE OPTICAL TEST SYSTEM

Run Huang, Peng Su, Todd Horne, Guido Brusa, Jim H. Burge

Published in Optical Engineering, August, 2014

COPYRIGHT TRANSFER AGREEMENT

Tue 9/1/2015 8:34 AM

From: Nicole Harris <nicoleh@spie.org>

To: Run Huang <rhuang@optics.arizona.edu>;

Dear Run Huang,

Thank you for seeking permission from SPIE to reprint material from our publications. As author, SPIE shares the copyright with you, so you retain the right to reproduce your paper in part or in whole. Publisher's permission is hereby granted under the following conditions:

(1) the material to be used has appeared in our publication without credit or acknowledgment to another source; and

(2) you credit the original SPIE publication. Include the authors' names, title of paper, volume title, SPIE volume number, and year of publication in your credit statement.

Sincerely,

Nicole Harris

Administrative Editor, SPIE Publications

1000 20th St.

Bellingham, WA 98225

+1 360 685 5586 (office)

nicoleh@spie.org

Optical Engineering

OpticalEngineering.SPIEDigitalLibrary.org

Optical metrology of a large deformable aspherical mirror using software configurable optical test system

Run Huang
Peng Su
Todd Horne
Guido Brusa
Jim H. Burge

SPIE.

Optical Engineering 53(8), 085106 (August 2014)

Optical metrology of a large deformable aspherical mirror using software configurable optical test system

Run Huang,[a,*] Peng Su,[a] Todd Horne,[a] Guido Brusa,[b] and Jim H. Burge[a]
[a]The University of Arizona, College of Optical Sciences, Tucson, Arizona 85721, United States
[b]The University of Arizona, Steward Observatory and Large Binocular Telescope, Tucson, Arizona 85721, United States

Abstract. The software configurable optical test system (SCOTS) is an efficient metrology technology based on reflection deflectometry that uses only a liquid-crystal display and a camera to measure surface slope. The surface slope is determined by triangulation using the co-ordinates of the display screen, camera, and test mirror. We present our SCOTS test results concentrated on high dynamic range measurements of low order aberrations. The varying astigmatism in the 910-mm diameter aspheric deformable secondary mirror for the large binocular telescope was measured with SCOTS, requiring no null corrector. The SCOTS system was designed on-axis with camera and screen aligned on the optical axis of the test mirror with the help of a 6-inch pellicle beam splitter. The on-axis design provides better control of the astigmatism in the test. The high dynamic range of the slope provided a measurement of astigmatism within 0.2-μm root-mean-square accuracy in the presence of 231-μm peak-to-valley aspheric departure. The simplicity of the test allowed the measurements to be performed at multiple gravity angles. [DOI: 10.1117/1.OE.53.8.085106]

Keywords: deflectometry; optical metrology; aspheric; software configurable optical test system.

Paper 140673P received Apr. 23, 2014; revised manuscript received Jul. 13, 2014; accepted for publication Jul. 16, 2014; published online Aug. 15, 2014.

1 Introduction

Interferometry has served as an accurate noncontact optical metrology technology for a long time. The wave nature of light gives this technology subwavelength precision and accuracy; however, it typically has a small dynamic range. Traditional null testing interferometry can only measure the surface departures within a few wavelengths from reference shapes. For measuring aspheric or freeform optics, interferometry usually requires compensation optics such as a computer-generated hologram. Sometimes a stitching process is also required for measuring large aspheric optics, which makes interferometry testing costly and inflexible. In addition, interferometry requires a normal incidence that leads to tedious alignment and calibration to perform accurate testing.[1,2] The software configurable optical test system (SCOTS), a slope measurement technique based on deflectometry, provides a contact-free, high dynamic range, full field metrology method with easy system setup and alignment. It is able to achieve high dynamic range slope measurements by using computer-controlled large displays such as liquid-crystal display (LCD) monitors. The camera in SCOTS provides a full-field of view of the test optics and a 2-D surface map can be obtained within one measurement, thus, no stitching is needed. The performance of SCOTS has been successfully demonstrated in testing many large astronomy telescope mirrors and precision x-ray mirrors.[3–7]

In this paper, we show SCOTS test results for a 910-mm diameter aspheric deformable secondary mirror for the large binocular telescope (LBT).[8,9] The observatory noticed an elevation dependent astigmatism in its secondary. A compact SCOTS system was taken to the observatory to further investigate this aberration. A series of tests demonstrated that the SCOTS accurately measured the astigmatism to submicrometer accuracy in the presence of a 231-μm peak-to-valley aspheric departure.

The paper is organized as follows. In Sec. 2, we describe the principle of SCOTS as a Hartmann test in reverse. In Sec. 3, we provide a detailed discussion of the system design, expected performance, alignment procedures, and test results. Conclusions are given in Sec. 4.

2 Principle

SCOTS uses deflectometry to measure slopes by triangulation. It works like a Hartmann test[10] but in reverse. Figure 1 shows the schematic comparison of Hartmann and SCOTS tests. In a Hartmann test, a point source of light is placed near the center of curvature of the test mirror, and a plate with a number of holes is centered just in front of the test mirror. The point source illuminates the entire test mirror, but only the light passing through the holes is reflected. One or more images are recorded for slope calculations. In SCOTS, the detector in Hartmann test is replaced by an LCD screen and the point source is replaced by a camera focusing on the test mirror to detect the light reflected from the display.

When testing a polished optical surface, we are usually interested in the surface departure of the testing surface from its ideal shape. We approximate the wavefront slopes to be equal to Eq. (1) based on the transverse ray aberration model[11]

$$\frac{\partial W(x,y)}{\partial x} \cong -\frac{\Delta x_{\text{screen}}}{d_{m2\,\text{screen}}}, \frac{\partial W(x,y)}{\partial y} \cong -\frac{\Delta y_{\text{screen}}}{d_{m2\,\text{screen}}}, \quad (1)$$

*Address all correspondence to: Run Huang, E-mail: rhuang@optics.arizona.edu

0091-3286/2014/$25.00

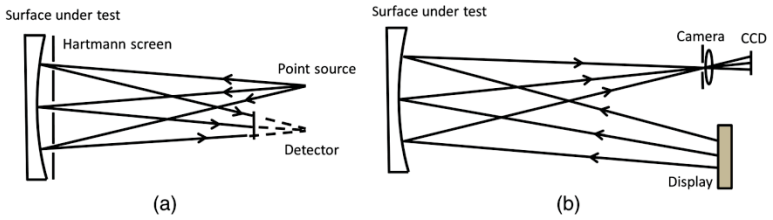

Fig. 1 Schematic setup of (a) a Hartmann test and (b) a software configurable optical test system (SCOTS) test. SCOTS traces rays in reverse.

$$\Delta x_{\text{screen}} = x_{\text{measured}} - x_{\text{ideal}} \quad \Delta y_{\text{screen}} = y_{\text{measured}} - y_{\text{ideal}}, \tag{2}$$

where $W(x, y)$ is the wavefront aberration and $d_{m2\,\text{screen}}$ is the distance from the mirror to the display. The measured x and y positions (x_{measured} and y_{measured}) are determined by phase shifting or line scanning techniques.[3] The ideal x and y positions (x_{ideal} and y_{ideal}) are determined by ray tracing for the case of an ideal optical surface. From these slopes, a wavefront map is reconstructed by zonal integration.

3 SCOTS Test for a Large Deformable Aspherical Mirror

3.1 *On-Axis SCOTS*

As mentioned in Sec. 1, the LBT secondary mirror is an $f/1.1$ deformable ellipsoid with a 910-mm diameter and a 231-μm aspheric departure. Although SCOTS allows an off-axis configuration as shown in Fig. 1(b), sensitivity to alignment errors can be reduced by maintaining coaxial alignment of the camera, display, and test mirror for measuring axisymmetric mirrors. The dominant aberration in the LBT secondary is astigmatism and it can be described using Seidel sums as[12]

$$W_{222} = \frac{1}{2} S_{\text{III}}, \tag{3}$$

$$S_{\text{III}} = -\sum \bar{A}^2 y \Delta\left(\frac{u}{n}\right), \tag{4}$$

$$\bar{A} = n\bar{u} + n\bar{y}c, \tag{5}$$

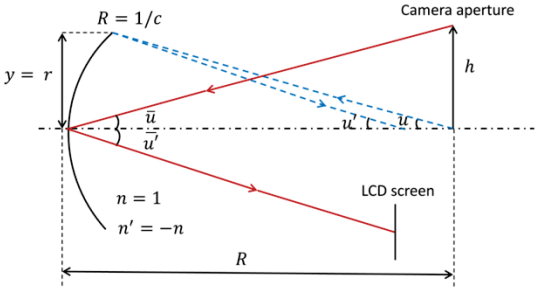

Fig. 2 Ray tracing in SCOTS for Seidel coefficient calculation.

$$\Delta\left(\frac{u}{n}\right) = \left(\frac{u'}{n'}\right) - \left(\frac{u}{n}\right), \tag{6}$$

where $\bar{y}$ is chief ray height, y is marginal ray height, $\bar{u}$ and $\bar{u}'$ are the chief ray angles before and after reflection, and u and u' are marginal ray angles before and after reflection, respectively.

Applying Eqs. (3)–(6) to a SCOTS test, two rays are traced through the system, the marginal ray for full aperture (Fig. 2 dashed ray, $y = r$) and the chief ray (Fig. 2 solid ray, $\bar{y} = 0$) at the maximum field, (i.e., the camera off-axis distance, h). Using the paraxial approximation, we can get an astigmatism of

$$W_{222} = \frac{h^2 r^2}{R^3}. \tag{7}$$

The sensitivity of astigmatism to the camera off-axis distance is

$$\frac{\partial W_{222}}{\partial h} = \frac{2\,hr^2}{R^3}. \tag{8}$$

Equation (8) shows that the alignment sensitivity of astigmatism to test geometry increases linearly as a function of the off-axis distance of the camera. Figure 3 plots the sensitivity for LBT secondary mirror SCOTS test. If we use a test geometry with the camera at a 100-mm off-axis distance (i.e., $h = 100$ mm) and have a 0.1-mm uncertainty of camera lateral position, there will be a 0.5-μm uncertainty for W_{222} in the measurement. However, if we use an on-axis geometry (i.e., $h = 0$ mm), a 0.1-mm camera lateral distance

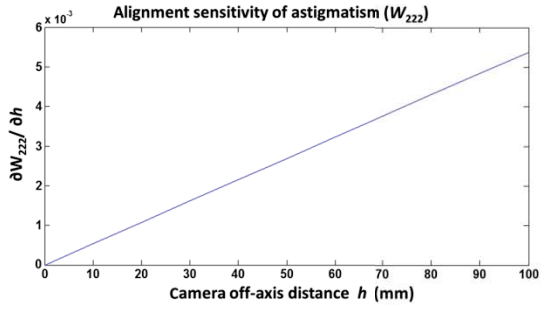

Fig. 3 A plot showing the SCOTS alignment sensitivity of astigmatism due to the camera off-axis distance for the large binocular telescope secondary mirror.

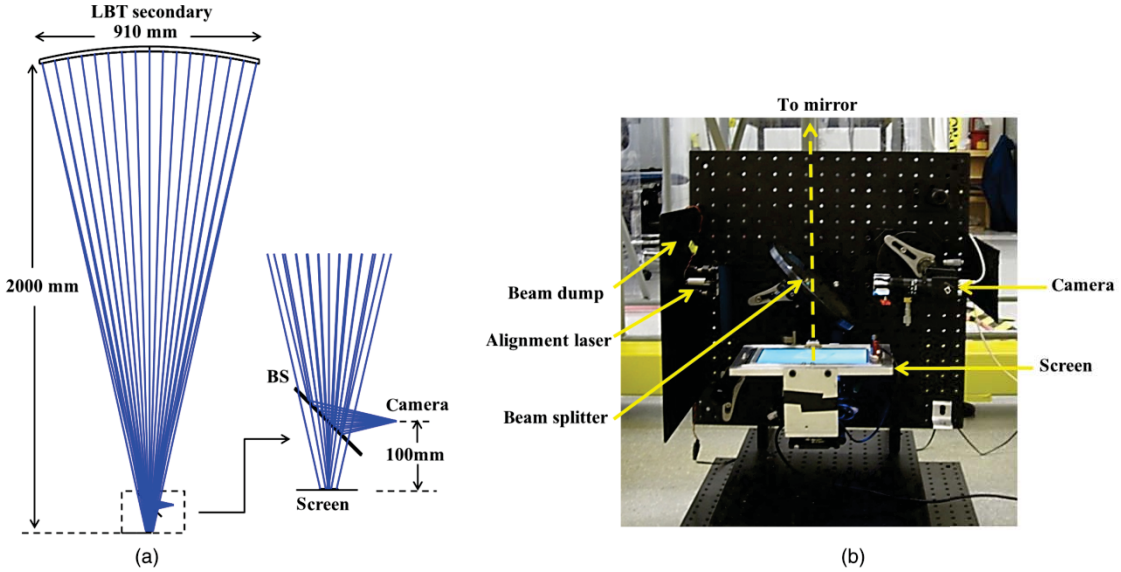

Fig. 4 (a) Geometry layout of the on-axis SCOTS test and (b) experiment setup.

uncertainty will only generate a 0.3-nm uncertainty for W_{222} in the test. Therefore, an on-axis design makes the SCOTS test less sensitive to geometric uncertainty in component positions and reduces test geometry induced astigmatism in the measurements.

It is worth mentioning that the coaxial alignments of the camera, LCD, and the test mirror also makes the camera view of the test mirror free from perspective distortion which is a major difficulty with many SCOTS tests and has to be calibrated out by putting customized fiducial targets on the test mirror.[5]

The on-axis SCOTS setup for the LBT secondary mirror measurement is shown in Fig. 4. A 7-inch mini LCD screen with a 190.5-μm pixel pitch is aligned at the center of curvature of the secondary mirror to illuminate the test mirror; a 6-inch pellicle beam splitter with a 2-μm thickness is set between the screen and test mirror and is 100 mm away from the LCD screen. A camera is put into the reflection path of the beam splitter. The camera lens has a 1-mm external aperture and a 6-mm focal length with a 42-deg field-of-view. The distance between the camera and the beam splitter is also set at 100 mm. An alignment laser is placed opposite to the camera and is used for creating a reference axis in the alignment, which will be discussed in detail in Sec 3.3. A beam dump is also used to prevent stray light from entering the camera.

3.2 *Effect of Beam Splitter*

As stated in Sec 3.1, the use of a pellicle beam splitter makes the test components coaxial to reduce the sensitivity of the test to alignment. However, the beam splitter inherently adds errors to the measurement due to its thickness and shape variation. In this section, we will discuss the effects of these two potential issues in the LBT secondary SCOTS test.

To consider the effect of constant thickness, the beam splitter is treated as a plane parallel plate (PPP), which causes a lateral displacement of the rays passing through it. For small angles, the lateral displacement D can be approximated as[13]

$$D \approx \frac{TI(n-1)}{n}, \tag{9}$$

where T is the thickness of the beam splitter and I is the incident angle on the beam splitter.

When a PPP is used with collimated light, no aberration is introduced. However, as shown in Fig. 5, and in a SCOTS test, the beam splitter is used with converging light where astigmatism, coma, and spherical aberrations arise. To compute the magnitude of this effect in the test, we added 2 μm

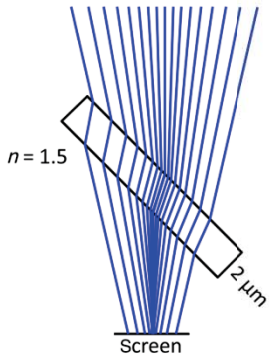

Fig. 5 The constant thickness of the beam splitter introduces aberrations when it is used with converging light.

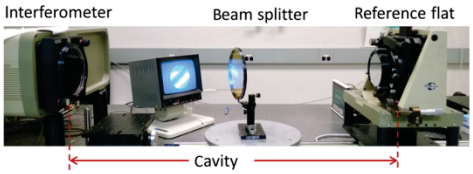

Fig. 6 Experiment setup to measure the thickness variation of the pellicle beam splitter.

to the thickness of the beam splitter in the LBT secondary SCOTS test model using ZEMAX. The ray trace result showed that it merely generated 3.4-nm RMS wavefront errors (mainly astigmatism). Therefore, the measurement error coming from the constant thickness of the beam splitter can be ignored for this test because it did not require nanometer level accuracy.

The thickness variation of the beam splitter was measured in transmission with a Fizeau interferometer as shown in Fig 6. The difference map [Fig. 7(a)] shows that there are low order thickness fluctuations (2 to 4 cycles/aperture) in the beam splitter. Figure 7(b) is the integrated one-dimensional power spectral density plot [PSD(υ)] of the difference map [Fig. 7(a)]. Using Eq. (10), the RMS value at a certain spatial frequency can be calculated[14]

$$\mathrm{rms} = \sqrt{\int_{\upsilon 1}^{\upsilon 2} \mathrm{PSD}(\upsilon) d\upsilon}. \tag{10}$$

Based on the above experiment and PSD analysis, three sine shape surface sags at 1, 4, and 10 cycles/aperture with RMS amplitude of 3, 0.5, and 0.05 nm, respectively, were added to the front surface of the beam splitter in the LBT secondary SCOTS ZEMAX model. The ray trace result showed that the introduced measurement error was on the level of 1-nm RMS for the wavefront and 10^{-8} rad for the wavefront slope, which was also negligible.

The experiments and analysis above are general and may be extended to similar deflectometry systems using a beam splitter to make an on-axis alignment. It will help to quantify and budget the effect of a beam splitter during test design.

Table 1 Tolerance analysis for large binocular telescope secondary mirror on-axis SCOTS test.

Wavefront (unit: μm)	Camera lateral shift 1 mm	Mirror tilt 0.35 deg	Mirror z shift 20 mm	Screen tilt 0.3 deg	Root sum square
Z5 (astigmatism)	0	0	0	0	0
Z6 (astigmatism)	0.005	0.78	0	0.001	0.78
Z7 (coma)	0.011	0.19	0	0.056	0.20
Z8 (coma)	0	0	0	0	0
Z9 (trefoil)	0	0	0	0	0
Z10 (trefoil)	0	0	0	0	0
Z11 (spherical)	0	0.006	0.21	0	0.21

3.3 *System Alignment*

The observatory required better than 1-μm RMS sensitivity in the measurement of astigmatism. Therefore, we designed the mechanics and the alignment procedure based on the tolerance analysis in Table 1. The tolerance shows that the astigmatism is very sensitive to the mirror tilt, whereas it is insensitive to the screen tilt and the longitudinal distance from SCOTS to the mirror.

The designed alignment was separated into two steps. The first step was the in-lab integration of the SCOTS package with prealignment of the components. The second step was the alignment of the test mirror and the SCOTS package at the observatory.

An alignment laser, placed on the opposite side of the beam splitter to the camera (depicted in Fig. 8), shot a collimated beam to the beam splitter with 50% of the light transmitted and 50% reflected. The laser beam served as the reference optical axis for the whole system. The first step of the prealignment (Fig. 8①) was to align the camera's

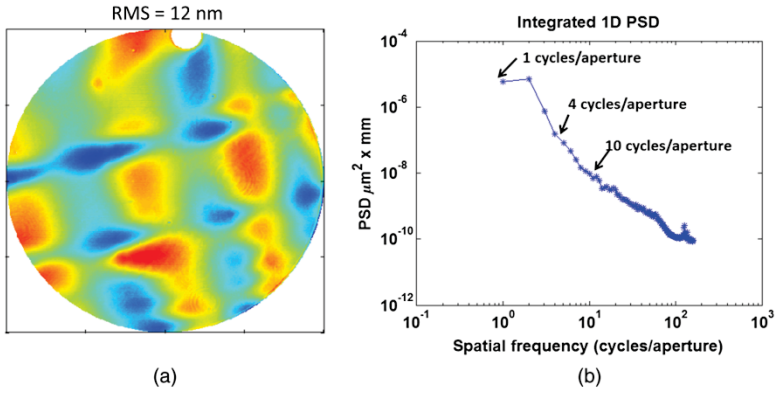

Fig. 7 (a) Difference map with and without beam splitter in the light path. (b) One-dimensional power spectral density of (a).

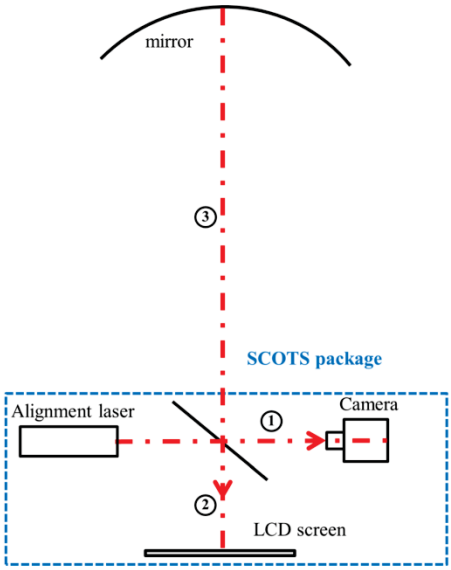

Fig. 8 Alignment of SCOTS test. The SCOTS package was prealigned before taken to the observatory. The on-axis alignment was achieved with the help of an alignment laser.

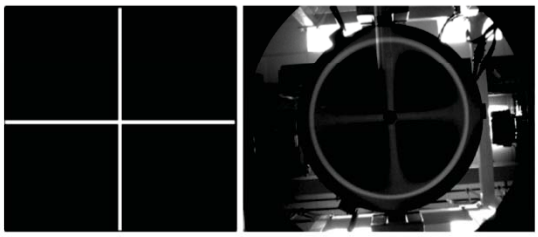

(a) (b)

Fig. 9 (a) A bright cross on the screen was lit up to illuminate the mirror. (b) Reflected image of the cross on the mirror.

aperture and the center of the CCD onto the laser beam. The camera was translated so that the laser beam with ~1-mm diameter was able to go through the 1-mm external aperture of the camera. Subsequently, by tip-tilting the camera and monitoring the centroid of the laser beam incident on the CCD, the laser beam was positioned at the center of the camera sensor within a 0.1-pixel accuracy. The second step of the prealignment (Fig. 8②) was to align the LCD screen perpendicular to the laser beam by adjusting its tip-tilt so that the laser beam reflected by the screen went back through the aperture of the alignment laser. The position where the laser beam was incident on the LCD screen was recorded for the second alignment step. With these prealignment steps, the SCOTS package was sent to the observatory.

Once at the LBT observatory, the SCOTS package had to be aligned with the secondary mirror (Fig. 8③) so that (1) the mirror was centered on the CCD and (2) the mirror was perpendicular to the SCOTS axis. The mirror centering was controlled to ~0.2-mm accuracy by fitting a circle to the image of the mirror boundary where the center of the circle could be calculated with sub pixel accuracy. The major challenge in aligning the secondary mirror normal to the reference optical axis was the central obscuration on the mirror, which made it impossible to use a vertex reflection of the laser beam. Instead, we used a bright cross [see Fig. 9(a)] produced by the LCD screen at the previously recorded position. By adjusting the mirror tip-tilt and having both the mirror and the reflected cross centered on the CCD, [as shown in Fig. 9(b)], the mirror was aligned with its vertex perpendicular to the optical axis. Considering the limitation of the mechanical mounting of the mirror and the width of the reflected cross, we estimated the mirror tilt was aligned within 0.1-deg accuracy.

With the two-step alignment procedures, the test setup was aligned within the tolerance and was capable of measuring astigmatism with submicrometer accuracy.

3.4 *Test Results*

The performance of the low-order aberration measurement of this SCOTS was first verified with the secondary mirror pointing straight down as shown in Fig. 10(a). Intensity

(a) (b)

Fig. 10 SCOTS test of the secondary mirror with mirror (a) pointing straight down and (b) at 30-deg elevation position.

sinusoidal fringes were displayed on the LCD screen in the x and y directions and a four-step phase-shifting algorithm was used to register the mirror pixel coordinates with the screen pixel coordinates. Figure 11 shows camera captured raw intensity maps of the sinusoidal fringes reflected by the mirror and Fig. 12 shows the calculated LCD screen position. At this position, SCOTS measured ~0.2-μm (RMS) astigmatism. This 0.2 μm (RMS) might be the combined effect from the alignment uncertainty, the systematic error in SCOTS, and a small amount of inherent errors in the secondary mirror.

After the initial measurement, a series of controlled aberration, 1-μm astigmatism (RMS), 1-μm coma (RMS), and 1-μm trefoil (RMS) wavefront errors were intentionally added using the deformable secondary mirror and SCOTS accurately measured these aberrations with submicrometer accuracy. The wavefront maps shown in Fig. 13 are the commanded wavefronts, measured wavefronts, and the difference. The repeatability of the test is 2-μrad RMS in slope and 98-nm RMS in wavefront, taking measurements at the same test configuration several times.

After the verification tests with the secondary mirror pointing straight down, this compact SCOTS system was then used to measure the secondary mirror at a different elevation. Figure 10(b) shows the test configuration at a 30-deg elevation (i.e., optical axis at 60-deg from vertical). Moving the mirror to a 30-deg elevation introduced a large amount of astigmatism, the value of which is a function of the path followed (hysteresis). As shown in Table 2, reaching a 30-deg elevation from the vertical position caused an ~6.2-μm RMS astigmatism but only an ~3.7-μm RMS astigmatism when the position was reached from horizon pointing (i.e., optical axis horizontal). This test result confirmed previous measurements taken with the unit installed at the telescope, including the hysteretic behavior of the introduced aberration. Several other SCOTS measurements were also done after modifying the secondary mirror hardware configuration in an attempt to determine the causes of this aberration. Although no direct cause was found, the measurements eliminated several potential causes. The results obtained will help the observatory design a series of tests to further investigate the source of the astigmatism.

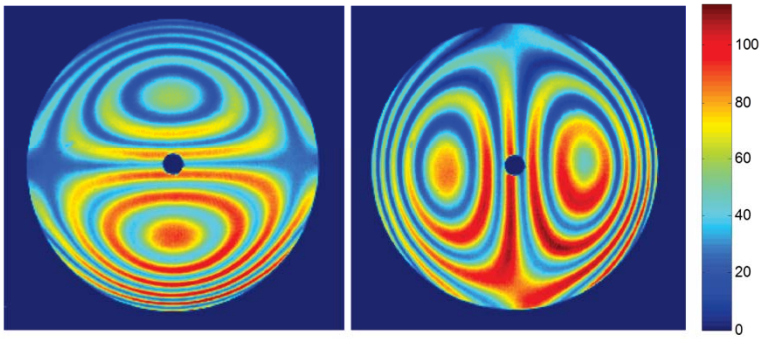

Fig. 11 Raw intensity images of the sinusoidal fringes reflected by the mirror.

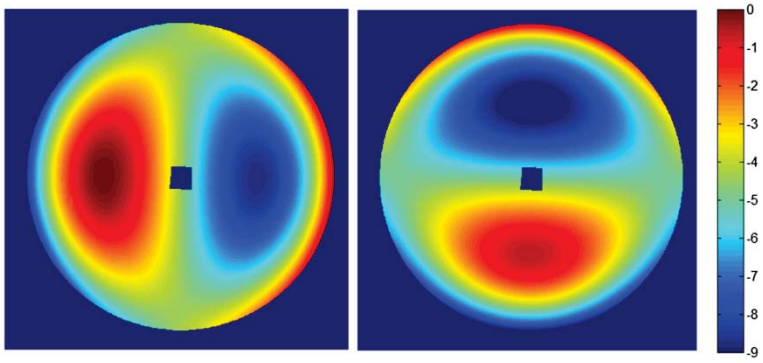

Fig. 12 Measured liquid-crystal display screen position in x and y directions (unit: mm). Those positions were calculated by phase unwrapping algorithm. The secondary mirror is an $f/1.1$ ellipsoid with 231-μm aspheric departure, so the measured wavefront was dominated by spherical aberration and consequently the above patterns show a coma shape (SCOTS directly measures the slopes of wavefront).

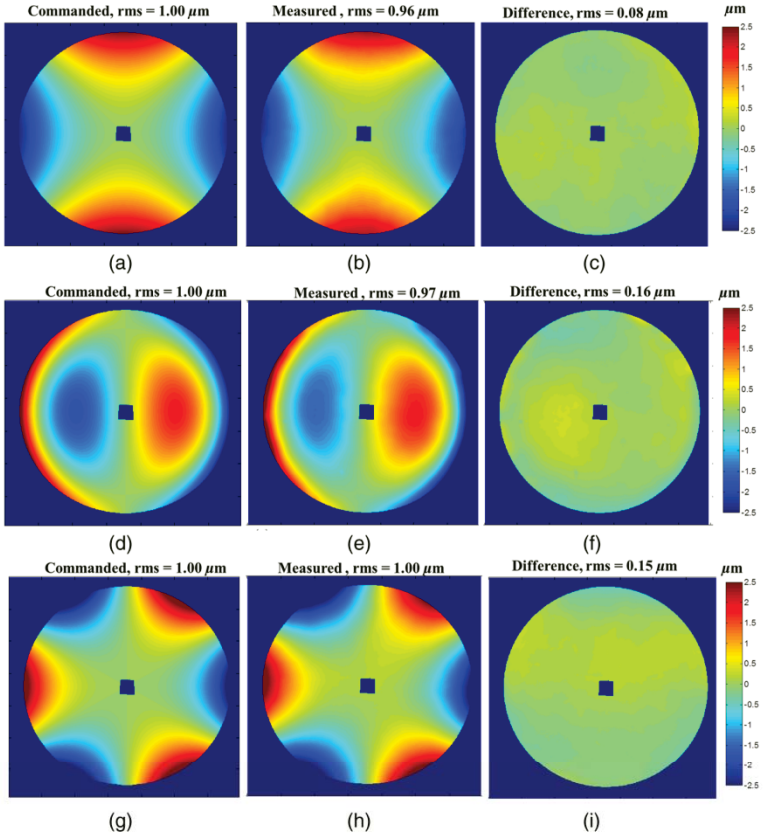

Fig. 13 SCOTS measurement results with controlled aberration in secondary mirror. Unit: μm. (a), (d), and (g) are commanded wavefront aberrations which are 1-μm RMS astigmatism, 1-μm RMS coma, and 1-μm RMS trefoil, respectively. (b), (e), and (h) are SCOTS measured wavefront aberrations. (c), (f), and (i) are the differences between commanded and measured wavefront aberrations.

Table 2 Measured astigmatism by reaching 30-deg from zenith position and horizon position.

Test sequence	Straight down to 30 deg	Horizon to 30 deg
Astigmatism	6.21 μm	3.75 μm

4 Conclusion

An on-axis SCOTS was successfully constructed to measure low order aberrations in the presence of a large spherical departure with submicrometer accuracy. The SCOTS does not require using a null lens and is very compact, allowing us to easily measure the aberrations at multiple mirror orientations with respect to gravity. Unlike previous SCOTS systems, this new on-axis setup does not require perspective corrections. Furthermore, the use of off-the-shelf products for the LCD screen and camera makes this system cost-effective. A detailed study of the beam splitter was presented, which can help us to budget its effect in future SCOTS tests.

To advance this technology to a higher accuracy level, careful calibrations related to system geometry, lens imaging aberration, stray light, etc., need to be performed. Continuing research on the SCOTS system calibration is being conducted in our group to improve the accuracy of the test to a nm or even a subnanometer RMS.

References

1. M. Knauer, J. Kaminski, and G. Hausler, "Phase measuring deflectometry: a new approach to measure specular free form surfaces," *Proc. SPIE* **5457**, 366–376 (2004).
2. C. Faber et al., "Deflectometry challenges interferometry: the competition gets tougher!," *Proc. SPIE* **8493**, 84930R (2012).
3. P. Su et al., "Software configurable optical test system: a computerized reverse Hartmann test," *Appl. Opt.* **49**(23), 4404–4412 (2010).
4. P. Su et al., "Precision aspheric optics testing with the SCOTS: a deflectometry approach," *Proc. SPIE* **8788**, 87881E (2013).
5. P. Su et al., "SCOTS: A reverse Hartmann test with high dynamic range for giant Magellan telescope primary mirror segments," *Proc. SPIE* **8450**, 84500W-1 (2012).
6. P. Su et al., "Non-null full field x-ray mirror metrology using SCOTS: a reflection deflectometry approach," *Opt. Express* **20**(11), 12393–12407 (2012).
7. R. Huang et al., "X-ray mirror metrology using SCOTS/deflectometry," *Proc. SPIE* **8848**, 88480G (2013).
8. A. Riccardi et al., "The adaptive secondary mirror for the Large Binocular Telescope: optical acceptance test and preliminary on-sky commissioning results," *Proc. SPIE* **7736**, 77362C (2010).
9. R. Huang et al., "Measurement of a large deformable aspherical mirror using SCOTS (Software Configurable Optical Test System)," *Proc. SPIE* **8838**, 883807 (2013).

10. D. Malacara-Doblado and I. Ghozeil, "Hartmann, Hartmann-Shack, and other screen tests," in *Optical Shop Testing*, 3rd ed., D. Malacara, Ed., Wiley Series in Pure and Applied Optics, pp. 361–397, Wiley, New Jersey (2007).
11. J. L. Rayces, "Exact relation between wave aberration and ray aberration," *Opt. Act.* **11**, 85–88 (1964).
12. J. Sasián, *Introduction to Aberrations in Optical Imaging Systems*, Cambridge University Press, New York (2013).
13. J. C. Wyant and K. Creath, "Basic wavefront aberration theory for optical metrology," *Appl. Opt. Opt. Eng.* **11**, S29 (1992).
14. R. N. Youngworth, B. B. Gallagher, and B. L. Stamper, "An overview of power spectral density (PSD) calculations," *Proc. SPIE* **5869**, 58690U (2005).

Run Huang obtained her BS (2007) and MS (2009) in optics from Nanjing University of Science and Technology, China. She is currently a PhD candidate at the College of Optical Sciences at the University of Arizona. She is working on high-precision deflectometry system development.

Peng Su received his PhD (2008) degree from the College of Optical Sciences at the University of Arizona. He is currently a research associate professor there. His research focuses on developing advanced technologies for optical testing of large optical components and systems.

Todd Horne is an optomechanical engineer in the optics shop in the College of Optical Sciences at the University of Arizona.

Guido Brusa received his degree in physics in 1989 at the Universita' di Firenze (Italy). Since then he has held several appointments, including research astronomer from 1997 to 2002 at Osservatorio Astrofisico di Arcetri (Florence, Italy) and adaptive optics scientist at Steward Observatory and at the Large Binocular Telescope Observatory (Tucson, Arizona). His field of research is adaptive optics.

Jim H. Burge received his BS in engineering physics from Ohio State University in 1987, and his MS and PhD degrees in optical sciences in 1991 and 1993, from the University of Arizona. His current position is professor at the University of Arizona with joint appointments in optical sciences and astronomy. His interests are astronomical optics, optical fabrication and testing, optomechanics, and optical system engineering.

APPENDIX B: HIGH ACCURACY ASPHERIC X-RAY MIRROR METROLOGY USING SCOTS/DEFLECTOMETRY

Run Huang, Peng Su, James H. Burge, Lei Huang and Mourad Idir

Published in Optical Engineering, August, 2015

Optical Engineering

OpticalEngineering.SPIEDigitalLibrary.org

High-accuracy aspheric x-ray mirror metrology using Software Configurable Optical Test System/ deflectometry

Run Huang
Peng Su
James H. Burge
Lei Huang
Mourad Idir

SPIE.

Optical Engineering 54(8), 084103 (August 2015)

High-accuracy aspheric x-ray mirror metrology using Software Configurable Optical Test System/deflectometry

Run Huang,[a,*] Peng Su,[a] James H. Burge,[a] Lei Huang,[b] and Mourad Idir[b]
[a]University of Arizona, College of Optical Sciences, 1630 East University Boulevard, Tucson, Arizona 85721, United States
[b]Brookhaven National Laboratory, NSLS II 50 Rutherford Drive, Upton, New York 11973-5000, United States

Abstract. The Software Configurable Optical Test System (SCOTS) uses deflectometry to measure surface slopes of general optical shapes without the need for additional null optics. Careful alignment of test geometry and calibration of inherent system error improve the accuracy of SCOTS to a level where it competes with interferometry. We report a SCOTS surface measurement of an off-axis superpolished elliptical x-ray mirror that achieves <1 nm root-mean-square accuracy for the surface measurement with low-order term included. [DOI: 10.1117/1.OE.54.8.084103]

Keywords: optics; metrology; deflectometry; calibration; x-ray optics; interferometry.

Paper 150705P received May 28, 2015; accepted for publication Jul. 1, 2015; published online Aug. 5, 2015.

1 Introduction

Modern synchrotron light sources at hard x-ray, soft x-ray, and extreme ultraviolet wavelengths provide an ideal tool to explore the structure of matter in medical imaging, structure analysis, etc., from millimeter to subnanometer sizes. Transporting the synchrotron light to the sample with a high photon flux and diffraction-limited focus requires ultra-precise x-ray optical elements in the beamline. Single-nanometer spatial resolution in x-ray optics has been theoretically investigated, but the fabrication of the focusing optics is still very challenging.[1] High performance requirements for the x-ray optics push currently available fabrication and metrology technologies to their limits. Any arbitrary optical surfaces could be fabricated in modern computer controlled figuring; however, fabrication of these nano-focusing mirrors relies highly on metrology of the two-dimensional map of the optical surface to serve as a feedback in polishing deterministic processes to correct subtle surface distortion.[2] Thus, the key point for the x-ray optics is the improvement of the metrology. It provides fabrication feedback as well as inspection of optics in the mechanical mount before installing in the beamline.

Interferometry has served as an accurate and noncontact optical metrology in many areas including x-ray optics for a long time. However, it usually requires specifically designed and calibrated null optics[3] when measuring aspheric or freeform optics and has limited dynamic range.[4] Besides interferometry, slope measurements have been widely used to inspect x-ray optics since the 1980s.[5] Instruments like Long Trace Profilers (LTP),[6] Nanometer Optical Component Measuring Machines (NOM),[7] etc., were developed to measure free-form reflective surfaces by measuring the deflection angle along an inspection line. The advantage of these slope measuring instruments is that they do not rely on extra null lenses or computer-generated holograms. By inspecting the deflection angle of a laser beam along an inspection line, the slope of the test optics can be measured directly, and spatial integration can give the topography profile. Slope accuracy of 0.05 μrad has been reported with some of these instruments.[8,9] The metrology technology used to measure x-ray optics in this paper is the Software Configurable Optical Test System (SCOTS), which was developed in the University of Arizona.[10] Similar to LTP/NOM, SCOTS is also a slope measurement technology based on deflectometry.[11] However, it provides a full field of view of the test optics with no scanning or stitching needed. SCOTS has been successfully implemented in the measurements of large astronomy telescopes, such as Giant Magellan Telescope[12] and Large Binocular Telescope.[13]

More recently, we applied this technology to the metrology of a spherical x-ray optics and a superpolished elliptical x-ray mirror.[14,15] In this paper, we present our recent measurement results on the elliptical mirror with more careful measurement calibration controls. This paper extends our previous work by

- presenting detailed experiment procedures, including test model setup, test alignment, distortion correction, and calibration with a reference flat,
- calculating the absolute shape of the elliptical mirror and evaluating the uncertainty by fitting the source distance p, focus distance q, and incident angle Θ of the mirror, and
- discussing sensitivity of reference calibration using generalized expressions.

The paper is organized as follows. In Sec. 2, the principle of the SCOTS test is given. In Sec. 3, metrology results on the x-ray mirror using SCOTS are given with a detailed discussion about system alignment and calibration. Further discussion on reference surface calibration is given in Sec. 4. Summary and perspectives are discussed in Sec. 5.

*Address all correspondence to: Run Huang, E-mail: rhuang@optics.arizona.edu

0091-3286 /2015/$25.00

2 Measurement Principle

SCOTS is a deflectometric method using a simple setup to measure the surface slope using triangulations. Figure 1(a) shows the schematic setup of a SCOTS test. Both the camera and LCD screen are placed near the center of curvature of the test mirror. A certain pixel on the LCD screen illuminates the test mirror; a corresponding bright region shows up on the detector image plane where the mirror image is formed. The illuminating screen pixel, reflection region on the mirror, and camera aperture center uniquely define an incident ray and its reflected ray. Using the coordinate of these three points, the local surface slope of the test mirror can then be calculated. Integration[16] of the slope gives the surface map of the optics under test. To register the illumination screen pixel and the corresponding mirror pixel, line scanning and phase-shifting methods are implemented. A detailed discussion about these two methods is presented in Ref. 10.

When testing a polished optical surface, we are interested in the surface departure of the test surface from its ideal shape. We achieve this by setting up a ray trace model using Zemax with the test optics in its ideal shape and calculating the slope difference between measurement data and Zemax model. The two direction slope maps are integrated into the surface departure map. Since SCOTS works like a Hartmann test with the light path in reverse, the ray trace model in Zemax is quite similar to a Hartmann test,[17] as shown in Fig. 1(b). The camera is modeled as a point source sending the light to the test surface, and the LCD screen is modeled as the image plane to capture the reflected light. Utilizing the Zemax ray tracing function to sample the mirror aperture and trace those individual rays, an ideal spot distribution on the image plane can be obtained (x_{ideal} and y_{ideal}), while in the experiment, this spot distribution (x_{measured} and y_{measured}) is calculated from line scanning or the phase-shifting method. Based on transverse ray aberration model, system wavefront aberrations are approximately equal to the transverse ray aberration by dividing the spot coordinate differences (Δx_{screen} and Δy_{screen}) with the measured mirror-to-screen distance (d_{m2screen})[15] as expressed in Eq. (1). The surface slopes are then obtained by half the wavefront aberrations. Subtraction of the slopes between experimental raw data and the Zemax model gives the surface departure of test optics directly with surface integration. In other words, the Zemax model makes the SCOTS test a virtual null test.

$$\frac{\partial W(x,y)}{\partial x} \cong -\frac{\Delta x_{\text{screen}}}{d_{\text{m2screen}}}, \qquad \frac{\partial W(x,y)}{\partial y} \cong -\frac{\Delta y_{\text{screen}}}{d_{\text{m2screen}}}, \tag{1}$$

$$\Delta x_{\text{screen}} = x_{\text{measured}} - x_{\text{ideal}}, \qquad \Delta y_{\text{screen}} = y_{\text{measured}} - y_{\text{ideal}}, \tag{2}$$

where $W(x,y)$ is wavefront aberration and d_{m2screen} is the distance from the mirror to the LCD screen.

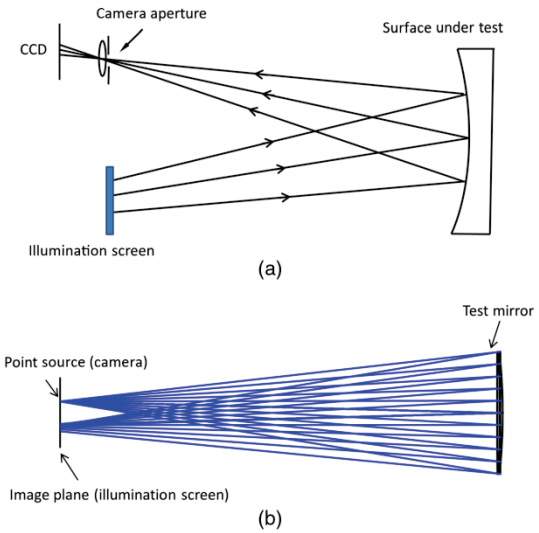

Fig. 1 (a) Schematic setup of a Software Configurable Optical Test System (SCOTS) test and (b) reversed model of a SCOTS test in Zemax.

3 SCOTS Test for Superpolished Aspheric X-Ray Optics

The measured off-axis elliptical x-ray mirror is 100 mm long and 50 mm wide with a working area of 90 mm × 8 mm. The local radius of curvature of the mirror is ~260 m with a maximum surface sag around 4.5 μm. The overall shape error in the useful area of the mirror is <1 nm root-mean-square (RMS) (based on the inspection report from the manufacturer). A detailed SCOTS system setup, geometry control, and calibration procedures are discussed in the following parts.

3.1 *System Setup and Geometry Control*

The actual SCOTS test setup is shown in Fig. 2(a). The illumination screen, set up 2.7 m away from the mirror, is a 19 in. LCD display chosen to give enough illumination area for this 100 mm long elliptical mirror. The camera, which is composed of a 1/3 in. CCD sensor and a commercial camera lens of 50 mm focal length, was set up right next to the LCD screen to capture the reflected screen image. The camera is focused on the mirror surface and samples the working mirror area with ~400 by 40 pixels. Sinusoidal fringes in the x and y directions were displayed on the LCD screen and phase-shifting algorithms were used to correlate the mirror pixel coordinates with the screen pixel coordinates. The slope of each mirror pixel can then be calculated by transverse ray aberration model, as discussed in Sec. 2.

The elliptical mirror was modeled as a biconic surface in Zemax. The mirror was flat in one direction and off-axis aspheric (ellipsoid) in the other direction. The aspheric surface was defined by the parent radius of curvature R and conic constant k, which were calculated from the nominal value of the object distance p, image distance q, and incident angle Θ using Eqs. (3)–(5) in Refs. 18 and 19. The definitions of those parameters are illustrated in Fig. 3. A coordinate break pair was used to decenter and tilt the aspheric surface to get the correct off-axis segment with its local surface normal aligned with global z axis. The amount of decenter was optimized by constraining the real ray y coordinate (REAY) at the mirror surface equal to the off-axis distance [calculated by Eq. (6)] in the merit function. The tilt

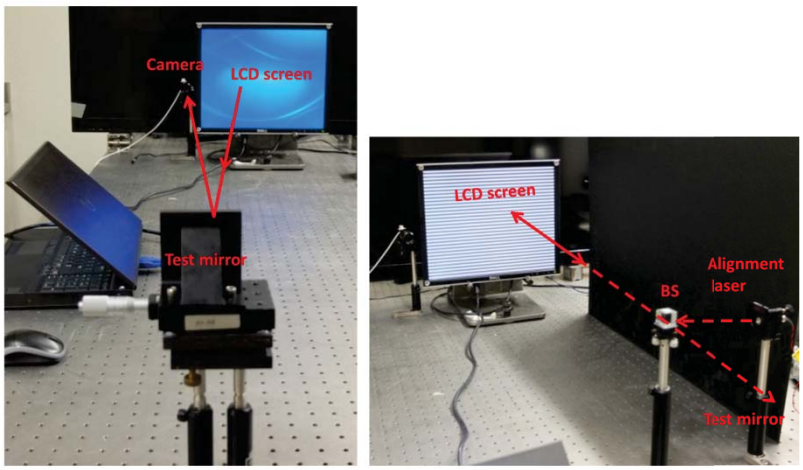

Fig. 2 (a) Experiment SCOTS setup and (b) geometry control with an alignment laser.

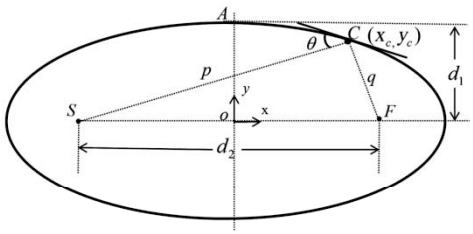

Fig. 3 Model of an ellipse for imaging a point source (S) into a focus (F) with incident angle Θ. p is the object distance and q is the image distance.

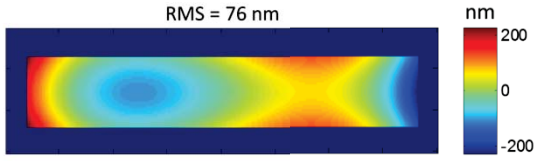

Fig. 4 76 nm RMS wavefront (power removed) that needs to be correctly measured when testing the elliptical mirror.

was optimized by constraining the real ray angle of incidence (RAID) on the mirror surface to be zero. The z position of the coordinate break pair was optimized by fixing the distance between the test optics and camera (screen) (OPTH) equal to the measured value in the test.

$$d_1 = \sqrt{pq} * \sin(\theta) \quad d_2 = \sqrt{p^2 + q^2 + 2pq\ \cos(2\theta)}. \tag{3}$$

Conic constant

$$k = \left(\frac{d_2}{2d_1}\right)^2. \tag{4}$$

Parent radius of curvature (parent axis along OA)

$$R_{\mathrm{OA}} = d_1(k+1). \tag{5}$$

Off-axis distance

$$x_c = \frac{(p^2 - q^2)}{2d_2}. \tag{6}$$

Although the measurement shares a test geometry similar to that described in Ref 15 for measuring a long radius of curvature spherical x-ray mirror, due to the aspherical shape of this elliptical mirror, SCOTS would measure a 76 nm RMS (power removed) wavefront (as shown in Fig. 4) in the test geometry, which is almost zero (10^{-3} nm RMS) for the spherical mirror. Since SCOTS builds the test geometry in Zemax to virtually null the measured wavefront, to accurately measure all the surface shapes even including astigmatism, which is always a difficulty in general SCOTS tests, it requires us to have much more accurate knowledge of the test geometry, i.e., the respective locations of the camera, the screen, and the mirror to correctly null the 76 nm RMS wavefront in the software when measuring the elliptical mirror.

Calibrations of the camera position and screen pixel position have been done in our group by high-precision metrology instruments, such as laser tracker, point source microscope, and coordinate measurement machine, to a few micrometers accuracy. For measuring some large astronomical telescope mirrors during the fabrication process, the mirror position can usually be measured by clamping spherically mounted retro-reflectors (SMRs) on the edge of the mirror and using A laser tracker to measure the SMRs' positions. However, the surface of this superpolished x-ray mirror cannot be touched with SMRs or any other indicators to avoid scratching or contamination. Therefore, the mirror position in this test was measured by a noncontact distance meter with ~1 mm accuracy. To avoid the use of indicators in the previous test, a collimated laser beam and a beamsplitter,

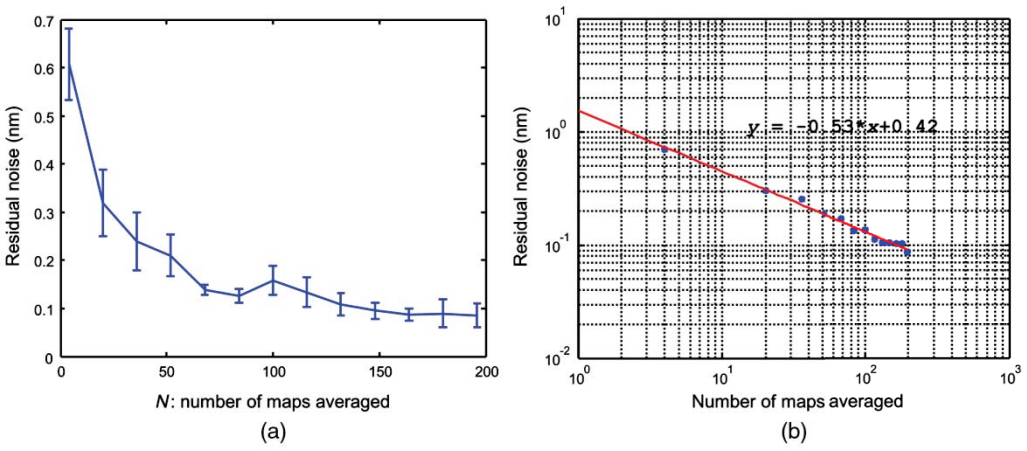

Fig. 5 Estimated residual noise in average of N maps in (a) normal scale and (b) log-log plot.

as shown in Fig. 2(b), were added into the system to help to align the test mirror parallel to the surface of the illumination screen within a 0.9-mrad accuracy. Furthermore, the test uses a high-quality flat to calibrate system error, which includes error from test geometry. The flat calibration helps to reduce the test sensitivity on geometry and a detailed discussion is presented in Sec. 3.4

3.2 *Noise Estimation*

Averaging measurements were conducted to reduce the noise in the measurement, which was probably induced by the stability of mechanical mounts, quality of the illumination screen as well as thermal expansion, detector noise, etc. The residual error in the average map was estimated using the method mentioned in Ref. 20. 600 measurements were taken and N maps were chosen at random and averaged. The comparison of $(\overline{W_N})$ and the total averaged map $(\overline{W_{600}})$ is plotted in Fig. 5. In Fig. 5(b), the fitted line has a slope of -0.53, indicating the dominated noise is random noise, which drops approximately as $1/\sqrt{N}$. From Fig. 5, the error in the final surface map is <0.1 nm RMS with 200 averages. Therefore, we chose 200 averages in the test to achieve a subnanometer low noise measurement.

3.3 *In Situ Camera Distortion Calibration*

Since SCOTS uses three-point (camera position, screen pixel, and mirror pixel) triangulation to calculate the surface slope, the registration between mirror pixel and screen pixel is very important and needs to be addressed with careful camera distortion and perspective correction. In this section, the calibration procedures are described and simulation results are shown.

In the measurement, after taking the phase-shifting measurement, the test x-ray mirror was removed and a mini LCD screen displaying a dots pattern was aligned into the system exactly at the test mirror position, as shown in Fig. 6. The position of the mini LCD screen was precisely controlled by using a Keyence laser displacement sensor with a 1 μm distance accuracy, and the tip/tilt was controlled by monitoring the spot of the reflected alignment laser within a 10 μrad accuracy.

We used a set of orthogonal vector polynomials[21,22] to fit the mapping between the ideal dots positions, which represent the local samplings on the test mirror, and the camera-captured dots positions. The diameter of each dot displayed on the mini LCD screen was chosen such that each dot image can fill 6 pixels on the camera CCD to avoid distortion bias to be introduced into centroiding.[23] The polynomial coefficients were then used to correct the camera distortion and perspective in the phase maps. Different from traditional camera distortion calibration in photogrammetry, this *in situ* camera calibration takes only one image and calibrates the camera distortion (intrinsic) and perspective (extrinsic) at the same time. It avoids the adverse effects from camera instability and uncertainty in the estimation of external parameters in the bundle adjustment algorithms

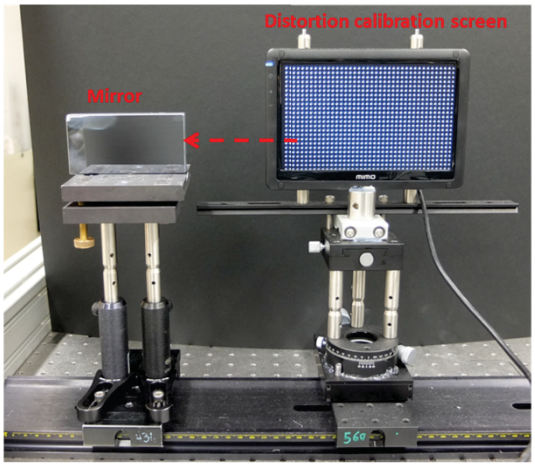

Fig. 6 (a) Experiment setup of camera mapping correction using an LCD screen with dots pattern.

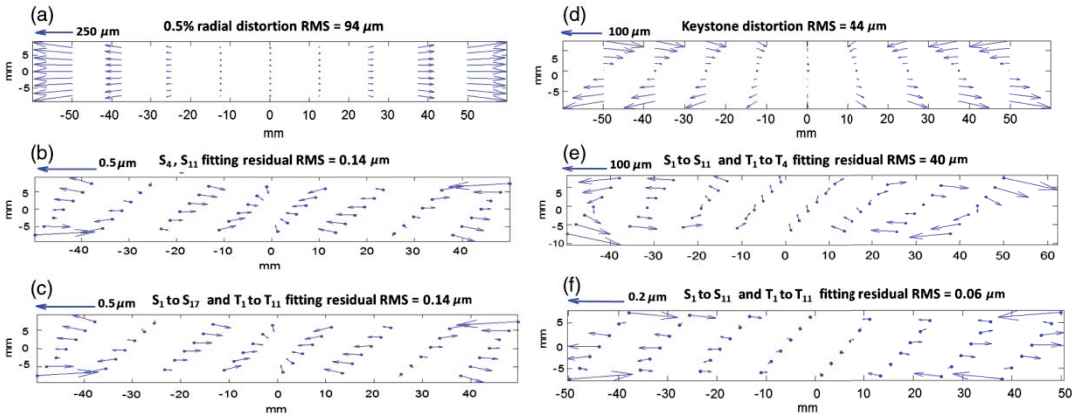

Fig. 7 (a) Vector plot of 0.5% radial distortion at the edge of the mirror image, (b) use of S4 and S11 to fit radial distortion with fitting residual of 0.14 μm RMS, (c) use of S1 to S17 and T1 to T11 to fit radial distortion with fitting residual of 0.14 μm RMS, (d) vector plot of 2.6 mrad keystone projection, (e) use of S1 to S17 and T1 to T4 to fit keystone projection with fitting residual of 40 μm RMS, and (f) use of S1 to S17 and T1 to T11 to fit keystone projection, fitting residual decreases to 0.06 μm RMS.

commonly used in photogrammetry. However, the drawback is camera intrinsic distortion and extrinsic perspective parameters are not separable in the fitting coefficients; and the calibration needs to be performed every time if the camera perspective changes between the measurements.

The vector polynomials are divided into two types of fields, which are S polynomials (irrotational vector field with zero curl) and T polynomials (solenoidal vector field with zero divergence). Simulations were performed to evaluate the effectiveness of correcting camera distortion and perspective using the vector polynomials.

From the simulation, 0.5% camera radial distortion (third order) on the mirror working area can cause 25 μrad RMS slope errors, which corresponds to 57 nm RMS surface measurement errors (mainly spherical aberration). We can use S_4 and S_{11} to model the radial distortion with 0.14 μm RMS fitting residual as shown in Fig. 7(b). The residual error may propagate to the surface measurement and result in 0.045 μrad RMS and 0.3 nm RMS residuals in the slope and surface map, respectively. For most of the measurements, the subnanometer residual in the surface map can be ignored. Since typical camera radial distortion is dominated by low-order deviation (third and fifth), including higher-order polynomial fitting (for example, 17 S terms and 11 T terms) cannot further improve the fitting result as shown in Fig. 7(c).

Camera perspective effect can be modeled as keystone distortion. Simulation shows that to correct the keystone effect, higher-order polynomial terms should be used. For 44 μm RMS keystone distortion (2.6 mrad tilt) in one direction, the large fitting residual (40 μm RMS) in Fig. 7(e) shows that only 11 S terms and 4 T terms cannot model the keystone distortion very well. After increasing the fitting terms, up to 11 S terms and 11 T terms, the fitting residual is down to 0.06 μm RMS. The propagation of the 0.06 μm RMS fitting residual causes 0.016 μrad RMS slope error and 0.003 nm RMS surface error, which can also be ignored.

It is possible to get lower fitting residuals by using more polynomial terms in the fitting process; however, the use of higher-order polynomials might introduce artificial high-order spatial components into the measurement. Therefore, in practical measurements, it is better to align the camera with normal pointing[24] so that there is less keystone effect and we can use fewer polynomial terms to fit mapping coefficients. For most of the practical measurements, we used first 11 S terms and 11 T terms (S1~S11, and T1~T11), to fit the mapping coefficients.

3.4 *System Calibration with a Reference Surface*

Surface irregularity of the elliptical mirror measured by SCOTS after calibration of camera distortion is given in Fig. 8(a), where the surface RMS is 1.3 nm. From the manufacture's report, the elliptical mirror has better than 0.3 nm

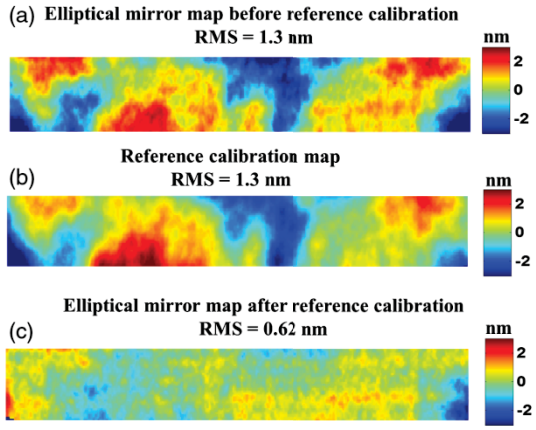

Fig. 8 (a) Measured surface irregularity of the elliptical mirror before reference calibration applied, RMS = 1.3 nm; (b) averaged calibration map with translation of reference flat, RMS = 1.3 nm; and (c) surface map of elliptical mirror with calibration of reference applied, RMS = 0.62 nm.

RMS surface error, which indicates there is a 1 to 2 nm RMS systematic error in the surface map. Further calibration to cancel out the systematic error is needed to improve the test accuracy.

From our analysis, we found that the systematic errors of SCOTS are a function of the camera's field of view,[25] indicating possible effects from camera lens aberrations and other inherent errors, such as ghost image, stray light, screen pixel distortion, etc. Test accuracy can benefit from a calibration to subtract these errors by measuring a high-quality reference surface.[15]

Reference calibration also helps to reduce measurement errors introduced by test geometry uncertainty as long as the shape of the reference surface is not far from the test optics. For this x-ray elliptical mirror, which has a radius of curvature around 260 m and PV sag <5 μm, we applied a reference calibration using a high-quality flat mirror.

Based on the estimated alignment accuracy described in Sec 3.1, we performed a geometry tolerance analysis on the measurement with and without reference calibration. The results are given in Table 1. The coordinates were set up locally at the mirror, where the x direction is along the long side of the mirror, the y direction is along the short side of the mirror, and the z direction is perpendicular to the slope of the mirror center. This SCOTS test is very insensitive to the positioning of the components, except for the relative tilt between the screen and mirror about the y axis. This is understandable since the elliptical mirror under test only has optical power in the x direction. Comparing column 3 and column 2 in Table 2, reference calibration greatly reduces geometry sensitivity on elements' tilt. Measurement error due to the 0.9 mrad screen tilt about the y axis is only ~0.05 nm RMS if we apply reference calibration, which is 10 times smaller than the test without the reference calibration. Measurement error due to camera lateral shift cannot be compensated by the reference calibration since it only causes a constant shift of the measured screen coordinate and is removed in the data reduction as a piston term. With the geometry controls mentioned in Sec 3.1 and reference calibration, measurement error introduced by the geometry uncertainty can be limited to subnanometers on this SCOTS test setup.

Table 1 Geometry tolerance of Software Configurable Optical Test System (SCOTS) test for ellipse x-ray mirror.

	Measurement uncertainty with power removed (nm RMS)	
System geometry uncertainty	Without flat calibration	With flat calibration
1 mm camera x position uncertainty	0.02	0.02
1 mm camera y position uncertainty	0.002	0.002
1 mm camera z position uncertainty	0	0
0.9 mrad screen tilt about x axis	0.01	0
0.9 mrad screen tilt about y axis	0.54	0.05
1 mm screen z position uncertainty	0	0

Table 2 SCOTS measured x-ray mirror parameters (p, q, Θ).

	p (mm)	q (mm)	Θ (mrad)
Nominal value	93,595	355	2.7
SCOTS measured	93,595	359.914	2.77

Although system error in SCOTS can be greatly reduced by reference calibration, directly subtracting a single measurement of the flat mirror could introduce the surface error of the reference surface itself into the measurement. The reference surface usually has better surface quality than the test optics so that the error from the reference surface can be ignored. However, when the test optics has a similar surface quality as the reference surface, it becomes necessary to compensate the surface error from the reference surface to improve measurement accuracy. Inspired by the random ball test[20,26] in phase-shifting interferometry, we translated the reference flat randomly and a series of random patches on the reference flat surface was measured with SCOTS and averaged. In the averaged map, the imperfection from the reference surface was averaged out leaving only the fixed systematic error from SCOTS system. In our test, a high-precision flat mirror, which has ~1.6 nm RMS surface errors over 260 mm × 9 mm working area, was used as a reference surface. The flat was carefully aligned at the test mirror position, following the same procedures described in Sec 3.3 with 1 μm accuracy in distance and 10 μrad in tip/tilt. A total of eight maps were taken and averaged. Figure 8(b) is the averaged map of the flat measured with SCOTS after performing the random test discussed above.

For an ideal random test, the measurement patches on the reference flat surface would be uncorrelated and independent, and therefore, RMS error from reference surface drops as $1/\sqrt{N}$, where N is the total number of measurement patches. Therefore, the slope in the log-log plot of measured surface RMS as a function of number of measurements is -0.5. To check the residual error from the reference surface in the average map, we evaluated the slope of the measurement data using the same method described in Sec 3.2. N maps ($N = 1, 2, 3, 4$) were randomly selected and averaged. After subtracting the averaged map, the fitted slope of the residual RMS in log scale is ~ -0.7, indicating certain correlation exists between the eight maps, and therefore, some residual error from reference surface stays in the averaged map in Fig. 8(b). A small shear step between each measurement, which is limited by the relative size of the test surface and reference surface, might be the major cause that reduces the effectiveness of the random test. In practical measurement, it is always good to have a large shear of the reference flat to reduce the correlation between different sample patches. Rotation of the reference flat can also help to increase test efficiency.

It is clear by comparing Figs. 8(a) and 8(b) that the measurements are dominated by systematic errors. As shown in Fig. 8(c), after subtracting the reference calibration [Fig. 8(b)] from the uncalibrated map [Fig. 8(a)], the major systematic error was removed and the measured surface RMS of the elliptical x-ray mirror was reduced to 0.62 nm. Through the above analysis, we expect using a larger reference surface

and averaging more maps with larger shear steps can help to further improve the measurement result.

3.5 *Absolute Shape of the Elliptical Mirror*

With reference flat calibration, not only the subtle surface departure of the elliptical mirror from ideal shape was measured (0.62 nm surface RMS), but also the primary shape (average radius of curvature) of the elliptical mirror was retrieved by evaluating the surface power departure from the flat. A series of repeated tests show that the fitted radius of best fit sphere from the SCOTS test is ~259.05 m. Compared with the result from the Zemax model, which is 261.25 m, there is ~50 nm P-V measurement uncertainty in surface sag over the 90 mm aperture. The effect of this power uncertainty was evaluated by fitting the parameters of the elliptical mirror, i.e., source distance p, focus distance q, and incident angle Θ. The fitting results are given in Table 2. Fixing p equal to 93,595 mm (designed value), the fitted q and Θ are found to be 359.914 mm and 2.77 mrad, respectively, with ~0.018 nm RMS in residual surface height. Compared with the designed value of this elliptical mirror, the 4.914 mm increase in focus distance will enlarge the focus size by 1.38%, since $\text{focus}_{\text{size}} \approx \text{source}_{\text{size}} \times q/p$.

4 Further Discussion on Reference Calibration

We mentioned in Sec. 3.4 that reference calibration can help to increase the test accuracy by cancelling inherent system error and test geometry error. The validation of this calibration procedure requires that the reference surface shape does not have a large departure from the test optics so that they share a similar light path in the measurement. Through a ray trace simulation in Zemax, Table 1 in Sec. 3.4 gives the improved measurement sensitivity of this x-ray mirror by using a flat calibration. Equations are derived in this section for a fundamental understanding of the geometry sensitivity improvement using reference calibration.

For simplicity and easy illustration, the discussion below assumes off-axis test geometry where the camera and display are configured with a certain amount of lateral separation and near-paraxial conjugate position of the test mirror (for most cases of SCOTS tests). The analysis also simplifies the test optics as a spherical surface with radius of curvature R.

As described in Sec. 2, the spot distribution on the display can be calculated using a reverse ray trace model in Zemax, where the camera is modeled as a point source sending the light on to the mirror and reflecting back to the display plane. With this model, for near-paraxial conjugate configuration, SCOTS test can be treated as an imaging system and the spot distribution on the display can be approximated as transverse ray aberration. In the following discussion, we only included defocus and two primary off-axis aberrations, which are astigmatism and coma.

For an optical system with a circular exit pupil of radius r, it is convenient to use normalized coordinate (ρ, θ), where $0 \le \rho \le 1$ and $0 \le \theta \le 2\pi$; in the following discussion, we convert (ρ, θ) coordinate to normalized Cartesian coordinates (x_p, y_p), where $(x_p, y_p) = \rho(\sin\theta, \cos\theta)$. For defocus, astigmatism, and coma, the wavefront aberration is in the form of

$$W(x_p, y_p) = W_{020}(x_p^2 + y_p^2) + W_{222}y_p^2 + W_{131}(x_p^2 + y_p^2)y_p, \tag{7}$$

where W_{020}, W_{222}, and W_{131} are the aberration coefficients of defocus, astigmatism, and coma representing the peak values of the aberrations.[27]

The spot diagram on the display can be approximated as transverse ray aberration.[28]

$$\varepsilon_y(x_p, y_p) \approx -2f_{\#}\frac{\partial W(x_p, y_p)}{\partial y_p}, \tag{8}$$

$$\varepsilon_x(x_p, y_p) \approx -2f_{\#}\frac{\partial W(x_p, y_p)}{\partial x_p}, \tag{9}$$

where $f_{\#}$ is the f-number of the image-forming light cone.

For test configuration in Fig. 9, object distance $d_{\text{m2camera}} = d_{\text{m2screen}} = d$, where $d \neq R$; usually, the dominated spot spread on the LCD display is the result of defocus; W_{020} is related to the amount of focus shift δ_z (Refs. 27 and 28) and can be expressed as

$$W_{020} = \frac{1}{8f_{\#}^2}\delta_z = \frac{r^2(R-d)}{d(R-2d)}. \tag{10}$$

Off-axis test configuration introduces camera lateral position (h) dependent aberrations in the measured wavefront, which are usually dominated by astigmatism and coma. For paraxial conjugation, by using Seidel sums,[29] we get Seidel coefficients of W_{222} and W_{131}:

$$W_{222} = \frac{h^2r^2}{Rd^2}, \tag{11}$$

$$W_{131} = \frac{hr^3(d-R)}{R^2d^2}, \tag{12}$$

where r is the radius of the test optics; h is the lateral position of the camera.

Test sensitivity on geometry with and without reference calibration can then be derived from the above equations. In this paper, we derive the sensitivity on camera lateral position h and display tilt as two examples.

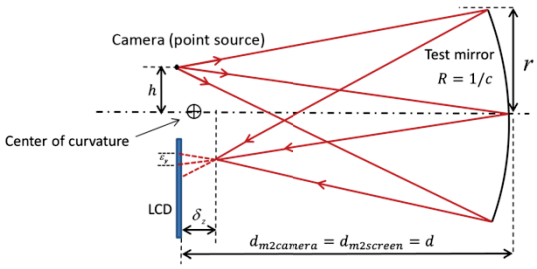

Fig. 9 Reverse ray tracing model is used for SCOTS measurement sensitivity analysis.

From Eqs. (8)–(12), we can see that the spot diagram on the LCD display due to test geometry introduced defocus W_{020} is independent of camera lateral position h; therefore, by applying reference calibration, the improvement of test sensitivity on camera lateral position h is only related with camera lateral position dependent aberrations, which are astigmatism, and coma.

Without reference calibration, the sensitivity of astigmatism W_{222} and coma W_{131} to camera lateral position h are given in Eqs. (13) and (14), which are the partial derivatives of Eqs. (11) and (12) with respect to h:

$$\frac{\partial W_{222}}{\partial h} = \frac{2hr^2}{Rd^2}, \tag{13}$$

$$\frac{\partial W_{131}}{\partial h} = \frac{r^3(d-R)}{R^2d^2}. \tag{14}$$

Calibrating the test by measuring a reference surface at the same test configuration but with a slightly different radius of curvature (small ΔR), the sensitivities of astigmatism W_{222} and coma W_{131} to camera lateral position h are reduced to

$$\frac{\partial W_{222}}{\partial h} = \frac{2hr^2}{R^2d^2}\Delta R, \tag{15}$$

$$\frac{\partial W_{131}}{\partial h} = \frac{r^3(R-2d)}{R^3d^2}\Delta R. \tag{16}$$

In the case of testing an x-ray mirror, the calibration reference is a flat, whose wavefront does not have any off-axis aberrations. It cannot help to reduce sensitivity on those off-axis aberrations, therefore, in Table 1, there is no improvement of test sensitivity on camera lateral position.

For the test sensitivity on display tilt, we assume one directional display tilt θ about the x direction as shown in Fig. 10. For a ray coming from a specific mirror pupil coordinate (x_p, y_p), the slope error of that ray is

$$\Delta S_y(x_p,y_p) = \frac{\varepsilon_y - \varepsilon_y'}{d_{\text{m2screen}}} = \frac{\varepsilon_y\left\{1 - \frac{\cos\gamma_{(x_p,y_p)}}{\cos[\gamma_{(x_p,y_p)}+\theta]}\right\}}{d_{\text{m2screen}}}, \tag{17}$$

$$\Delta S_x(x_p,y_p) = \frac{\varepsilon_x - \varepsilon_x'}{d_{\text{m2screen}}} = \frac{\varepsilon_x - \varepsilon_y' \cdot \sin\theta \cdot \tan\beta_{(x_p,y_p)}}{d_{\text{m2screen}}}, \tag{18}$$

where γ and β are the angles of the incident ray from the mirror pupil (x_p,y_p) on the display in the yoz and xoz planes.

Let us take y slope sensitivity as an example. For defocus dominated test configuration, without reference calibration, the sensitivity on the display tilt is obtained by calculating ε_y due to defocus W_{020} using Eqs. (8) and (10), and substituting ε_y into Eq. (17).

$$\Delta S_y \approx \frac{2(R-d)r_p y_p}{R} \cdot \left[1 - \frac{\cos\gamma}{\cos(\gamma+\theta)}\right] \cdot \frac{1}{d}. \tag{19}$$

With reference calibration, assuming the differences of γ and β are negligible between the test mirror and calibration reference (ΔR is small), the measurement error is reduced to

$$\Delta S_y \approx \frac{2dr_p y_p \Delta R}{R^2} \cdot \left[1 - \frac{\cos\gamma}{\cos(\gamma+\theta)}\right] \cdot \frac{1}{d}. \tag{20}$$

Equations (19) and (20) show that reference calibration helps reduce ΔS_y by a factor of $[R(R-d)]/\Delta R d$.

The above analysis is applied to the SCOTS test of this x-ray mirror with some approximations. The mirror is flat in the y direction and has a very large radius of curvature along the x direction. By assuming the mirror is spherical in the x direction using its best fit sphere and ignoring the small off-axis geometry effect, the spot diagram in the x direction can be estimated as

$$\varepsilon_x = \varepsilon_{x(\text{mirror})} = \frac{2(R-d)r_p x_p}{R}, \tag{21}$$

where R is the radius of the best fit sphere (~260 m), and d ($d \sim 2.7$ m) is the distance from the mirror to the display.

Once calibrating with a flat, the spot diagram in the x direction is

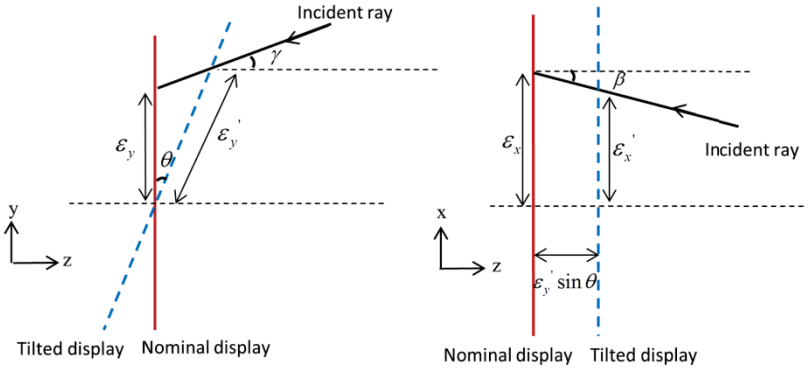

Fig. 10 Display tilt about x direction. Solid red line represents display at nominal position, and dash blue line represents tilted display plane.

$$\varepsilon_x = \varepsilon_{x(\text{mirror})} - \varepsilon_{x(\text{flat})} = \frac{2(R-d)r_p x_p}{R} - 2r_p x_p = \frac{-2dr_p x_p}{R}. \quad (22)$$

Ignoring the differences of γ and β between the x-ray mirror and calibration flat, the estimated improvement of x slope sensitivity on the display tilt about the y direction by using flat calibration is $(R-d)/d$, which is ~90 times and it is at the same level as the Zemax ray tracing result.

The above analysis uses wavefront aberration theories to derive parametric expressions of sensitivity improvement by using a reference calibration. The calculation uses Seidel coefficients to calculate the spot diagram on the display due to astigmatism and coma, which assumes paraxial conjugate of the camera and display about the test mirror. The calculated spot distribution can hold a good accuracy if the camera and the display are not far away from the conjugate position of a spherical test mirror. To get the exact spot distribution on the display, a rigorous ray trace should be performed when the surface is far away from spherical or defocus effect gets larger. However, one can still use the sensitivity equations above to get a quick and good estimation of the improvement when selecting the reference surface in the design of the test.

5 Summary

We advanced SCOTS measurement of aspheric x-ray optics to subnanometer (RMS) surface accuracy with precise alignment control and calibration. This is a promising, non-null, noncontact, high dynamic range, and full-field test to achieve comparable accuracy with interferometry testing. The calibration procedures of SCOTS have been researched and experimentally proved in this test. However, depending on different applications, the calibration procedures are not limited to those described in this work. A reference calibration is very useful in calibrating the SCOTS systematic error. However, the quality of the reference will influence the test result significantly when the test optics has equivalent or even better quality. A random test of the reference surface was carried out in this paper to reduce the error from the calibration reference. Generalized sensitivity of the reference calibration is also discussed in Sec. 4. Further work on system calibration is in progress. Future work will evaluate the effect of camera lens aberration in order to guide the selection of the camera lens, as well as the analysis of measurement results. We will explore these aspects and report in future papers.

Acknowledgments

This work was supported by the U.S. Department of Energy, Office of Science, Office of Basic Energy Sciences, under Contract No. DE-AC-02-98CH10886.

References

1. H. Mimura et al., "Breaking the 10 nm barrier in hard-x-ray focusing," *Nat. Phys.* **1457**, 1–4 (2009).
2. M. Idir et al., "Current status of the NSLS-II optical metrology laboratory," *Nucl. Instrum. Methods Phys. Res. A* **710**, 17–23 (2013).
3. W. Cai et al., "The diffractive optics calibrator: measurement of etching variations for binary computer generated holograms," *Appl. Opt.* **53**(11), 2477–2486 (2014).
4. C. Faber et al., "Deflectometry challenges interferometry: the competition gets tougher!," *Proc. SPIE* **8493**, 84930R (2012).
5. P. Z. Takacs, S. N. Qian, and J. Colbert, "Design of a long trace surface profiler," *Proc. SPIE* **749**, 59–64 (1987).
6. H. Li, P.Z. Takacs, and T. Oversluizen, "Vertical scanning long trace profiler: a tool for metrology of x-ray mirrors," *Proc. SPIE* **3152**, 180–187 (1997).
7. F. Siewert, H. Lammert, and T. Zeschke, "The nanometer optical component measuring machine," in *Modern Developments in X-Ray and Neutron Optics*, A. Erko et al., Eds., Vol. 137, pp. 193–200, Springer, Berlin, Heidelberg (2008).
8. F. Siewert et al., "Ultra-precise characterization of LCLS hard x-ray focusing mirrors by high resolution slope measuring deflectometry," *Opt. Express* **20**, 4525–4536 (2012).
9. Y. Senba et al., "Upgrade of long trace profiler for characterization of high-precision x-ray mirrors at SPring-8," *Nucl. Instrum. Methods Phys. Res. A* **616**, 237–240 (2010).
10. P. Su et al., "Software configurable optical test system: a computerized reverse Hartmann test," *Appl. Opt.* **49**(23), 4404–4412 (2010).
11. M. Knauer, J. Kaminski, and G. Hausler, "Phase measuring deflectometry: a new approach to measure specular free form surfaces," *Proc. SPIE* **5457**, 366–376 (2004).
12. P. Su et al., "SCOTS: a reverse Hartmann test with high dynamic range for Giant Magellan Telescope primary mirror segments," *Proc. SPIE* **8450**, 84500W (2012).
13. R. Huang et al., "Measurement of a large deformable aspherical mirror using SCOTS (Software Configurable Optical Test System)," *Proc. SPIE* **8838**, 883807 (2013).
14. R. Huang et al., "X-ray mirror metrology using SCOTS/deflectometry," *Proc. SPIE* **8848**, 88480G (2013).
15. P. Su et al., "Non-null full field x-ray mirror metrology using SCOTS: a reflection deflectometry approach," *Opt. Express* **20**, 12393–12407 (2012).
16. W. H. Southwell, "Wave-front estimation from wave-front slope measurements," *J. Opt. Soc. Am.* **70**(8), 998 (1980).
17. D. Malacara-Doblado and I. Ghozeil, "Hartmann, Hartmann-Shack, and other screen tests," in *Optical Shop Testing*, 3rd ed., D. Malacara, Ed., pp. 361–397, Wiley Series in Pure and Applied Optics, Wiley, New Jersey (2007).
18. J. P. Sutter et al., "Geometrical and wave-optical effects on the performance of a bent-crystal dispersive x-ray spectrometer," *Nucl. Instrum. Methods Phys. Res. A* **621**, 627–636 (2010).
19. J. C. Wyant and K. Creath, "Basic wavefront aberration theory for optical metrology," in *Applied Optics and Optical Engineering*, R. R. Shannon and J. C. Wyant, Eds., Vol. **11**, pp. 48–50, Academic Press, New York (1992).
20. P. Zhou and J. H. Burge, "Limits for interferometer calibration using the random ball test," *Proc. SPIE* **7426**, 74260U (2009).
21. C. Zhao and J. H. Burge, "Orthonormal vector polynomials in a unit circle. Part I: basis set derived from gradients of Zernike polynomials," *Opt. Express* **15**(26), 18014–18024 (2007).
22. C. Zhao and J. H. Burge, "Orthonormal vector polynomials in a unit circle. Part II: completing the basis set," *Opt. Express* **16**(9), 6586–6590 (2008).
23. J. Mallon and P. F. Whelan, "Which pattern? Biasing aspects of planar calibration patterns and detection methods," *Pattern Recognit. Lett.* **28**(8), 921–930 (2007).
24. R. Huang et al., "Optical metrology of a large deformable aspherical mirror using software configurable optical test system," *Opt. Eng.* **53**(8), 085106 (2014).
25. P. Su et al., "Precision aspheric optics testing with SCOTS: a deflectometry approach," *Proc. SPIE* **8788**, 87881E (2013).
26. W. Cai et al., "Interferometer calibration using the random ball test," 2010, http://www.loft.optics.arizona.edu/documents/journal_articles/2010_wenrui_osa_randomball.pdf (3 July 2015).
27. V. Mahajan, *Aberration Theory Made Simple*, SPIE Press, Bellingham, WA (1991).
28. J. E. GreivenKamp, *Field Guide to Geometrical Optics*, SPIE Press, Bellingham, WA (2003).
29. J. Sasián, *Introduction to Aberrations in Optical Imaging Systems*, Cambridge University Press, New York (2013).

Run Huang obtained her BS in 2007 and MS in 2009 in optics from Nanjing University of Science and Technology, China. She is currently a PhD candidate at the College of Optical Sciences in the University of Arizona. She is working on high-precision deflectometry system development.

Peng Su received his PhD in 2008 from the College of Optical Sciences at the University of Arizona. His research focuses on developing advanced technologies for optical testing of large optical components and systems.

James H. Burge received his BS in engineering physics from Ohio State University in 1987 and his MS and PhD degrees in optical sciences in 1991 and 1993 from the University of Arizona. His current

position is professor at the University of Arizona with joint appointments in optical sciences and astronomy, where his interests are astronomical optics, optical fabrication and testing, optomechanics, and optical system engineering.

Lei Huang received his PhD from Nanyang Technological University in 2013. He is currently a research associate at Brookhaven National Laboratory. His research interests include wavelength metrology, wavefront reconstruction, phase measuring deflectometry, phase measuring profilometry, fringe analysis, and phase retrieval.

Mourad Idir graduated in 1994 from Paris Sud University, France. He joined the NSLS II Project in November 2010 after nearly 10 years in Synchrotron SOLEIL in France. Since coming to NSLS II, he has been the group leader of the Optic and Tests Beamline.

APPENDIX C: ZERNIKE STANDARD POLYNOMIALS

mode	polynomial
1	1
2	$\sqrt{4}\rho\cos(\theta)$
3	$\sqrt{4}\rho\sin(\theta)$
4	$\sqrt{3}(2\rho^2-1)$
5	$\sqrt{6}\rho^2\sin(2\theta)$
6	$\sqrt{6}\rho^2\cos(2\theta)$
7	$\sqrt{8}(3\rho^3-2\rho)\sin(\theta)$
8	$\sqrt{8}(3\rho^3-2\rho)\cos(\theta)$
9	$\sqrt{8}\rho^3\sin(3\theta)$
10	$\sqrt{8}\rho^3\cos(3\theta)$
11	$\sqrt{5}(6\rho^4-6\rho^2+1)$
12	$\sqrt{10}(4\rho^4-3\rho^2)\cos(2\theta)$
13	$\sqrt{10}(4\rho^4-3\rho^2)\sin(2\theta)$
14	$\sqrt{10}\rho^4\cos(4\theta)$
15	$\sqrt{10}\rho^4\sin(4\theta)$
16	$\sqrt{12}(10\rho^5-12\rho^3+3\rho)\cos(\theta)$
17	$\sqrt{12}(10\rho^5-12\rho^3+3\rho)\sin(\theta)$
18	$\sqrt{12}(5\rho^5-4\rho^3)\cos(3\theta)$
19	$\sqrt{12}(5\rho^5-4\rho^3)\sin(3\theta)$
20	$\sqrt{12}\rho^5\cos(5\theta)$
21	$\sqrt{12}\rho^5\sin(5\theta)$
22	$\sqrt{7}(20\rho^6-30\rho^4+12\rho^2-1)$

REFERENCES

1. J. F. Song and T. V Vorburger, "Stylus profiling at high resolution and low force.," Appl. Opt. **30**, 42–50 (1991).

2. G. Udupa, M. Singaperumal, R. S. Sirohi, and M. P. Kothiyal, "Characterization of surface topography by confocal microscopy: I. Principles and the measurement system," Meas. Sci. Technol. **11**, 305–314 (2000).

3. H.-J. Jordan, M. Wegner, and H. Tiziani, "Highly accurate non-contact characterization of engineering surfaces using confocal microscopy," Meas. Sci. Technol. **9**, 1142–1151 (1998).

4. P. Hariharan, "Optical interferometry," Reports Prog. Phys. **54**, 339–390 (1991).

5. A. F. Fercher, "Computer-generated Holograms for Testing Optical Elements: Error Analysis and Error Compensation," Opt. Acta Int. J. Opt. **23**, 347–365 (1976).

6. W. Cai, P. Zhou, C. Zhao, and J. H. Burge, "Analysis of wavefront errors introduced by encoding computer-generated holograms.," Appl. Opt. **52**, 8324–31 (2013).

7. J. C. Wyant, "White light interferometry," in *AeroSense 2002*, H. J. Caulfield, ed. (International Society for Optics and Photonics, 2002), pp. 98–107.

8. P. Su, R. E. Parks, L. Wang, R. P. Angel, and J. H. Burge, "Software configurable optical test system: a computerized reverse Hartmann test.," Appl. Opt. **49**, 4404–12 (2010).

9. J.Ojeda-Castanede, "Foucault, Wire, and Phase Modulation Tests," in *Optical Shop Testing*, D. Malacara, ed., third (John Wiley & Sons, 2007), pp. 275–313.

10. M. Mansuripur, "The Ronchi test," Opt. & Photonics News **8**, (1997).

11. Cornejo-Rodriguez, "Ronchi Test," in *Optical Shop Testing*, D. Malacara, ed., third (John Wiley & Sons, 2007), pp. 317–350.

12. Daniel and I. G. Malacara, "Hartmann, Hartmann-Shack, and Other Screen Tests," in *Optical Shop Testing*, D. Malacara, ed., third (John Wiley & Sons, 2007), pp. 361–394.

13. B. C. Platt and R. Shack, "History and principles of Shack-Hartmann wavefront sensing.," J. Refract. Surg. **17**, S573–7.

14. D. R. Neal, J. Copland, and D. A. Neal, "Shack-Hartmann wavefront sensor precision and accuracy," in *International Symposium on Optical Science and Technology*, A. Duparr‰ and B. Singh, eds. (International Society for Optics and Photonics, 2002), pp. 148–160.

15. M. C. Knauer, J. Kaminski, and G. Hausler, "Phase measuring deflectometry: a new approach to measure specular free form surfaces," in *Photonics Europe*, W. Osten and M. Takeda, eds. (International Society for Optics and Photonics, 2004), pp. 366–376.

16. P. Su, S. Wang, M. Khreishi, Y. Wang, T. Su, P. Zhou, R. E. Parks, K. Law, M. Rascon, T. Zobrist, H. Martin, and J. H. Burge, "SCOTS: a reverse Hartmann test with high dynamic range for Giant Magellan Telescope primary mirror segments," in *SPIE Astronomical Telescopes + Instrumentation*, R. Navarro, C. R. Cunningham, and E. Prieto, eds. (International Society for Optics and Photonics, 2012), p. 84500W.

17. R. Huang, P. Su, T. Horne, G. Brusa Zappellini, and J. H. Burge, "Measurement of a large deformable aspherical mirror using SCOTS (Software Configurable Optical Test System)," in *SPIE Optical Engineering + Applications*, O. W. Fähnle, R. Williamson, and D. W. Kim, eds. (International Society for Optics and Photonics, 2013), p. 883807.

18. R. Huang, P. Su, T. Horne, G. Brusa, and J. H. Burge, "Optical metrology of a large deformable aspherical mirror using software configurable optical test system," Opt. Eng. **53**, 085106 (2014).

19. R. Huang, P. Su, J. H. Burge, and M. Idir, "X-ray mirror metrology using SCOTS/deflectometry," in *SPIE Optical Engineering + Applications*, A. Khounsary, S. Goto, and C. Morawe, eds. (International Society for Optics and Photonics, 2013), p. 88480G.

20. J. L. Rayces, "Exact Relation between Wave Aberration and Ray Aberration," Opt. Acta Int. J. Opt. **11**, 85–88 (1964).

21. A. Riccardi, M. Xompero, R. Briguglio, F. Quirós-Pacheco, L. Busoni, L. Fini, A. Puglisi, S. Esposito, C. Arcidiacono, E. Pinna, P. Ranfagni, P. Salinari, G. Brusa, R. Demers, R. Biasi, and D. Gallieni, "The adaptive secondary mirror for the Large Binocular Telescope: optical acceptance test and preliminary on-sky commissioning results," in *SPIE Astronomical Telescopes + Instrumentation*, B. L. Ellerbroek, M. Hart, N. Hubin, and P. L. Wizinowich, eds. (International Society for Optics and Photonics, 2010), p. 77362C.

22. Faro, "FARO Laser Tracker - Downloads," http://www.faro.com/products/metrology/faro-laser-tracker/downloads#Download.

23. R. E. Parks and W. P. Kuhn, "Optical alignment using the Point Source Microscope," in *Optics & Photonics 2005*, A. E. Hatheway, ed. (International Society for Optics and Photonics, 2005), p. 58770B–58770B–15.

24. J. E. Greivenkamp, "Field Guide to Geometrical Optics | (2004) | Greivenkamp | Publications | Spie," http://spie.org/Publications/Book/547461.

25. L. Hazra, "Introduction to Aberrations in Optical Imaging Systems by José Sasián," J. Opt. **42**, 293–294 (2013).

26. R. R. Shannon and J. C. Wyant, *Applied Optics and Optical Engineering, Volume XI* (1992).

27. R. N. Youngworth, B. B. Gallagher, and B. L. Stamper, "An overview of power spectral density (PSD) calculations," in *Optics & Photonics 2005*, H. P.

Stahl, ed. (International Society for Optics and Photonics, 2005), p. 58690U–58690U–11.

28. D. W. Kim, C. J. Oh, P. Su, and J. H. Burge, "Advanced Technology Solar Telescope 4.2 m Off-axis Primary Mirror Fabrication," in *Classical Optics 2014* (OSA, 2014), p. OTh2B.3.

29. P. S. Huang, "High-speed 3-D shape measurement based on digital fringe projection," Opt. Eng. **42**, 163 (2003).

30. J. C. Wyant, "Phase shifting Interferometry," http://fp.optics.arizona.edu/jcwyant/Optics513/ChapterNotes/Chapter05/Notes/Phase Shifting Interferometry.nb.pdf.

31. K. Creath, "Comparison Of Phase-Measurement Algorithms," in *30th Annual Technical Symposium*, K. Creath, ed. (International Society for Optics and Photonics, 1987), pp. 19–28.

32. C. Faber, *New Methods and Advances in Deflectometry* (Erlangen Scientific Press, 2012).

33. F. Liu, B. M. Robinson, P. J. Reardon, and J. M. Geary, "Analyzing optics test data on rectangular apertures using 2-D Chebyshev polynomials," Opt. Eng. **50**, 043609 (2011).

34. D. C. Brown, "Close-range camera calibration," Photogramm. Eng. (1971).

35. J. Weng, P. Cohen, and M. Herniou, "Camera calibration with distortion models and accuracy evaluation," IEEE Trans. Pattern Anal. Mach. Intell. **14**, 965–980 (1992).

36. J. Wang, F. Shi, J. Zhang, and Y. Liu, "A new calibration model of camera lens distortion," Pattern Recognit. **41**, 607–615 (2008).

37. C. Zhao and J. H. Burge, "Orthonormal vector polynomials in a unit circle, Part I: basis set derived from gradients of Zernike polynomials," Opt. Express **15**, 18014 (2007).

38. C. Zhao and J. H. Burge, "Orthonormal vector polynomials in a unit circle, Part II : completing the basis set," Opt. Express **16**, 6586 (2008).

39. J. Mallon and P. F. Whelan, "Which pattern? Biasing aspects of planar calibration patterns and detection methods," Pattern Recognit. Lett. **28**, 921–930 (2007).

40. T. Bothe, W. Li, M. Schulte, C. von Kopylow, R. B. Bergmann, and W. P. O. Jüptner, "Vision ray calibration for the quantitative geometric description of general imaging and projection optics in metrology.," Appl. Opt. **49**, 5851–60 (2010).

41. W. Zhao, R. Huang, P. Su, and J. H. Burge, "Aligning and testing non-null optical system with deflectometry," in *SPIE Optical Engineering + Applications*, J. Sasián and R. N. Youngworth, eds. (International Society for Optics and Photonics, 2014), p. 91950F.

42. "MATLAB - The Language of Technical Computing," http://www.mathworks.com/products/matlab/.

43. J. W. Goodman, *Introduction To Fourier Optics 3Rd Edition* (Viva Books Private Limited, 2007).

44. J. B. Breckinridge and D. G. Voelz, *Computational Fourier Optics: A MATLAB Tutorial* (Society of Photo Optical, 2011).

45. T. Su, A. Maldonado, P. Su, and J. H. Burge, "Instrument transfer function of slope measuring deflectometry systems.," Appl. Opt. **54**, 2981–90 (2015).

46. P. Su, M. A. H. Khreishi, T. Su, R. Huang, M. Z. Dominguez, A. Maldonado, G. Butel, Y. Wang, R. E. Parks, and J. H. Burge, "Aspheric and freeform surfaces metrology with software configurable optical test system: a computerized reverse Hartmann test," Opt. Eng. **53**, 031305 (2013).

47. P. Zhou and J. H. Burge, "Limits for interferometer calibration using the random ball test," in *SPIE Optical Engineering + Applications*, J. H. Burge, O. W. Fähnle, and R. Williamson, eds. (International Society for Optics and Photonics, 2009), p. 74260U.

48. P. Su, Y. Wang, J. H. Burge, K. Kaznatcheev, and M. Idir, "Non-null full field X-ray mirror metrology using SCOTS: a reflection deflectometry approach.," Opt. Express **20**, 12393–406 (2012).